Physical properties of asteroid dust bands and their sources

David Nesvorný [a,*], David Vokrouhlický [b], William F. Bottke [a], Mark Sykes [c]

[a] *Department of Space Studies, Southwest Research Institute, 1050 Walnut St., Suite 400, Boulder, CO 80302, USA*
[b] *Institute of Astronomy, Charles University, V Holešovičkách 2, 180 00 Prague 8, Czech Republic*
[c] *Planetary Science Institute, 1700 E. Ft. Lowell, Suite 106, Tucson, AZ 85719, USA*

Abstract

Disruptive collisions in the main belt can liberate fragments from parent bodies ranging in size from several micrometers to tens of kilometers in diameter. These debris bodies group at initially similar orbital locations. Most asteroid-sized fragments remain at these locations and are presently observed as asteroid families. Small debris particles are quickly removed by Poynting–Robertson drag or comminution but their populations are replenished in the source locations by collisional cascade. Observations from the Infrared Astronomical Satellite (IRAS) showed that particles from particular families have thermal radiation signatures that appear as band pairs of infrared emission at roughly constant latitudes both above and below the Solar System plane. Here we apply a new physical model capable of linking the IRAS dust bands to families with characteristic inclinations. We use our results to constrain the physical properties of IRAS dust bands and their source families. Our results indicate that two prominent IRAS bands at inclinations $\approx 2.1°$ and $\approx 9.3°$ are byproducts of recent asteroid disruption events. The former is associated with a disruption of a ≈ 30-km asteroid occurring 5.8 Myr ago; this event gave birth to the Karin family. The latter came from the breakup of a large >100-km-diameter asteroid 8.3 Myr ago that produced the Veritas family. Using an N-body code, we tracked the dynamical evolution of $\approx 10^6$ particles, 1 μm to 1 cm in diameter, from both families. We then used these results in a Monte Carlo code to determine how small particles from each population undergo collisional evolution. By computing the thermal emission of particles, we were able to compare our results with IRAS observations. Our best-fit model results suggest the Karin and Veritas family particles contribute by 5–9% in 10–60-μm wavelengths to the zodiacal cloud's brightness within 50° latitudes around the ecliptic, and by 9–15% within 10° latitudes. The high brightness of the zodiacal cloud at large latitudes suggests that it is mainly produced by particles with higher inclinations than what would be expected for asteroidal particles produced by sources in the main belt. From these results, we infer that asteroidal dust represents a smaller fraction of the zodiacal cloud than previously thought. We estimate that the total mass accreted by the Earth in Karin and Veritas particles with diameters 20–400 μm is $\approx 15,000$–20,000 tons per year (assuming 2 g cm^{-3} particles density). This is ≈ 30–50% of the terrestrial accretion rate of cosmic material measured by the Long Duration Exposure Facility. We hypothesize that up to $\approx 50\%$ of our collected interplanetary dust particles and micrometeorites may be made up of particle species from the Veritas and Karin families. The Karin family IDPs should be about as abundant as Veritas family IDPs though this ratio may change if the contribution of third, near-ecliptic source is significant. Other sources of dust and/or large impact speeds must be invoked to explain the remaining ≈ 50–70%. The disproportional contribution of Karin/Veritas particles to the zodiacal cloud (only 5–9%) and to the terrestrial accretion rate (30–50%) suggests that the effects of gravitational focusing by the Earth enhance the accretion rate of Karin/Veritas particles relative to those in the background zodiacal cloud. From this result and from the latitudinal brightness of the zodiacal cloud, we infer that the zodiacal cloud emission may be dominated by high-speed cometary particles, while the terrestrial impactor flux contains a major contribution from asteroidal sources. Collisions and Poynting–Robertson drift produce the size-frequency distribution (SFD) of Karin and Veritas particles that becomes increasingly steeper closer to the Sun. At 1 AU, the SFD is relatively shallow for small particle diameters D (differential slope exponent of particles with $D \lesssim 100$ μm is ≈ 2.2–2.5) and steep for $D \gtrsim 100$ μm. Most of the mass at 1 AU, as well as most of the cross-sectional area, is contributed by particles with $D \approx 100$–200 μm. Similar result has been found previously for the SFD of the zodiacal cloud particles at 1 AU. The fact that the SFD of Karin/Veritas particles is similar to that of the zodiacal cloud suggests that similar processes shaped these particle populations. We estimate that there are $\approx 5 \times 10^{24}$ Karin and $\approx 10^{25}$ Veritas family particles with $D > 30$ μm in the Solar System today. The IRAS observation of the dust bands may be satisfactorily modeled using 'averaged' SFDs that are constant with semimajor axis. These SFDs are best described by a broken power-law function with differential power index $\alpha \approx 2.1$–2.4 for $D \lesssim 100$ μm and by $\alpha \gtrsim 3.5$ for 100 μm $\lesssim D \leqslant 1$ cm. The total

---

* Corresponding author. Fax: +1 303 546 9687.
  E-mail address: davidn@boulder.swri.edu (D. Nesvorný).

cross-sectional surface area of Veritas particles is a factor of ≈ 2 larger than the surface area of the particles producing the inner dust bands. The total volumes in Karin and Veritas family particles with $1\ \mu m < D < 1$ cm correspond to $D = 11$ km and $D = 14$ km asteroids with equivalent masses $\approx 1.5 \times 10^{18}$ g and $\approx 3.0 \times 10^{18}$ g, respectively (assuming $2\ g\,cm^{-3}$ bulk density). If the size-frequency and radial distribution of particles in the zodiacal cloud were similar to those in the asteroid dust bands, we estimate that the zodiacal cloud represents $\sim 3 \times 10^{19}$ g of material (in particles with $1\ \mu m < D < 1$ cm) at $\pm 10°$ around the ecliptic and perhaps as much as $\sim 10^{20}$ g in total. The later number corresponds to about a 23-km-radius sphere with $2\ g\,cm^{-3}$ density.

1. Introduction

The Solar System is dusty. Small dust particles and larger micrometeoroids are produced by the sublimation and out-gassing of comets, collisions within the asteroid and Kuiper belts, and by impacts onto planetary moons. They also arrive in the Solar System from interstellar sources. Meteor showers and the zodiacal light provide the most spectacular appearances of tiny interplanetary particles to a naked-eye observer.

There are many active areas in research of interplanetary particles at this time. Some probe their mineralogical and elementary compositions, while others study their spatial, velocity and size distributions. The goals are to place Interplanetary Dust Particles (IDPs) and micrometeorites in our collections into the appropriate geologic context, determine collision and dynamical evolution of dust particles and micrometeoroids in the interplanetary space, understand the hazard posed by these projectiles to spacecraft missions, etc.

Observations of interplanetary particles have been made using several different methods: direct impacts of particles onto detectors located onboard spacecrafts such as the Long Duration Exposure Facility (LDEF; Love and Brownlee, 1993; see Grün et al., 2001, for a review of in situ spacecraft measurements); thermal infrared observations by facilities like the Infrared Astronomical Telescope (IRAS), the Cosmic Background Explorer (COBE), the Infrared Space Observatory (ISO), and the Spitzer Space Telescope (Low et al., 1984; Hauser et al., 1984; Kelsall et al., 1998; Reach et al., 1995, 2003; Sykes et al., 2005, in preparation); in scattered and reflected visible light (Ishiguro et al., 1999; Hahn et al., 2002), and by radar (e.g., Brown and Jones, 1999; Mathews et al., 2001; Janches et al., 2001; Hunt et al., 2004). About 20,000–60,000 tons of IDPs with sizes ranging from ≈ 20 to 400 μm in diameter (Love and Brownlee, 1993; Taylor et al., 1996) are annually accreted by the Earth. These and smaller interplanetary particles are collected by aircraft in the Earth's stratosphere, in the polar ice (Taylor et al., 1996), are traced using rare isotopes in deep-ocean sediments (Farley et al., 1998, 2006), and produce meteors (e.g., Brown and Campbell-Brown, 2003; see Ceplecha et al., 1998, for a review).

To explain these observations, researchers have developed physical models of interplanetary dust (Dermott et al., 1984, 1994; Grün et al., 1985; Sykes and Greenberg, 1986; Sykes, 1990; Reach et al., 1997; Durda and Dermott, 1997; Grogan et al., 1997, 2001; Kelsall et al., 1998; Moro-Martín and Malhotra, 2003; Mahoney-Hopping et al., 2003, 2004; see also the reviews by Dermott et al. (2001) and Sykes et al. (2005), and references therein). These models account for a variety of dynamical (e.g., planetary perturbations, Poynting–Robertson (P–R) and solar wind drag forces, radiation pressure, electromagnetic forces on charged particles) and physical processes (e.g., collisions, sublimation, sputtering) that determine the behavior of particles in interplanetary space and their interaction with a detector (e.g., ablation of micrometeorites in the Earth's atmosphere, ^{3}He retention, thermal radiation, light scattering).

In this paper, we will concentrate on modeling of the particles that produce the *zodiacal dust bands*. The zodiacal dust bands are extended sources of infrared (IR) emission roughly parallel to the ecliptic. They were discovered by IRAS observations in 1983 (Low et al., 1984). Originally, the major dust bands detected by IRAS were thought to be associated with three prominent asteroid families (Eos, Koronis, and Themis; Dermott et al., 1984; Sykes, 1986). More recently, using young asteroid families as tracers of recent disruptions in the main belt, Nesvorný et al. (2002, 2003) identified alternative sources of two of the brightest dust bands.

Nesvorný et al. proposed that the dust band with inclination 9.35° comes from the Veritas asteroid family at 3.17 AU, while the 2.1° band comes from the Karin family located inside the Koronis asteroid family at 2.865 AU. The Veritas and Karin families formed via collisional disruptions of >100- and ≈ 30-km-diameter parent bodies at 8.3 ± 0.5 and 5.75 ± 0.05 Myr ago, respectively (Nesvorný et al., 2002, 2003; Nesvorný and Bottke, 2004). See Durda et al. (2005) and Nesvorný et al. (2005b) for estimates of parent bodies' diameters derived from Smooth-Particle Hydrodynamic simulations of asteroid impacts.[1]

Recent disruption events are thought to be a stronger present-day source of dust particles than older, more prominent asteroid families (Sykes and Greenberg, 1986). Older families like Eos, Koronis, and Themis reached collisional equilibrium for $D < 5$ km bodies (Morbidelli et al., 2003; Bottke et al., 2005). This means their present ability to produce large quantities of dust particles is generally limited. Conversely, recently formed families should still contain large quantities of $\gtrsim 1$-cm-diameter particles that can feed populations of <1-cm-diameter particles through the collisional cascade.

---

[1] The Veritas family's parent body may have been ≈ 160 km in diameter (Durda et al., 2005), or smaller if (490) Veritas is an interloper in its own family (see discussion in Nesvorný et al., 2003).

A more specific problem we have in linking the IRAS dust bands to large families is that the orbital inclination of the dust bands typically does not produce a precise match with the proposed source family. For example, there is a $\approx 1°$ discrepancy between the outer dust band (inclination $i \approx 9.35°$; Sykes, 1990; Reach et al., 1997; Grogan et al., 1997, 2001) and the mean inclination of Eos family members ($i \approx 10.3°$) (e.g., see Dermott et al., 2001, in particular their Fig. 16 and the related discussion). A better fit for this band comes from the Veritas family whose mean inclination value is $\approx 9.3°$. The large size of the Veritas family's parent body, when compared to the relatively small size of the Karin family's parent body, allows us to naturally explain why the cross-sectional area of dust contributing to the outer dust band is larger than the area of dust coming from inner, near-ecliptic band associated with the Karin family (Dermott et al., 2002; Nesvorný et al., 2003).

As particles evolve inward toward the Sun, they absorb sunlight and reemit the energy over thermal infrared wavelengths. To produce the observed, smooth longitudinal profile of the IRAS dust bands, we need the radiating particles to have nodal and perihelion longitudes distributed uniformly between 0° and 360° (Sykes, 1990). Conveniently, the Karin family and the Veritas family are several Myr old, old enough that the nodal and perihelion longitudes of their immediate precursors have been randomized by planetary perturbations (Sykes and Greenberg, 1986).

In this paper, we have constructed a new physical model for the zodiacal dust bands where the Veritas family and the Karin family are assumed to be the source locations of the particles producing the dust bands. This model is complimentary to the previous work on the subject. Following closely the method developed by the Florida group (Dermott et al., 1984, 1988, 1994, 2001, 2002; Grogan et al., 1997, 2001; Mahoney-Hopping et al., 2003, 2004), we use numerical integration to propagate particles from our source region to the sinks. Moreover, we also account for the collisional disruption of the particles. We believe the physical model described here has several important advantages over empirical fits to data (e.g., Sykes, 1990; Kelsall et al., 1998; Reach et al., 1997):

(1) The cloud of dust particles evolving into the inner solar system by P–R drag may gradually become spread in ecliptic latitude by planetary perturbations that resonate with orbital modes (e.g., secular resonances at ≈ 2 AU). By using direct numerical integration, we can track particles through the resonances and determine the fraction of dust (produced by recent asteroid disruptions) that spreads to large inclinations and thereby contributes to the broad-background, zodiacal cloud IR emission.

(2) By using a model based on orbital integrations, we can realistically characterize the complex spatial distribution of particles in the IRAS dust bands and include the effects of the warped plane of symmetry, the offset produced by forced eccentricity, etc. We can also determine the dependence of these effects on heliocentric distance. See Dermott et al. (2001) for a discussion and illustrations of these important effects.

(3) In the low-opacity circumsolar environment like that of the zodiacal cloud, the temperature of a small particle in interplanetary space is determined by its size, optical properties, and distance from the Sun. As the particle slowly evolves inward by the effects of P–R drag, its temperature increases, which shifts the peak of its thermal emission to shorter wavelengths. The IRAS detectors, with effective wavelengths 12-, 25-, 60-, and 100-μm, can be used as windows into the spatial and size-frequency distributions of orbitally evolving particles at various heliocentric distances.

(4) The combined effect of disruptive collisions, P–R drag and planetary perturbations make it likely that the size-frequency distribution (SFD) of the evolving dust complex changes with heliocentric distance (R). In our model, we allow for SFDs that vary with R (Section 4.2).

Our model, which is described in Section 2, includes all features used in Grogan et al. (2001). In addition, (i) our model also accounts for thermal emission of diameter $D > 100$ μm particles; (ii) it includes dynamical effects on particles with $a < 2$ AU; (iii) it includes improved parameterization of the orbital distribution of asteroid dust obtained by integrating the orbits of $\approx 10^6$ particles; and (iv) it accounts for the variation of proper elements with a. We have also explored how the optical properties of different materials, as well as how the initial orbital dispersions of particles, change our results. Perhaps the most important aspect of our model is that it accounts for the collisional disruption of particles as well as the generation of new debris particles on the same orbits as their precursors (Section 4.2).

In the present paper, we constrain our model by using observations of zodiacal IR emission obtained by the IRAS (Neugebauer et al., 1984). We compare our results with the IRAS medium-resolution dataset in Section 3. Our best-fit models are determined in Section 4 and are discussed in Section 5.

2. Model

Our model for the asteroid dust bands has 4 parts: (i) we define the initial orbital and size-frequency distributions of particles at the source; (ii) we track their orbital and collisional evolution to the sink; (iii) we characterize the thermal IR emission from these synthetic particle distributions; and (iv) we model the detection of their thermal IR emission by a space-borne infrared telescope. These model components are described below.

2.1. Orbits and sizes of particles at sources

To accurately represent the spatial distribution of particles at the epoch of IRAS observations (Epoch 1983.5), we must follow their orbital and collisional evolution from when they were released from their immediate precursor to 1983.5. Since different particles were released at different times (via the stochastic nature of collisional disruption events), we performed orbital integrations of particles that start at many past epochs and tracked their evolution forward in time to 1983.5. As a

simplifying assumption, all particles in our integrations were released at the source locations of the dust bands taken here as the orbital locations of the Karin cluster and the Veritas family. We will account for the collisional removal of drifting particles and the injection of second-generation fragments into the intermediate orbits in Section 4.2.

To select the initial orbits of particles at the location of the Karin cluster and the Veritas family, we assumed that their initial orbital distributions resemble those of large asteroid members observed in these families. Because small particles may be actually more spread in orbital element space than the large asteroid members (reflecting size-dependance of ejection speeds; Nakamura, 1992), we used scaling factors that can stretch the initial distribution of orbits to a required range of values. These factors, described below, were treated as free parameters in our model.

In the first step, we separated the proper (also called free) and forced orbital elements of observed asteroid members by the particle-on-a-circle method (Hirayama, 1918). See Murray and Dermott (1999) (their Section 7.4), for a definition of these parameters and Dermott et al. (2001) for a description of the particle-on-a-circle method. It is important to deal with the proper and forced elements separately. The forced elements are a function of a and are controlled by secular planetary perturbations at that semimajor axis. The proper/free elements define the orbit of an asteroid in absence of planetary perturbations. While forced elements vary with time t reflecting changing configuration of planets, the proper elements are constant.[2] Hence, to set up the initial orbits of particles at t, we must vectorially sum the proper and forced orbits at t. We clarify this method below.

As for the Karin cluster, we used its 84 asteroid members identified by the Hierarchical Clustering Method with the 10 m s^{-1} cutoff (Nesvorný and Bottke, 2004). Osculating orbital elements of these asteroids were extracted from the AS-TORB catalog (Bowell et al., 1994) at MJD 2452700.5 epoch and were referred to the invariant plane of planets. We fitted circles to distributions of these orbits in the $[e \cos \varpi, e \sin \varpi]$ and $[i \cos \Omega, i \sin \Omega]$ planes, where e is the eccentricity, and i, ϖ, and Ω are the inclination, perihelion and nodal longitudes referred to the invariant frame.

The distances of centers of these circles from the origin are the forced eccentricity (e_f) and the forced inclination (i_f), respectively. We found $e_f = 0.0370$ and $i_f = 0.506°$. The angular position of centers of the circles are the forced perihelion longitude (ϖ_f) and the forced nodal longitude (Ω_f). We found $\varpi_f = 7.0°$ and $\Omega_f = 313°$. The circles' radii are the mean proper eccentricity (mean e_p) and the mean proper inclination (mean i_p) of Karin cluster members. By determining the circles' radii we determined the mean values of proper elements that were similar to the mean values calculated previously from the analytic proper elements ($e_p = 0.0446$ and $i_p = 2.11°$;

Table 1
Parameters defining our orbit selection at sources

	Karin	Veritas
$\langle a \rangle$	2.866	3.169
Δa	0.010	0.015
$\langle e_p \rangle$	0.0446	0.0636
Δe_p	0.007	0.04
$\langle i_p \rangle$	2.11	9.26
Δi_p	0.09	0.5
e_f	0.037	0.026
i_f	0.51	0.42
ϖ_f	7.0	11.1
Ω_f	313.0	315.0

The forced orbital elements at the 1983.5 epoch were determined by the 'particle-on-a-circle' method described in the main text. The angles are given with respect to the invariant plane of planets (Appendix A). The forced longitudes given in this frame are rotated by $\approx 213°$ in the counterclockwise direction from longitudes given in the ecliptic frame. Symbols $\langle \cdot \rangle$ denote mean values. Angles are given in degrees and a is in AU. Δ denotes the full spread in elements.

Nesvorný et al., 2002). The spread of proper elements of Karin cluster members around the mean value is $\Delta e_p = 0.007$ and $\Delta i_p = 0.09°$. Their proper perihelion and nodal longitudes (ϖ_p and Ω_p) are distributed randomly between 0° and 360° at the current epoch, as expected.

Using similar means, we separated the proper and forced elements for Veritas family members. We used 259 members of this family that were identified using a 40 m s^{-1} cutoff (Nesvorný et al., 2003). Table 1 lists the determined values.

In the second step, we calculated the forced elements for $a \approx 2.865$ AU and $a \approx 3.17$ AU at past epochs. Fourier series represent a convenient parameterization of forced elements for any time t:

$$e_f \exp \iota \varpi_f = \sum_{j=1}^{N} A_j \exp \iota (g_j t + \phi_j),$$

$$i_f \exp \iota \Omega_f = \sum_{j=1}^{N} B_j \exp \iota (s_j t + \theta_j), \qquad (1)$$

where A_j, B_j, g_j, s_j, ϕ_j, θ_j are real parameters, and $\iota = \sqrt{-1}$. We determined these parameters numerically using a 10-Myr-long integration of representative orbits and the Fourier-transform-based method described in Šidlichovský and Nesvorný (1997). For $t = 0$ the forced elements calculated here closely match the values determined by the particle-on-a-circle method in step one (values listed in Table 1). We also verified that Eq. (1) with $N = 10$ provides representations of the forced elements for any $-10 \lesssim t \lesssim 10$ Myr to better than 5% precision in e_f and i_f and to $\lesssim 1°$ in ϖ_f and Ω_f.

We used 100 past epochs, $t_k = -k \times T/100$, $k = 1, \ldots, 100$, where T was taken to be either the P–R drag lifetime of a particle of radius s or the age of its source family (i.e., 5.8 Myr for Karin; 8.3 Myr for Veritas particles) whichever turned out to be smaller. For each epoch t_k, we produced 100 orbits that had forced elements given by Eq. (1) with $t = t_k$. We assumed a uniformly random mean anomaly, ϖ_p and Ω_p between 0° and 360°, uniformly random a between 2.861 and 2.871 AU (corre-

---

[2] The proper elements of asteroids are constants of motion of a conservative dynamical system that approximates asteroid dynamics (Milani and Knežević, 1994). In Section 2.4, we will define generalized proper elements for small particles that evolve by P–R drag. These generalized proper elements will depend on the orbital history and particle size.

sponding to the semimajor axis spread of observed large Karin cluster members; $\Delta a = 0.01$ AU), and a uniformly random e_p and i_p in intervals $\Delta e_p = 0.007$ and $\Delta i_p = 0.09°$, respectively, around the mean values of these elements listed in Table 1. Using the same method, we also produced 100 orbits for every t_k at the location of the Veritas family.

We initially limited our selection of orbits by assuming that small particles produced at the source locations at $t = t_k$ had the same orbital spread as the observed asteroid members in the source families at the current epoch. As discussed above, this may or may not be a correct assumption. To allow for the possibility that small particles are spread in proper orbital elements more than large members, we also used orbital dispersions given by $f_a \Delta a$, $f_e \Delta e_f$, and $f_i \Delta i_f$, where Δa, Δe_f, and Δi_f are the orbital spreads of large asteroid members and f_a, f_e, and f_i are multiplication factors $\geqslant 1$. In particular, we assumed that $f_a = f_e = f_i = f$ and used $1 \leqslant f \leqslant 40$. For Karin particles, $f = 1$ and $f = 40$ correspond to ≈ 15 and ≈ 600 m s^{-1} ejection speeds, respectively.

We used particles with radius $s = 0.5, 1.5, 5, 15, 50, 150, 500, 1500,$ and 5000 μm. In a single run, we started 100 particles of the same size per epoch and used 100 different epochs. In total, orbits of 90,000 particles of different sizes were integrated per job. We performed 10 jobs with different values of f for Karin and Veritas particles, along with many additional test runs. In total, we numerically integrated more than 10^6 test particles.

2.2. Orbit evolution

The orbits of our test particles were tracked using the Wisdom–Holman map (Wisdom and Holman, 1991) modified to include effects of radiation forces (Burns et al., 1979). The acceleration $\vec{F}$ on a particle due to these forces is

$$\vec{F} = \beta G \frac{m_\odot}{R^2} \left[\left(1 - \frac{\dot{R}}{c} \right) \frac{\vec{R}}{R} - \frac{\vec{V}}{c} \right], \tag{2}$$

where $\vec{R}$ is the orbital radius vector of the particle, $\vec{V}$ is its velocity, G is the gravitational constant, $m_\odot$ is the mass of the Sun, c is the speed of light, and $\dot{R} = dR/dt$. The acceleration (2) consists of the radiation pressure and the velocity-dependent Poynting–Robertson (P–R) term. Parameter β is related to the radiation pressure coefficient (Q_{pr}) by

$$\beta = 5.7 \times 10^{-5} \frac{Q_{pr}}{\rho s}, \tag{3}$$

where radius s and density ρ of the particle are in cgs units. Pressure coefficient Q_{pr} can be determined using Mie theory (Burns et al., 1979). We used $Q_{pr} = 1$ which corresponds to the geometrical optics limit where s is much larger than the incident-light wavelength. We assumed that the solar wind drag force has the same functional form as the P–R term and contributes by $\approx 30\%$ to the drag intensity (Gustafson, 1994).

We used bulk density $\rho = 2.0$ g cm^{-3} for all particles. For comparison, Love et al. (1994) reported $\rho \approx 2.0$ g cm^{-3} for stratospheric-collected IDPs, while McDonnell and Gardner (1998) found mean $\langle \rho \rangle = 2.0$–$2.4$ g cm^{-3} from the analysis of

data collected by the LDEF and Eureca satellites. If measured bulk densities of asteroids tell us something about the particle densities that come from them, Karin particles may have a somewhat larger density than 2.0 g cm^{-3} because they derive from an S-type asteroid (Jedicke et al., 2004; Nesvorný et al., 2005a). Conversely, the C-type Veritas family (Di Martino et al., 1997; Bus and Binzel, 2002; Cellino et al., 2002) may produce particles with lower ρ. We do not account for these effects here.

We used the `swift_rmvs3` code (Levison and Duncan, 1994) which is an efficient implementation of the Wisdom–Holman map and which, in addition, can deal with close encounters between particles and planets. The radiation pressure and drag forces were inserted into the Keplerian and kick part of the integrator, respectively.[3]

The code tracks the orbital evolution of a particle that revolves around the Sun and is subject to the gravitational perturbations of seven planets (Venus to Neptune) until the particle impacts a planet, is ejected from the Solar System, evolves to within 0.3 AU from the Sun, or to $t = 0$ (corresponding to 1983.5). We removed particles that evolved to $R < 0.3$ AU because our integration scheme ignores orbital perturbations from Mercury and thus is inappropriate in the Mercury zone. Moreover, the orbital period for $R \lesssim 0.3$ AU is not properly resolved by our 10-day integration timestep. Fortunately, we do not need to account for the thermal emission of particles with $R < 0.3$ AU because the telescope was not allowed to point close to the Sun. IRAS measured the thermal IR flux at solar elongations between $\approx 60°$ and $\approx 120°$ in both the leading and trailing directions, thus IRAS scanned no closer than 0.87 AU to the Sun. Note that most particles reaching $R = 0.3$ AU will continue their orbital decay into the Sun.

To illustrate the variety of orbital evolutions produced by our simulations, we plotted the orbital elements of $s = 5, 50,$ and 500 μm Karin and Veritas particles at 1983.5 in Figs. 1 and 2. As particles spiral toward the Sun by the effects of P–R drag, their inclinations remain roughly constant for $a \gtrsim 2$ AU because the effects of resonant planetary perturbations in this region on i are small. The eccentricities are driven to smaller values by P–R drag, while the particles jump over the locations of mean motion resonances with Jupiter such as the 3:1 ($a = 2.5$ AU) and 5:2 ($a = 2.82$ AU) (see bottom panels in Figs. 1 and 2).

Small particles from Veritas are subject to strong effects of the radiation pressure that instantly, upon their release from the parent body, reduce the pull they feel towards the Sun. The semimajor axis of their new osculating orbits about effective central mass $m_\odot(1 - \beta)$ is larger than the semimajor axis of the Veritas family by about a factor of $(1 - \beta)/(1 - 2\beta)$ for low e. This change in a places small Veritas particles ($s \lesssim 10$ μm) in or just outside the 2:1 mean motion resonance with Jupiter located at $a \approx 3.27$ AU. Those that fall into the 2:1 will drift toward smaller values of e. Those that fall beyond the outer boundary of the 2:1 ($a \gtrsim 3.35$ AU) will transit over the resonance during their subsequent evolution (see top panels in Fig. 2). Because

---

[3] The change to the Keplerian part was trivially done by substituting $m_\odot$ by $m_\odot(1 - \beta)$.
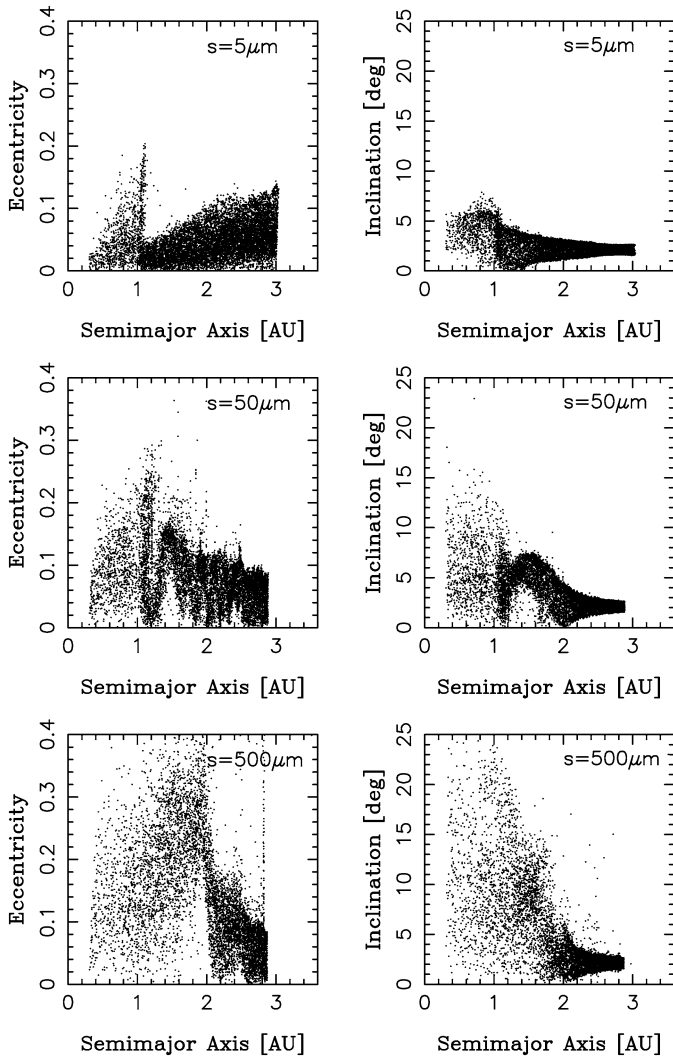
Fig. 1. From top to bottom, the orbital elements of radius $s = 5$, 50, and 500 μm Karin particles at 1983.5. In total, 10,000 particles of each size were released at the location of the Karin cluster ($a \approx 2.866$ AU) at various past epochs and were tracked into the inner Solar System by following their orbital decay due to P–R and solar wind drags. Here we show the result with $f = 1$.

Fig. 2. From top to bottom, the orbital elements of radius $s = 5$, 50, and 500 μm Veritas particles at 1983.5. In total, 10,000 particles of each size were released at the location of the Veritas family ($a \approx 3.17$ AU) at various past epochs and were tracked into the inner Solar System by following their orbital decay due to P–R and solar wind drags. Here we show the result with $f = 1$.

this inward migration cannot result in a simple capture,[4] particles will jump over the resonant location and receive a net positive kick in e. For initially low-e orbits that jump over the 2:1, e increases by ≈ 0.2.

Following their orbital decay, particles start to interact with strong secular resonances at $a \approx 2$ AU (ν_5, ν_6, and ν_{16}; Williams, 1979; Morbidelli and Henrard, 1991). Rapidly drifting small particles only reside inside the resonance for a short time and thus only experience modest perturbations. Slow drifting large particles, on the other hand, have time to interact and thus suffer significant orbital changes. An example of these changes can be seen in Figs. 1 and 2, where $s = 500$ μm par-
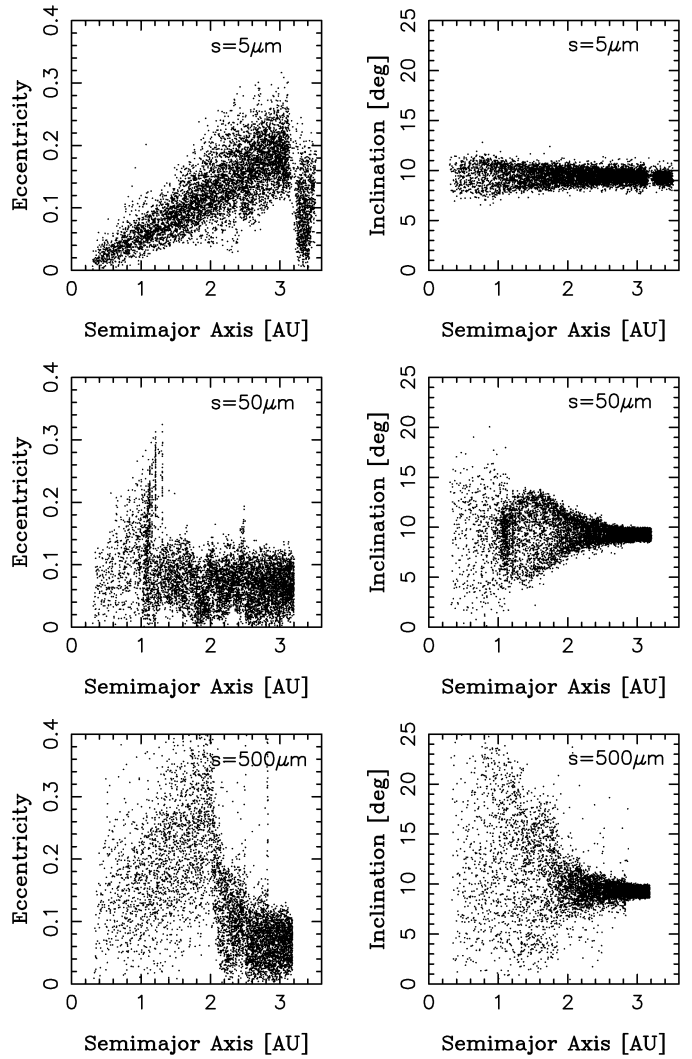
ticles cross $a = 2$ AU. These large particles have their orbital eccentricities excited to ~ 0.3 while their orbital inclinations become spread over a large range of values. Additional effects on i are produced by the ν_{13} and ν_{14} secular resonances located at $a < 2$ AU (Michel and Froeschlé, 1997). The thermal radiation of particles in these extended inclination structures will mainly contribute to the low-spatial-frequency broad-background component of the zodiacal light.

Further orbital changes are produced by planetary perturbations at $a \lesssim 1.5$ AU. Drifting particles can be trapped in exterior resonances with planets (Jackson and Zook, 1992; Weidenschilling and Jackson, 1993; Šidlichovský and Nesvorný, 1994). A belt of dust particles trapped by resonances near Earth was detected by IRAS as the apex/anti-apex asymmetry of the IR brightness (Dermott et al., 1994), and was confirmed by COBE (Reach et al., 1995).

The effect of resonant trapping on eccentricities just outside 1 AU is important for $5 \lesssim s \lesssim 100$ μm Karin particles and

---

[4] Occasional captures in the 2:1 may occur when particles are trapped in one of the secular resonances residing inside the 2:1 (such as the ν_5 or ν_6; Morbidelli and Moons, 1993). These particles then follow the loci of the secular resonance from low to large e, and are eventually released from the 2:1 with $e \approx 0.5$ (Marzari and Weidenschilling, 2002).

$30 \lesssim s \lesssim 100$ μm Veritas particles (Figs. 1 and 2). Small Veritas particles have their eccentricities excited early in the evolution by the effects of the 2:1 resonance, while large particles in general are excited by the secular resonances at 2 AU. These particles are rarely trapped in resonances with the terrestrial planets because interactions with main belt resonances frequently give them large e values (Weidenschilling and Jackson, 1993; Šidlichovský and Nesvorný, 1994).

Additional effects on particle orbits are produced by their encounters with the terrestrial planets that spread their e's and i's to large values. These effects are especially pronounced for particles reaching $R \lesssim 1$ AU, where scattering events by Earth and Venus become increasingly important. These perturbations can erase the original orbital distribution of the particles and make it difficult to trace particle populations from $R \lesssim 1$ AU back to their sources in the main belt. The effects of planetary encounters are less important for high-i and/or small fast-drifting particles.

Overall, the density distribution of particles in a is $\propto a$, notwithstanding a few bumps and dips at the orbital location of planets and planetary resonances. This functional form is expected from the rate of orbital decay of particles by P–R drag ($\propto 1/a$). The faster decay at smaller a produces a constant particle surface density in the mid-plane. Inter-particle collisions become increasingly important for $a \to 0$ because inter-particle speeds increase as $1/\sqrt{a}$ during the orbital decay (Grün et al., 1985). A fraction of particles produced by disruptive collisions are sub-micrometer in size and are ejected from the Solar System by radiation pressure. Evidence for these particle populations (β meteoroids) at $a < 1$ AU was found by the Helios probe (Leinert and Grün, 1990). Pioneer 8 and 9 observed the flux of these small particles from the solar direction at larger a (Berg and Grün, 1973).

The average duration (T_{decay}) of the orbital evolutions in Figs. 1 and 2 is a close match to the time scale at which particles on near-circular, unperturbed orbits are expected to decay due to effects of P–R drag and the solar wind. The orbital decay from a low-e source at a to 1 AU is $T_{\text{decay}} \approx 500$ yr $\times \rho s (a^2 - 1)$, where s is the particle's radius in μm and ρ is its density in g cm^{-3} (Wyatt and Whipple, 1950). For example, a particle from the Karin family with $\rho = 2.0$ g cm^{-3} and $s = 5$ μm decays from 2.865 to 1 AU in $\approx 36{,}000$ yr, while the same evolution takes ≈ 3.6 Myr for one with $s = 500$ μm. The time scales needed for particles from the Veritas family to reach 1 AU are longer because they start at a larger initial a. Captures in exterior resonances with the terrestrial planets can stretch these time scales by $\sim 10{,}000$–$100{,}000$ yr (Šidlichovský and Nesvorný, 1994). Using these results, we estimate that the surviving particles from the Karin and Veritas breakup events with $s \gtrsim 5$ mm have remained within $\lesssim 0.4$ AU of their source locations.

2.3. Thermal emission of particles

Particles were assumed to be isothermal, rapidly rotating spheres. The absorption was assumed to occur into an effective cross-section πs^2, and emission out of $4\pi s^2$. The IR flux density (per wavelength interval dλ) per unit surface area at distance r from a thermally radiating particle with radius s is

$$F(\lambda) = \epsilon(\lambda, s) B(\lambda, T) \frac{s^2}{r^2}, \qquad (4)$$

where ϵ is the emissivity efficiency and $B(\lambda, T)$ is the energy flux at $(\lambda, \lambda + d\lambda)$ per surface area from a black body at temperature T:

$$B(\lambda, T) = \frac{2\pi hc^2}{\lambda^5}[e^{hc/\lambda kT} - 1]^{-1}. \qquad (5)$$

In this equation, $h = 6.6262 \times 10^{-34}$ J s is the Planck constant, $c = 2.99792458 \times 10^8$ m s^{-1} is the speed of light, and $k = 1.3807 \times 10^{-23}$ J K^{-1} is the Boltzmann constant.

We used the Mie theory for spherical particles to calculate ϵ (e.g., Bohren and Huffman, 1983). To determine ϵ, the real (n) and imaginary (k) parts of the refractive index of particles had to be specified. These quantities depend in complicated ways on wavelength. To understand the dependence of our results on the optical properties of particles, we used several different plausible materials. The optical constants of these materials are shown in Fig. 3.

Olivines, pyroxenes and their mixtures are known to provide good spectral matches to the laboratory spectra of stratospheric IDPs (Sandford and Walker, 1985). Li and Greenberg (1997) have shown that the amorphous olivine described by Dorschner et al. (1995) has optical constants in the mid- and far-infrared spectrum that are representative of astronomical silicate (Draine and Lee, 1984). Motivated by these results, we used amorphous magnesium silicates with olivine stoichiometry Mg$_2$SiO$_4$ (denoted 'olivine' in Fig. 3) and with pyroxene stoichiometry MgSiO$_3$ (denoted 'pyroxene'). These materials are reasonable analogues within the context of this work for the composition of asteroid dust.

The laboratory spectra of these iron-free silicates have been measured by Jäger et al. (2003). From the comparison between laboratory spectra of olivine- and pyroxene-type silicates and astronomical spectra, it has been suggested that only completely iron-free magnesium silicates like forsterite and enstatite can account for the observed positions of silicate bands in circumstellar and cometary sources (Jäger et al., 1998; Bowey et al., 2002; Molster et al., 2002). Moreover, Reach et al. (2003) have shown that the amorphous forsterite/olivine is required to explain features in the mid-infrared spectrum of the zodiacal light. These results motivated the use of iron-free silicates in the present work.

Dorschner et al. (1995) determined the optical constants for olivine- and pyroxene-type materials with variable content of Fe. These variations are modest in the wavelength range of the IRAS filters (7–140 μm). Moreover, iron-rich pyroxene-type silicates have values of n and k that are often intermediate between those of amorphous Mg$_2$SiO$_4$ and MgSiO$_3$. For this reason, we used iron-free silicates in this work to represent the possible range of values for optical constants of silicates. Aluminium and calcium content in amorphous silicates produce only modest effect on optical constants (Mutschke et al., 1998).
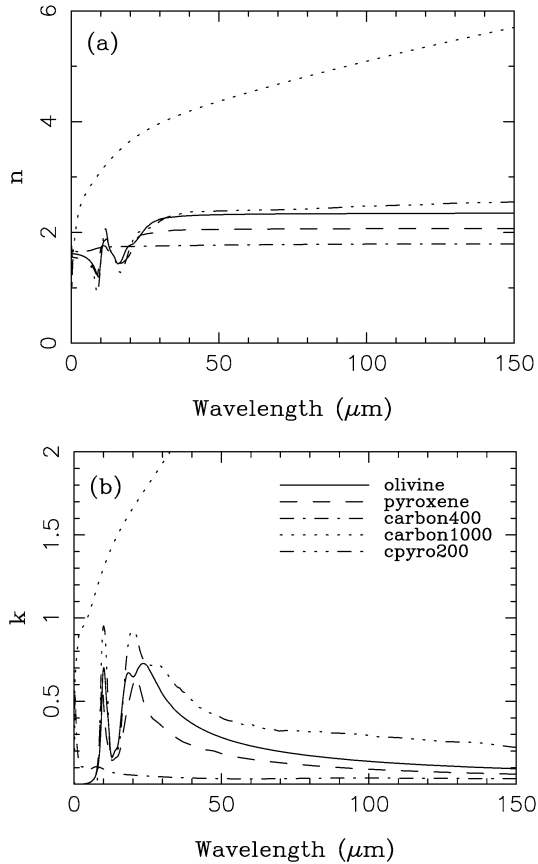
Fig. 3. Optical constants n and k for different materials described in the text. The imaginary part of refractive index for 'carbon1000' is a smoothly increasing function for $\lambda > 30$ μm that reaches $k = 5$ at $\lambda = 150$ μm. Data from Dorschner et al. (1995), Henning and Mutschke (1997), and Jäger et al. (1998, 2003).

The third material we used was the amorphous pyroxene of approximately cosmic composition with the following elementary abundances of the metal ions: Mg 28.1%, Fe 17.3%, Al 1.1%, Ca 2.2%, and Si 51.3%. Henning and Mutschke (1997) have determined the optical constants for this material for various low temperatures. Fig. 3 shows the optical constants for 200 K (denoted 'cpyro200') that is roughly the characteristic temperature of dust grains at 3 AU. We used these low-temperature data as a possible probe to temperature-dependent signature of n and k in the asteroid dust bands. The difference of n and k between amorphous $Mg_2SiO_4/MgSiO_3$ and the cosmic pyroxene at 200 K is large enough to be potentially identified in our fits to the IRAS data. We did not use Henning's and Mutschke's (1997) results for cosmic pyroxene at 300 K because these room-temperature measurements show values of n and k that are intermediate between the two iron-free magnesium silicates we use.

Given the goals of this work, we found it unnecessary to model the thermal emission from crystalline silicates. In contrast to amorphous silicates, crystalline silicates show a lot of diagnostic bands due to metal–oxygen vibrations in the mid-infrared range. Unfortunately, these bands are too sharp and too subtle to be detected in the wide-wavelength IRAS filters. Smoothed by IRAS filters, the thermal spectrum

of crystalline silicates is similar to that of amorphous silicates.[5]

For our model, we used carbonaceous dust analogues. Jäger et al. (1998) obtained these materials by carbonization of cellulose at temperatures between 400 and 1000 K. The increasing pyrolysis temperatures indicate increasing carbonization (graphitization) of the material. These structural changes have a large influence on the far-infrared thermal emission of carbon materials. We use Jäger et al.'s optical constants for pyrolyzed cellulose at 400 and 1000 K that represent two sides of the range of n and k in far-infrared (denoted 'carbon400' and 'carbon1000' in Fig. 3). The optical constants of 'carbon1000' are similar to those that have been measured for other carbonaceous dust analogues (e.g., Edoh, 1983; Zubko et al., 1996). The optical constants of 'carbon400' are similar to those derived by Li and Greenberg (1997) for organic refractory material. Both carbonaceous and silicate features are present in the cometary spectra (Hanner, 1999).[6]

Fig. 4 shows ϵ as a function of wavelength for spherical particles of radius $s = 5$, 50, and 500 μm and five different materials. For $s = 5$ μm particles, ϵ drops with λ because these small particles do not efficiently radiate at far-infrared wavelengths. Small silicate particles show increased emission efficiencies at 10- and ≈ 25-μm wavelengths. Small carbon grains with high carbonization degrees ('carbon1000' in Fig. 4) show largest emission efficiencies at $\gtrsim 50$ μm from all materials used here. In contrast, small carbon grains with low carbonization levels ('carbon400') have the lowest emission efficiencies at long wavelengths from all materials used here.

We used two methods to determine the temperature of a particle at distance R from the Sun. In the first method, we balanced the absorbed and re-radiated energy fluxes:

$$(1 - A)\frac{\mathcal{F}_0}{4R^2} = \int_\lambda \epsilon(\lambda, s) B(\lambda, T)\, d\lambda, \qquad (6)$$

where A is the albedo and $\mathcal{F}_0 = 1370$ W m^{-2} is the solar constant. The left-hand side of Eq. (6) approximates the absorbed energy in the optical limit where the radiating grain is much larger than the incident wavelength. According to Sekanina et al. (2001), this approximation is valid for grains that are several micrometers in size or larger. Using Mie theory for spherical particles to calculate $\epsilon(\lambda, s)$ and Eq. (5), we solved Eq. (6) for $T = T(R)$ by iterations. We assumed $A = 0.1$. Our choice of albedo was motivated by asteroidal values (Tedesco et al., 2002) and by the fact that chondritic IDPs are dark objects with <15% reflectivity (Bradley et al., 1996). The temperature of a

[5] Using other means, crystalline silicates have been detected in the cometary dust (Hanner et al., 1994; Hanner, 1996; Crovisier et al., 1997), β-Pictoris-like dust disks around main sequence stars (Knacke et al., 1993; Fajardo-Acosta and Knacke, 1995) and in other circumstellar dust environments (e.g., Waelkens et al., 1996). Crystalline silicates are also present in IDPs (MacKinnon and Rietmeijer, 1987; Bradley et al., 1992) and meteorites. Moreover, Reach et al. (2003) have found that the 9–11-μm silicate feature observed in the zodiacal light requires the presence of crystalline olivine phases in the dust grains.
[6] Optical constants for all materials used in this work were obtained from: http://www.astro.uni-jena.de/Laboratory/Database/odata.html.
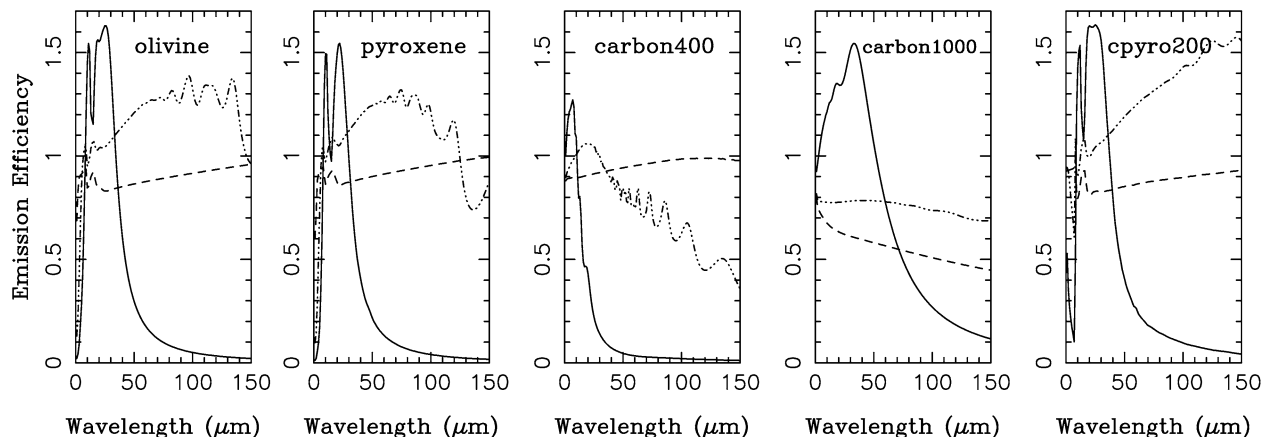
Fig. 4. Emission efficiency ϵ for spherical Mie particles composed of materials described in the text. The solid, dotted, and dashed lines show ϵ for radius $s = 5, 50$, and 500 μm particles, respectively.

small grain at 1 AU is about 3% higher/lower if its A is varied between 0 and 0.2.

Silicate particles with $s = 5$–500 μm at distance R have equilibrium temperatures within 10 K of the equilibrium temperature of a gray body at the same distance with $A = 0.1$ and $T(R) = 275/\sqrt{R}$ K. Carbonaceous grains show larger variation. For example, a 5-μm-radius grain composed of 'carbon1000' is about 30 K hotter than a 50-μm-radius particle of the same composition. These temperature variations may have measurable effects on the fluxes detected in the IRAS filters.

In the second method, we used the temperature variations with R that were proposed by different authors from spectral observations of the zodiacal cloud (e.g., Dumont and Levasseur-Regourd, 1988; Renard et al., 1995; Leinert et al., 2002; Reach et al., 2003). For example, Leinert et al. (2002) proposed that $T(R) = 280/R^{0.36}$ K near $R = 1$ AU from ISOPHOT spectra. We used $T(R) = T_{1\,\mathrm{AU}}/R^{\delta}$ K, where $T_{1\,\mathrm{AU}}$ is the temperature at 1 AU and δ is a power index. We varied $T_{1\,\mathrm{AU}}$ and δ to see how our results depend on these parameters. These tests are described in Section 4. Values $\delta < 0.5$ would be expected, for example, for micrometer-sized and/or fluffy particles with small packing factors (e.g., Gustafson et al., 2001).

IRAS measured IR fluxes in four filters with effective wavelengths of 12, 25, 60, and 100 μm. Fig. 5 shows the overall response of IRAS system defined as the product of the optical transmittance and relative detector response, and normalized to its peak value. We denoted these profiles by $\mathcal{I}_j(\lambda)$, where j denotes the filters in sequence from 1 to 4 (i.e., $\mathcal{I}_1(\lambda)$ is the overall response function of the 12-μm IRAS filter). To determine the model flux detected in each IRAS filter (F_j), we multiplied Eq. (4) by $\mathcal{I}_j(\lambda)$ and integrated over wavelengths:

$$F_j = \frac{s^2}{r^2} \int_{\lambda} \mathcal{I}_j(\lambda)\epsilon(\lambda, s)B(\lambda, T)\,\mathrm{d}\lambda, \qquad (7)$$

where the radiating particle of radius s is at a distance r from the telescope, and $T = T(R)$ is calculated from Eq. (6).

The IRAS filters can be used as windows into the dust distribution at different distances from the Sun. From Wien's dis-
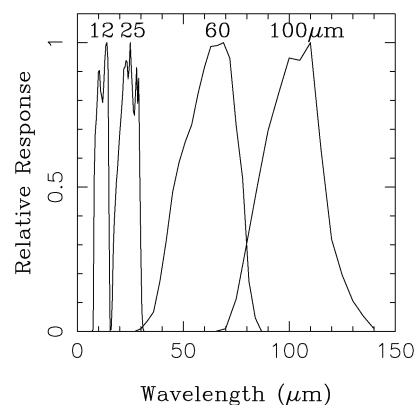

Fig. 5. The relative spectral response of the IRAS system. Data taken from http://dorothy.as.arizona.edu/DSN/IRAS/FPA/ (see Neugebauer et al., 1984). The profiles have been normalized so that they are equal to 1 at the wavelength of peak sensitivity.

placement law,

$$\lambda_{\max} = \frac{hc}{4.965kT} = \frac{2898}{T}\ \mathrm{K\,\mu m}, \qquad (8)$$

we found that a gray body radiates maximum energy fluxes at 12-, 25-, and 60-μm wavelengths if heated to 241, 116, and 48 K, respectively. Hence, measurements in the 12-μm IRAS band are sensitive to distributions of particles in the inner Solar System, while the 25- and 60-μm band measurements preferentially detect thermal emission from larger R. IRAS measurements in the 100-μm band are less useful for probing the thermal radiation of dust particles in the Solar System.

2.4. SIRT—Synthetic InfraRed Telescope

To compare our numerical results with data from spaceborne infrared telescopes, we developed a code that models thermal emission from distributions of orbitally evolving particles and produces IR fluxes that a space-borne infrared telescope would detect depending on its location, pointing direction, and the epoch of observation. A version of this code simulates IRAS observations. This code differs in several aspects from other comparable codes described in the literature (e.g.,

SIMUL; Dermott et al., 1988). Our code, which we call SIRT (Synthetic InfraRed Telescope), uses the following algorithm.

We assumed that the telescope is located at (x_t, y_t, z_t) in the Sun-centered reference frame and that its viewing direction in the same frame is defined by unit vector with components (x_v, y_v, z_v). Transformation of these vectors between the ecliptic and invariant frames is straightforward (Appendix A). The pointing vector can be also conveniently defined by longitude l and latitude b of the pointing direction, where $x_v = \cos b \cos l$, $y_v = \cos b \sin l$, and $z_v = \sin b$.

In Section 2.2, we produced a large database of test orbits by tracking the orbital evolution of $\approx 10^6$ particles from sources to sinks. Here we use this database to produce a spatial distribution of dust particles that is sufficiently smooth to allow us to model important, small-scale features in the IRAS scans. We assumed that the a, e, i of each individual orbit represents a large number of particles that have orbits with uniformly random nodal, perihelion, and mean orbital longitudes. In absence of planetary perturbations, the spatial density of particles distributed in this way is (Kessler, 1981; Sykes, 1990):

$$S(R, \beta) = \frac{1}{2\pi^3 a^2 R} \frac{1}{\left[e^2 - \left(\frac{R}{a} - 1\right)^2\right]^{1/2} [\sin^2 i - \sin^2 \beta]^{1/2}} \quad (9)$$

with the limits

$$a(1 - e) \leqslant R \leqslant a(1 + e), \qquad -i \leqslant \beta \leqslant i. \quad (10)$$

Here, $R = \sqrt{X^2 + Y^2 + Z^2}$ and $\beta = \arcsin(Z/R)$, where X, Y, Z are the Cartesian heliocentric coordinates. We normalized the above distribution to the total number of one particle with orbital elements (a, e, i). Equivalently, $S(R, \beta)\Delta X \Delta Y \Delta Z$ is the probability that the particle with orbital elements a, e, i is located within an infinitesimal box $\Delta X \times \Delta Y \times \Delta Z$ centered at (X, Y, Z).

The space density distribution given by Eq. (9) was illustrated in Sykes (1990) and shows why dust bands appear as essentially parallel lines above and below the ecliptic. The spatial density is non-zero in an annulus that is centered at the Sun. It is infinite at the limits of this annulus defined by Eq. (10). Using this density distribution, the brightness integral along the line of sight (defined by fixed l and b) is:

$$\int_{a,e,i} da\, de\, di \int_{r_{MIN}}^{r_{MAX}} dr\, r^2 \int_D dD\, F_j(D, r) N(D; a, e, i) S(R, \beta), \quad (11)$$

where r is the distance from the telescope, $F_j(D, R)$ is given by Eq. (7) for diameter $D = 2s$, $S(R, \beta)$ parameterized by a, e, i is given by Eq. (9), and R, β are functions of r as determined by geometry from the location and pointing direction of the telescope. $N(D; a, e, i)$ is the number of particles having diameter D and orbits with a, e, i. Here we switched to a commonly used notation where the size-frequency distribution is expressed in terms of D (see Section 3). The integral (11) was renormalized at singularities and evaluated numerically. We describe the integration method and test its accuracy in Appendix B.
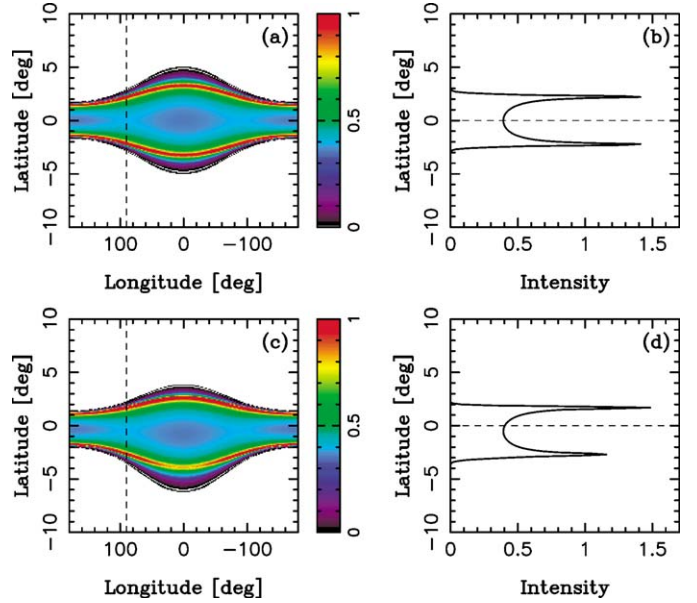

Fig. 6. Intensity in the 25-μm IRAS filter for $s = 50$ μm Karin particles in orbits with $a > 2$ AU. (a, b) Telescope was located at distance 1 AU from the Sun and in the invariant plane. (c, d) Telescope was moved to 0.02 AU above the invariant plane. $[l, b] = [0, 0]$ point in the longitude–latitude plane corresponds to the telescope pointing toward the opposition. The profiles on the right are given for $l = 90°$ corresponding to the direction toward the apex of Earth's motion (denoted by dashed lines in panels (a) and (c)). The IRAS surveyed the IR brightness within $\approx 30°$ to the apex (and the anti-apex). The forced orbital elements of Karin particles were set to zero to illustrate the symmetric case where both the southern and northern bands of maximum intensity have the same latitude offset from the invariant plane and are symmetrical with respect to $l = 0°$ (a, b). An observer displaced from the invariant plane in northward direction will see the dust bands shifted toward southern latitudes (c, d). The units of intensity used in these plots are arbitrary.

Fig. 6 illustrates the intensity profiles in the 25-μm IRAS filter calculated from Eq. (11) for Karin particles with $s = 50$ μm. Fig. 7 shows intensity profiles for $s = 5$, 50, and 500 μm Karin particles with olivine-like composition. These profiles have been normalized so that the emission cross-section is the same for all s. We do not plot here the results for pyroxene and low-temperature cosmic pyroxene because these profiles are similar to that of olivine. Relative to olivine (Fig. 7), radius $s = 5$ μm pyroxene grains show a $\approx 10\%$ stronger peak signal in the 12-μm filter and a $\approx 10\%$ weaker signal in the 60-μm filter. Conversely, the low-temperature cosmic pyroxene grains with $s = 5$ μm produce a $\approx 15\%$ stronger signal at the 60-μm wavelength than olivine. These variations can be readily explained by different emissivities of olivine, pyroxene, and low-temperature cosmic pyroxene.

Carbonaceous grains show signal intensities in IRAS filters that significantly differ from those of the silicate grains. Again, these results can be linked to their emission efficiencies and temperatures. For example, 'carbon1000' produces similar intensities in 12-, 25-, and 60-μm IRAS filters for all particle sizes. This is due to the capability of small carbonaceous grains with high carbonization degrees to thermally radiate at long wavelengths (Jäger et al., 1998). Conversely, small 'carbon400' grains radiate inefficiently at long wavelengths and produce weak signals in the 60-μm filter.
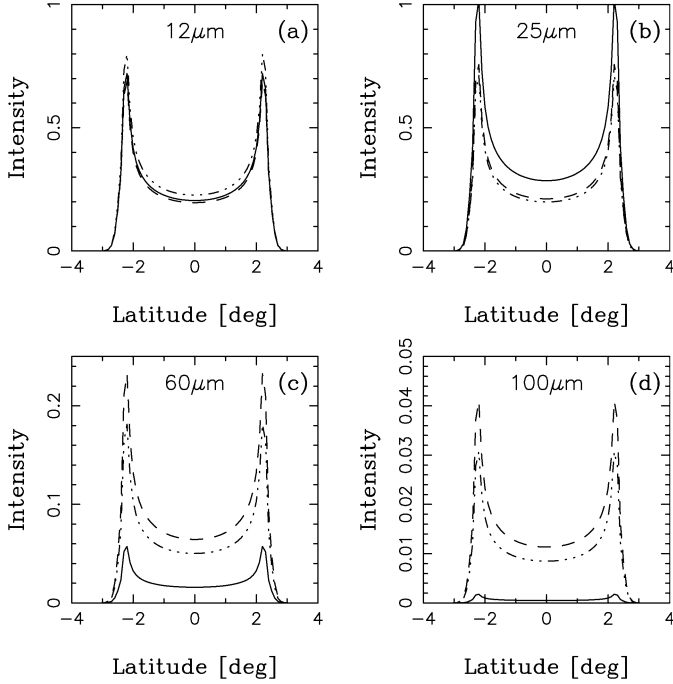
Fig. 7. Intensity in the IRAS filters for $s = 5$ μm (solid lines), $s = 50$ μm (dashed lines) and $s = 500$ μm (dotted lines) Karin particles: (a) 12-μm filter, (b) 25-μm filter, (c) 60-μm filter, and (d) 100-μm filter. Radiating particles were assumed to be isothermal spheres with olivine emission efficiency. The telescope was placed at distance 1 AU from the Sun and in the invariant plane. The intensity profiles are given for $l = 90°$ corresponding to the pointing direction of the telescope toward the apex of Earth's motion. The units of intensity used in these plots are arbitrary (are the same for all panels). The cross-sections of particles with different s were normalized to the same value.

Fig. 8. Intensity in the 25-μm IRAS filter for $s = 50$ μm Karin particles in orbits with $a > 2$ AU. We used $i_f = 0.5°$ and $\Omega_f = 25.4°$ for these plots; e_f and ϖ_f were set to 0. (a, b) Telescope was placed at distance 1 AU from the Sun and in the ascending node of the Earth's orbit with respect to the invariant plane. (c, d) Telescope was placed in the Earth orbit and 90° ahead of the Earth's ascending node. $[l, b] = [0, 0]$ point in the longitude–latitude plane corresponds to the telescope pointing toward the opposition. The profiles on the right are given for $l = 90°$ (solid line) and $l = −90°$ (dashed line) corresponding to the directions toward the apex and anti-apex of Earth's motion, respectively. The units of intensity used here are arbitrary.

The SIRT algorithm accounts for the fact that particles have non-zero forced elements. To account for the forced elements we assumed that

$$i \exp \iota \Omega = i_f \exp \iota \Omega_f + i_p \exp \iota \Omega_p \qquad (12)$$

and

$$e \exp \iota \varpi = e_f \exp \iota \varpi_f + e_p \exp \iota \varpi_p, \qquad (13)$$

where i, e, Ω, ϖ are the osculating orbital elements at the epoch of observation, i_f, e_f, Ω_f, ϖ_f are the forced elements, and e_p, i_p, Ω_p, ϖ_p are the proper elements. Here, i_f, e_f, Ω_f, ϖ_f are functions of the semimajor axis; e_p, i_p characterize the individual test orbits obtained via numerical integrations; and Ω_p, ϖ_p are assumed to have uniformly random distributions. These assumptions lead to a spatial distribution of particles that differs in several ways from Eq. (9).

The effect of i_f and Ω_f is simply a rotation by i_f of Kessler's distribution (Eq. (9)) around the forced nodal line. This can be demonstrated by rotating the reference frame into the forced plane where i_f vanishes and the density distribution is rigorously described by Eq. (9) with a, e_p, i_p. We account for this rotation in SIRT. As viewed from the Sun, these inclined Kessler distributions look like two enhancements in the IR brightness, one at negative and one at positive latitudes. The maximum positive latitude $\beta = i_p + i_f$ occurs at heliocentric longitude equal to Ω_f. The maximum negative lat-
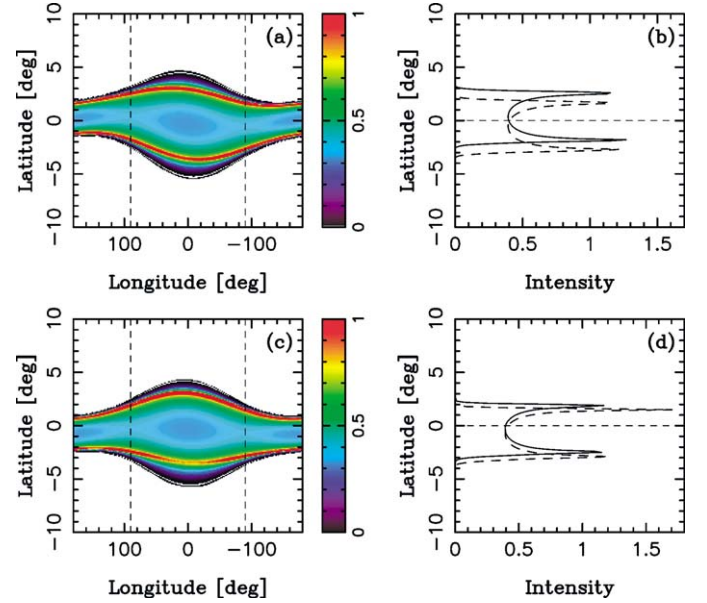
itude $\beta = −(i_p + i_f)$ occurs at heliocentric longitude equal to $\Omega_f + 180°$.

Fig. 8 illustrates these geometrical effects. It shows the intensity in the 25-μm IRAS filter for $s = 50$ μm Karin particles at $a > 2$ AU. We used this semimajor axis range here because the orbital distribution of particles at $a > 2$ AU is particularly simple and allowed us to separate the geometrical effect discussed above from more complicated orbital and projection effects for $a < 2$ AU.

In Figs. 8a and 8b, the telescope was placed at 1 AU and in the ascending node of the Earth's orbit with respect to the invariant plane. Following its orbital motion around the Sun, the Earth passes through this location on approximately January 6 each year when its heliocentric ecliptic longitude is ≈287°. We used a fixed forced inclination, $i_f = 0.5°$, and a fixed forced nodal longitude, $\Omega_f = 25.4°$, for particles at all a (numeric values given with respect to the invariant plane and opposition). These values approximate the forced elements for $a > 2$ AU at the current epoch.

Parameters i_f and Ω_f define the plane of symmetry for the dust bands. For an Earth-bound observer, the thermal emission radiated by these structures appears as two warped bands, one at southern and one at northern latitudes. In the example in Fig. 8a, the peaks of maximum brightness are symmetrical with respect to the invariant plane for solar elongations of ≈30° in the trailing direction and ≈150° in the leading direction, corresponding to the locations of descending and ascending nodes of the forced orbit, respectively. For large solar elongations, both

brightness peaks shift toward southern latitudes. For smaller solar elongations, the brightness peaks shift toward northern latitudes. The maximum latitudinal displacements of the northern and southern bands from the invariant plane are ≈3° and ≈3.8°, respectively. For 90° solar elongation in the leading direction, maximum brightness occurs at latitudes ≈2.6° and ≈ −2.0° in Fig. 8b.

In Figs. 8c and 8d, the telescope was placed in the Earth orbit, 90° ahead the Earth's ascending node. This configuration corresponds to the maximal distance of an Earth-bound observer from the invariant plane (in the positive z-axis direction). Corresponding to Earth's inclination with respect to the invariant plane of about 1.58°, this distance is ≈0.0276 AU. During its orbital motion, the Earth passes through this point on approximately April 8 each year when its heliocentric ecliptic longitude is about 17°. On April 8, an Earth-bound observer will see the dust bands from above at southern ecliptic latitudes. In the opposition direction, however, the forced plane of the dust bands rises above the ecliptic. This compensates for the viewing geometry effect so that the maximum southern latitude actually occurs at smaller b than in Fig. 8a.

Forced elements e_f and ϖ_f lead to several modifications of Eq. (9). The first effect is the displacement of the center of Kessler's distribution from the Sun. The new center is located at the point that is offset from the Sun's location by ae_f towards the aphelion of the forced orbit (i.e., towards $\varpi_f + 180°$). For $e_f = 0.05$ (typical value of the forced eccentricity at $a = 3$ AU), the magnitude of this offset is ≈0.15 AU. The second effect is a small flattening, $\approx \sqrt{1 - e_f^2}$, of the Kessler's torus in the direction of small axes of the forced orbit. This effect is typically small. For example, $e_f = 0.2$ produces only a 2% variation in distance of the inner edge of the deformed torus from the center. The third effect of e_f and ϖ_f is produced by faster orbital speeds of particles when they pass through pericenter of the forced orbit. This effect produces lower spatial density near ϖ_f where speeds are higher. Relative to ϖ_f, the fractional enhancement of particle density at $\varpi_f + 180°$ is $\approx 2e_f/(1 - e_f)$, or about 10% for $e_f = 0.05$.

Fig. 9 shows the effects of e_f and ϖ_f on brightness profiles measured by an observer at 1 AU. The principal effect is that the intensity becomes slightly larger in the direction toward the aphelion of the forced orbit where particles spend more time due to their slower orbital motion. Fig. 10 shows the intensity profiles for $e_f = 0.04$, $i_f = 0.5°$, $\varpi_f = 79.4°$, and $\Omega_f = 25.4°$. These profiles combine all effects discussed above including the warp, longitudinal variation due to the elliptic forced orbit, and projection to the observer's frame. In addition to these effects, the brightness profiles of IRAS dust bands are also affected by complex orbital dynamics of particles at $a < 2$ AU (Section 2.2) and by the variation of forced elements with a.

We used the particle-on-a-circle method (Hirayama, 1918; Dermott et al., 2001) to determine the variation of forced elements with a at 1983.5 for all orbits produced by our numerical integrations in Section 2.2. Figs. 11 and 12 show the forced elements for $s = 5$ and $s = 50$ μm Karin particles. The forced elements for $s = 500$ μm Karin particles (not shown here) are

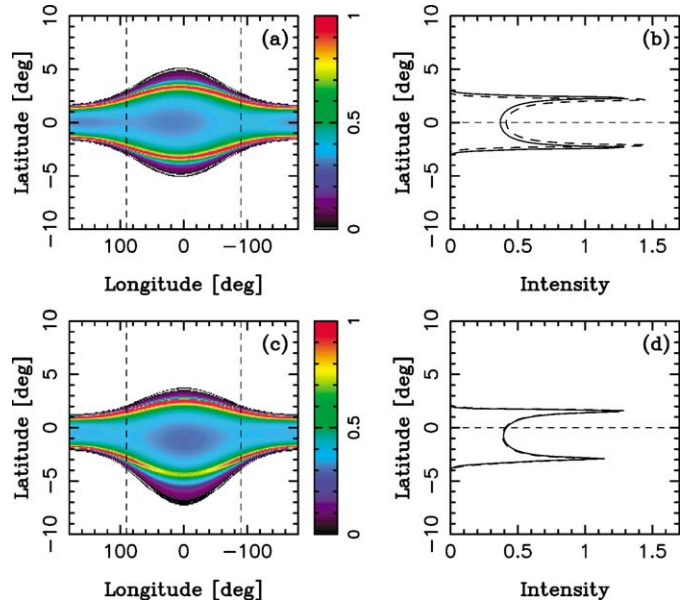Fig. 9. Intensity in the 25-μm IRAS filter for $s = 50$ μm Karin particles in orbits with $a > 2$ AU. We used $e_f = 0.04$ and $\varpi_f = 79.4°$; i_f and Ω_f were set to zero. (a, b) Telescope was placed at 1 AU and in the ascending node of the Earth's orbit with respect to the invariant plane. (c, d) Telescope was placed in the Earth orbit, 90° ahead of the Earth's ascending node. The profiles on the right are given for $l = 90°$ (solid line) and $l = -90°$ (dashed line) corresponding to the direction toward the apex and anti-apex of Earth's motion, respectively. These profiles are almost identical in (d). The units of intensity are arbitrary.
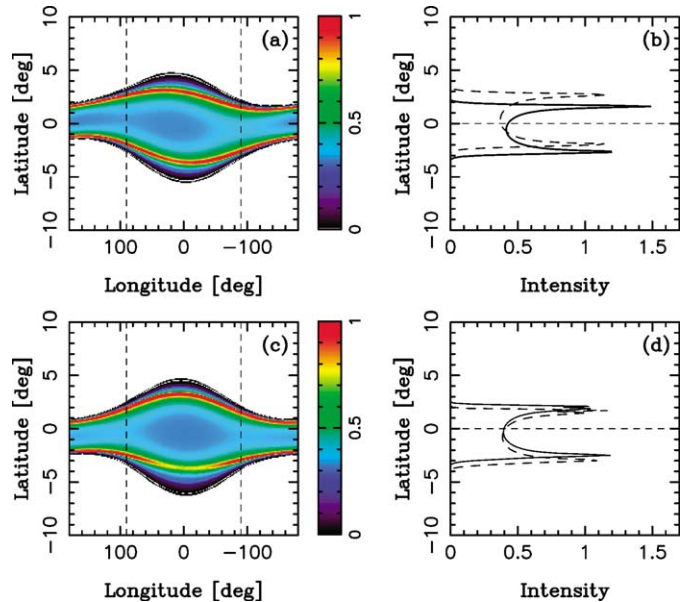

Fig. 10. The same as Figs. 8 and 9 but with $e_f = 0.04$, $i_f = 0.5°$, $\varpi_f = 79.4°$, and $\Omega_f = 25.4°$.

similar to those of $s = 50$ μm Karin particles except e_f for $s = 500$ μm has larger variation at $a \approx 2$ AU and i_f is less smooth as a function of a for $a \lesssim 2$ AU. The forced elements for Veritas particles (also not shown here) are similar to those of the Karin particles. In general, e_f and i_f become larger for larger s because these larger particles drift slowly over the res-
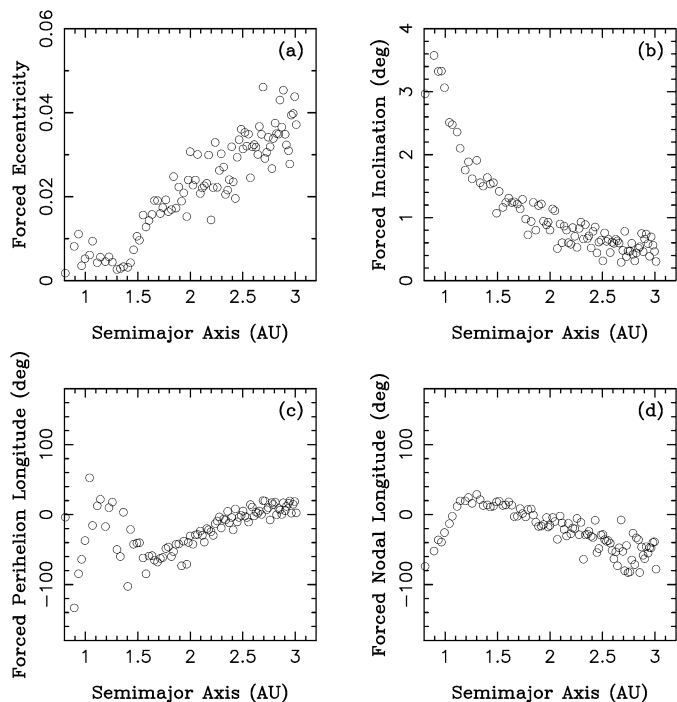
Fig. 11. Forced orbital elements at 1983.5 for $s = 5$ μm Karin particles. See text for the description of methods that we used to calculate these values. Angles are referred to the invariant frame.
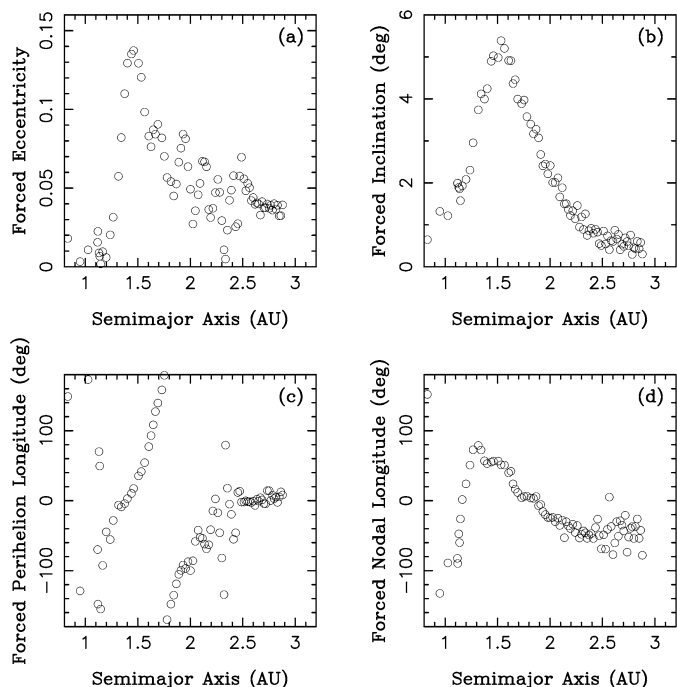

Fig. 12. Forced orbital elements at 1983.5 for $s = 50$ μm Karin particles. Angles are referred to the invariant frame.

onant locations and suffer larger orbital changes. These trends are similar to those determined by Grogan et al. (2001).

For $2 \lesssim a \lesssim 4$ AU, where low-e orbits are generally stable over long time spans, the forced orbital elements can be determined in the limit of large s by Fourier analysis. We integrated test orbits at $2 \lesssim a \lesssim 4$ AU and used the FMFT method (Šidli-

chovský and Nesvorný, 1997) to determine ten frequencies with largest amplitudes in $[e \cos \varpi, e \sin \varpi]$ and $[i \cos \Omega, i \sin \Omega]$. These integrations included the gravitational effects of planets and ignored drag forces. We identified and removed the Fourier terms that correspond to the proper terms. The remaining terms were vectorially added at 1983.5. We found good agreement between this determination of e_f, i_f, ϖ_f, and Ω_f and values calculated by the particle-on-a-circle method for $s \gtrsim 50$ μm. Small particles drift due to P–R drag on time scales that are comparable to time scales of planetary secular perturbations and tend to maintain values of the forced elements that characterize their starting location at ≈3 AU.

The overall trends seen in Fig. 12 for $a > 2$ AU are expected from analytic results derived from the secular theory where Jupiter acts as a sole perturbed on the particle orbit (Murray and Dermott, 1999). These results indicate that the forced orbit of a particle at large a is locked into Jupiter's osculating elements (Murray and Dermott, 1999, their Figs. 7.5 and 7.6). When referenced to the invariant frame, these values are $e_f = 0.049$, $i_f = 0.33°$, $\varpi_f = 15°$, and $\Omega_f = 317°$ at the 1983.5 epoch. The situation is more complicated for $a \lesssim 2$ AU because many mean motion and secular resonances exist in this region (Williams, 1979; Morbidelli and Henrard, 1991; Michel and Froeschlé, 1997; Gronchi and Milani, 2001). Rigorous parameterization of dynamics using standard proper and forced elements is inadequate at the resonant locations. The particle-on-a-circle method allows us to empirically parameterize the secular dynamics in this region by approximate means.

The uniform distribution of proper longitudes is a major approximation of the SIRT algorithm that allows us to speed up the calculation. As our tests show, this assumption is not strictly valid in cases where particles interact with resonances. For this reason, SIRT cannot be used to accurately simulate thermal emission from particle populations with strong longitudinal asymmetries. The effect of this approximation on the model predictions in this paper (Section 4) is unknown.

3. Application to IRAS data

The observational technique of IRAS caused it to scan the sky in circles of roughly constant solar elongation. By varying the elongation between 80° and 100° during the first 7 months of the 10-month mission, nearly the entire sky was mapped two times (Neugebauer et al., 1984). Each scan had a width of 0.5° and was shifted in ecliptic longitude by 0.25° on the subsequent orbit. During the last three months of the mission, a third map of the sky was attempted using a larger range of solar elongations (60°–120°). This map covered 72% of the sky before the satellite terminated operation.

We use here the IRAS Medium-Resolution (2-arcmin inscan) Zodiacal Observational History File (ZOHF) that consists of the time-ordered IRAS survey data averaged into $2'' \times 0.5°$ rectangular pixels along with pointing and timing information. These pixels contain the average of all detector samples in a given wavelength band summed over a time corresponding to a $2''$ scan. An explanation of the calibration and a statistical analysis of positions and fluxes can be found in Boulanger et

al. (1988). General information about the IRAS and its mission can be found in Neugebauer et al. (1984).

The data were stored in a large number of ASCII files, with each file listing the time of observation, pointing direction of the telescope, and fluxes detected in the four IRAS filters. The first and last scans were obtained on February 8, 1983 (JD 2445374) and November 21, 1983 (JD 2445661), respectively. To deal with this large amount of data, we selected 50 representative scans that met the following conditions. (1) We used scans that covered a continuous range of ecliptic latitudes from $b < -40°$ to $b > 40°$. We did not use incomplete scans. (2) We did not use scans that had gaps created when the telescope skipped over bright sources. (3) We did not use scans that showed strong IR emission from extrasolar sources such as the galactic plane, galactic cirrus, point sources, etc. (4) We required that our selected scans cover all values of ecliptic longitude and the available range of solar elongations. (5) We usually selected 2 or more scans with similar pointing geometry to see whether the flux-profile features seen for this geometry are robust. All scans were selected without the a priori knowledge of whether or not our model will produce good matches to them. Tables 2 and 3 list the selected scans and Fig. 13 shows their longitudinal distribution.

For each selected scan, we used the time associated with a pixel and determined the Earth's position at that time in ecliptic heliocentric coordinates using the JPL 403 ephemeris. The ZOHFs list the geocentric ecliptic latitude (b) and geocentric ecliptic longitude (l) of the pointing direction, both given for Equinox 1950.0, Epoch 1983.5. The geocentric ecliptic longitude is related to the solar elongation of observation (l_{SE}) and the geocentric ecliptic longitude of the Sun ($l_{\odot}$) through the relation $\cos(l_{SE}) = \cos b \cos(l - l_{\odot})$. We transformed all ecliptical coordinates from B1950.0 to the invariant reference frame using the algorithm described in Appendix A. We performed this transformation because the invariant frame is the primary reference frame of the SIRT.

Beichman and Wheelock (IRAS project note) showed that IRAS measurements at 60 and 100 μm were too bright relative to COBE/DIRBE (Diffuse Infrared Background Experiment) at large spatial scales. Since the IRAS mission was primarily designed to measure point sources and DIRBE was primarily designed to measure extended emission, we believe the COBE/DIRBE calibration is valid and the DIRBE results provide a check on the large scale performance of IRAS. A linear IRAS–DIRBE transformation was derived by Beichman and Wheelock based on carefully selected DIRBE data compared to IRAS scan data. We list this transformation in Table 4. The transformation shows that the IRAS–DIRBE calibration produces a 28% effect at 100 μm, 13% at 60 μm, and smaller effects at 25 and 12 μm. We calibrated and transformed the IRAS fluxes from Jy per steradian to W m^{-2} sr^{-1} according to Moshir (1989).

The zodiacal dust bands are low-contrast features in the background zodiacal light. A number of techniques have been proposed to extract these features from the IR flux measurements. Here we used the procedure developed and used by Reach et al. (1997) for the analysis of COBE data. This pro-

Table 2
Selected scans in the trailing direction; i.e., with the telescope pointing toward the anti-apex of Earth's motion

Id.	Scan file name	Pixels	Obs. time	Start lat.	End lat.	Longit.	Elong.
1	B_035_24.TAB	4680	2445378.1	81.02	−64.19	61.61	98.10
2	B_036_18.TAB	4750	2445378.6	81.05	−65.44	62.09	98.07
3	B_173_20.TAB	5114	2445447.0	82.83	−81.52	118.47	86.41
4	B_174_23.TAB	5158	2445447.6	83.51	−82.27	119.18	86.57
5	B_180_24.TAB	5354	2445450.7	87.08	−85.73	125.83	90.22
6	B_203_01.TAB	5296	2445461.7	85.83	−84.56	133.71	87.40
7	B_239_17.TAB	5302	2445479.9	85.80	−84.59	151.08	87.17
8	B_273_22.TAB	3156	2445496.9	51.79	−50.43	175.57	95.41
9	B_273_35.TAB	2932	2445497.1	48.20	−46.86	176.03	95.74
10	B_305_30.TAB	4298	2445513.1	71.06	−69.94	188.19	92.59
11	B_376_39.TAB	2614	2445548.7	43.09	−41.74	210.88	81.34
12	B_377_12.TAB	2940	2445548.8	50.02	−45.22	211.36	81.68
13	B_414_42.TAB	3266	2445567.6	53.40	−52.02	228.50	80.75
14	B_417_03.TAB	3852	2445568.7	62.68	−61.31	230.86	82.08
15	B_417_34.TAB	4074	2445569.0	66.22	−64.87	231.82	82.76
16	B_436_34.TAB	5060	2445578.7	63.84	−63.88	221.58	63.19
17	B_441_21.TAB	5048	2445580.9	65.48	−65.43	225.38	64.84
18	B_450_34.TAB	5182	2445585.6	66.81	−66.87	231.30	66.18
19	B_540_37.TAB	5400	2445630.6	84.98	−85.23	293.89	84.54
20	B_543_16.TAB	5578	2445631.8	86.06	−86.37	296.26	85.70
21	B_567_46.TAB	5572	2445644.1	85.33	−85.62	316.42	93.63
22	B_569_30.TAB	5598	2445644.9	85.04	−85.31	317.60	93.95
23	B_589_31.TAB	5586	2445654.9	88.19	−89.15	323.77	90.05
24	B_590_29.TAB	5426	2445655.6	88.12	−89.11	324.48	90.11

Columns are: (1) scan identification label; (2) scan file name; (3) number of pixels in the scan; (4) Julian Date epoch of observation; (5) starting ecliptic latitude of the scan; (6) ending ecliptic latitude of the scan; (7) ecliptic longitude of the pointing direction when scan crosses the ecliptic; (8) solar elongation. All angles are in degrees. Longitudes and latitudes are given for Equinox 1950.0, Epoch 1983.5. Longitudes for Equinox 2000.0 are about 0.64° larger than longitudes listed here. Ascending scans start with negative and end with positive values of the ecliptic latitude. Descending scans follow opposite paths. Scans are ordered by the observation date.

cedure uses a combination of high- and low-frequency Fourier filters. We modified the original filter of Reach et al. (1997) so that the filter profile in the frequency space smoothly approximates a step-like function (Guzzo and Benettin, 2001). Grogan et al.'s (2001) iterative method applied to the model/observed data with this filter produces the same result as a single application of filter on the model/observed data. We describe the Fourier filters in Appendix C and illustrate their application to IRAS data in Fig. 14.

Our filter has two adjustable frequency parameters, f_1 and f_2. Spatial frequencies smaller than f_1 and frequencies larger than f_2 are suppressed in the filtered signal. We used $f_1^{-1} = 15°$ and $f_2^{-1} = 1°$ to extract a noise-suppressed, high-frequency signal with enhanced spatial features in the latitudinal range between 1° and 15°. We also used $f_1^{-1} = 5°$ and $f_2^{-1} = 0.2°$ to better resolve the structure of the central bands.

The same filter, $\mathcal{F}$, was applied to the latitudinal profiles of the model IR flux, (F_{model}) and the observed IR flux (F_{obs}). The residual profiles, $R_{model} = \mathcal{F}(F_{model})$ and $R_{obs} = \mathcal{F}(F_{obs})$, can be directly compared. We adjusted the parameters in our model to produce R_{model} that provides the best fit to R_{obs}. Typically, R_{model} represents only a small fraction of the diffuse zodiacal cloud emission. To estimate this fraction, we calcu-

Table 3
Selected scans in the leading direction; i.e., with the telescope pointing toward the apex of Earth's motion

Id.	Scan file name	Pixels	Obs. time	Start lat.	End lat.	Longit.	Elong.
1	B_032_02.TAB	5490	2445376.3	−81.40	81.55	239.47	82.26
2	B_032_11.TAB	5568	2445376.5	−81.05	81.23	239.94	81.93
3	B_175_25.TAB	5074	2445448.1	−82.16	80.83	299.19	93.94
4	B_175_31.TAB	5104	2445448.2	−82.52	81.41	299.42	93.78
5	B_182_04.TAB	5488	2445451.3	−89.09	87.91	306.07	90.12
6	B_203_40.TAB	3522	2445462.2	−55.95	56.06	306.11	100.70
7	B_220_04.TAB	5578	2445470.3	−89.33	89.47	323.44	91.20
8	B_221_40.TAB	5382	2445471.3	−86.19	86.34	325.32	90.20
9	B_270_04.TAB	4994	2445495.3	−80.83	79.55	344.17	94.43
10	B_270_28.TAB	5132	2445495.6	−83.04	81.73	345.13	93.76
11	B_306_05.TAB	4922	2445513.3	−80.11	78.76	7.01	88.76
12	B_306_29.TAB	4270	2445513.6	−73.47	72.16	8.19	87.91
13	B_344_09.TAB	5104	2445532.4	−73.12	88.12	25.09	88.90
14	B_345_42.TAB	4000	2445533.1	−65.41	64.05	26.28	88.39
15	B_396_05.TAB	4620	2445558.3	−74.69	73.38	42.27	96.49
16	B_399_44.TAB	4954	2445560.1	−81.09	79.90	45.84	94.65
17	B_404_31.TAB	5606	2445562.6	−88.69	89.55	51.77	91.12
18	B_408_32.TAB	4244	2445564.6	−69.80	68.44	56.04	88.78
19	B_449_40.TAB	4732	2445585.1	−64.02	61.77	48.06	116.59
20	B_456_19.TAB	5142	2445588.4	−66.52	66.61	53.75	114.09
21	B_539_38.TAB	5516	2445630.1	−87.19	87.69	115.88	92.99
22	B_540_36.TAB	5596	2445630.6	−87.76	88.44	117.08	92.23
23	B_568_27.TAB	5628	2445644.5	−86.73	87.19	135.33	87.91
24	B_570_13.TAB	5624	2445645.4	−86.48	86.88	136.52	87.59
25	B_585_67.TAB	5544	2445653.2	−81.97	82.16	149.08	82.86
26	B_589_56.TAB	5542	2445655.2	−80.69	80.87	152.41	81.56

Columns are: (1) scan identification label; (2) scan file name; (3) number of pixels in the scan; (4) Julian Date epoch of observation; (5) starting ecliptic latitude of the scan; (6) ending ecliptic latitude of the scan; (7) ecliptic longitude of the pointing direction when scan crosses the ecliptic; (8) solar elongation. All angles are in degrees. Longitudes and latitudes are given for Equinox 1950.0, Epoch 1983.5. Longitudes for Equinox 2000.0 are about 0.64° larger than longitudes listed here. Ascending scans start with negative and end with positive values of the ecliptic latitude. Descending scans follow opposite paths. Scans are ordered by the observation date.

lated $\int F_{\text{model}} / \int F_{\text{obs}}$, where F_{model} is the best-fit (non-filtered) model and both integrals were evaluated over an adequate latitude range. Using this method, we determined the overall fraction by which sources of the asteroid dust bands contribute to the zodiacal cloud (Section 4).

Our best-fit results allowed us to constrain important model parameters and to determine physical properties of the asteroid dust bands and their sources. We summarize the main parameters of our models in the following:

(1) Factor f that determines the orbit dispersion of particles at their source families. Models with $f = 1$ correspond to the observed orbital dispersion of large family members; models with $f > 1$ use larger orbital spreads. We used $f = 1, 10, 20, 25, 30$, and 40 for the Karin cluster source and $f = 1, 2, 4$, and 8 for the Veritas family source.[7] Values of

f in the upper end of these intervals correspond to ejection speeds in excess of 500 m s^{-1}.

(2) Optical properties of dust grains. We used optical constants of five materials: iron-free olivine-like and pyroxene-like compounds, low-temperature pyroxene-like material with approximately cosmic abundance of metallic elements, and two carbonaceous materials differing by their carbonization degree (Dorschner et al., 1995; Henning and Mutschke, 1997; Jäger et al., 1998, 2003). We calculated the emissivity efficiency, ϵ, using Mie theory and determined the grain's temperature at distance R from the Sun from Eq. (6). We also used a parametrization of $T(R)$, where the temperature is given by an arbitrary power-law function of R (see Section 2.3).

(3) Size-Frequency Distribution (SFD) of the particles. We used two methods to define the SFD. In the first method (Sections 4.1 and 4.2.1), we assumed that the differential SFD can be represented by power-laws, $N(D) = N_0 D^{-\alpha}$, where N_0 is the calibration factor and α is the differential power-law index.[8] Each power-law SFD was assumed to be valid in the range $D_{\min} \leqslant D \leqslant D_{\max}$, where $D_{\min} \gtrsim 1$ μm and $D_{\max} \lesssim 1$ cm. The sub-micrometer particles are likely to be absent in the dust bands because they are removed on an orbital time scale by radiation pressure. $D > 1$ cm particles are unlikely contributors to the smooth profiles of the zodiacal light because they do not have enough surface area for their mass. In the second method, we used a Monte Carlo model for the collisional cascade to determine the SFD of particles as a function of their semimajor axis. This model is described in Section 4.2.2. We used nine logarithmic bins, D_j, $j = 1, \ldots, 9$, ranging from $\log D_1 = 0$ to $\log D_9 = 4$ (D in μm).

In this work, we attempted to match the high-frequency spatial profiles observed by the IRAS by only applying the particle populations from the Karin and Veritas families. We used these two and these two alone because, as described in the introduction, the Karin and Veritas families are best candidates for sources for the 2.1° and 9.3° dust bands, respectively. We are less certain about the source of the 1.4° IRAS dust band, with reasonable candidates being the large and ancient Themis family, smaller and younger Massalia family, or some yet-to-be-identified recent breakup (Nesvorný et al., 2003).

Mahoney-Hopping et al. (2004) have shown that the 1.4° dust band may represent a surface area that is a factor of $\gtrsim 10$ smaller than the combined surface area of particles in the 2.1° and 9.3° dust bands. If true, this would suggest that the 1.4° band can be treated as a small perturbation of the high-spatial-frequency IRAS profiles. For this reason, and given the computational expense of investigating all of its potential sources,

---

[7] The ejection velocity field for Veritas family members is strongly asymmetric as indicated by the distribution of large family members in proper element space. In particular, the component of the ejection velocity perpendicular to the orbital plane was ≈5 times larger than the other two components (Nesvorný et al., 2003). This stretched the Veritas family to its present width in inclination.

The Karin family was produced by a more symmetric ejection field with the velocities of large members $\lesssim 15$ m s^{-1} (Nesvorný et al., 2002).

[8] Alternatively, the spectrum of particles can be described by their cumulative mass distribution, $N(> M) \propto M^{-\gamma}$, where $\gamma = (\alpha - 1)/3$ (McDonnell et al., 2001). For a particle with an irregular shape, D defines the effective diameter of a sphere with the corresponding volume.
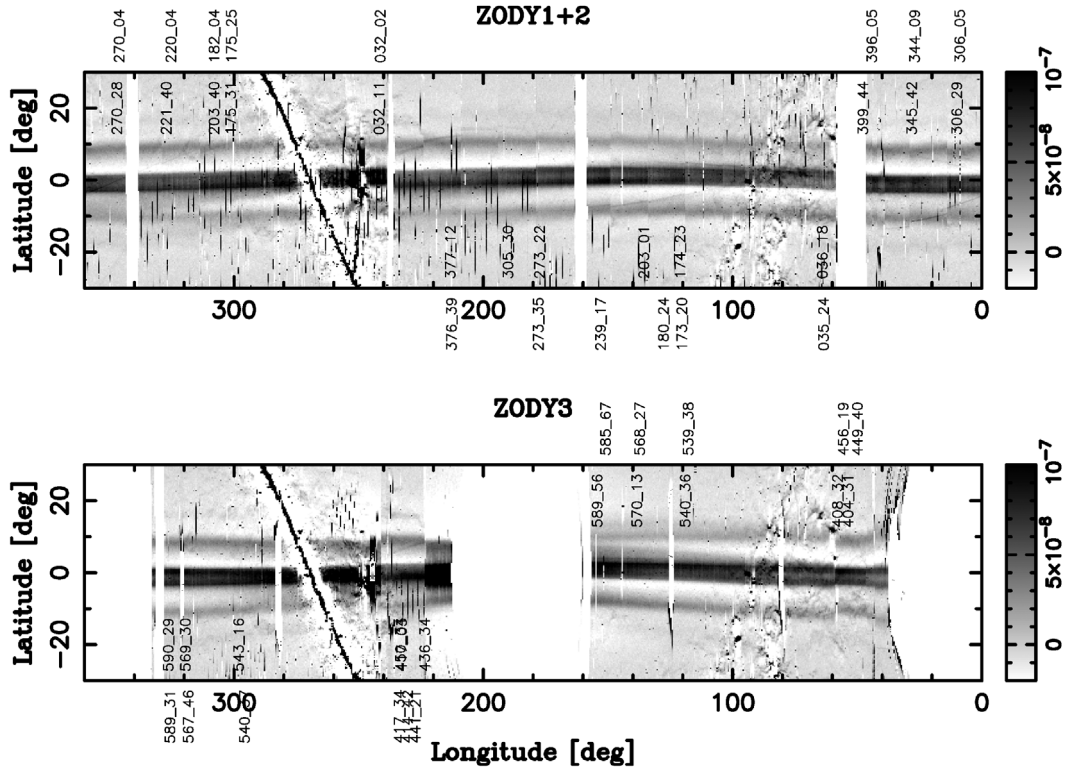
Fig. 13. Zodiacal dust bands are shown in this image constructed from 25-μm IRAS scans. The medium-resolution data were Fourier-filtered using the procedure described in the text to enhance high-frequency spatial features in ecliptic latitude. The dust bands appear as longitudinally extended features of IR emission that are roughly parallel to the ecliptic. The bright central bands consist of two band pairs that are unresolved in this image (Sykes, 1986). Tempel 2, Encke, and several other cometary trails appear as faint, thread-like IR sources (labeled in Fig. 2 of Sykes, 1990). The diagonal features at longitudes ≈90° and ≈270° are the galactic plane emission. We avoid these longitude values for comparisons with our model results. Labels denote the longitude values of fifty selected scans that we list in Tables 2 and 3. Labels printed in upper parts of panels denote scans in leading direction; labels in lower parts are trailing scans. Units of flux are W m^{-2} sr^{-1}.

Table 4
IRAS–DIRBE transformation given by Beichman and Wheelock (IRAS project note)

Wavelength (μm)	Gain	Offset (MJy sr^{-1})
12	1.06 ± 0.02	-0.48 ± 0.43
25	1.01 ± 0.02	-1.32 ± 0.74
60	0.87 ± 0.05	0.13 ± 0.65
100	0.72 ± 0.07	-1.47 ± 0.88

We use this transformation to calibrate IRAS flux measurements: $I_{\text{calib}} =$ Gain $\times I_{\text{IRAS}} +$ Offset, where I_{IRAS} and I_{calib} are the original and calibrated flux densities, and Gain/Offset are listed in the table.

we save an analysis of this band for a future study. If, on the other hand, the contribution of the 1.4° dust band is for some reason larger than that suggested by Mahoney-Hopping et al. (and more comparable to that suggested by Grogan et al., 2001), some of our results could be affected by that. For example, by attempting to fit both inner band pairs by a single source, our model may try to artificially adjust the dispersion of Karin particles by using large values of f. We will discuss this effect at relevant parts of the text below.

Our best fits discussed in the following text may not be unique. The best we can do is to vary the free parameters of the model, check which combinations of the parameters fit data and which do not. Given the number of model parameters and the CPU time available to us, however, we were unable to check

all combinations. It is possible that we missed some that would produce comparably good fits to those found or even better ones.

4. Results

In general, $N(D)$ is controlled by the production rate $P(D)$ of diameter D particles produced in the source by disruptive collisions and by the collisional lifetimes of drifting particles τ_{col}. $P(D)$ is defined here as the number of particles in the diameter range $(D, D + dD)$ produced per unit time interval. It accounts for the production at source of $D < 1$ cm particles by breakups of $D > 1$ cm objects. $P(D)$ decays with t over the source family age.

We analyzed two models that differed according to our choice of τ_{col} and $P(D)$. In Section 4.1 (Model I), we assumed that $\tau_{\text{col}} > \tau_{\text{dyn}}$ for all $D \leqslant 1$ cm, where τ_{dyn} is the dynamical lifetime of particles (Section 2.2), and that $P(D)$ does not change with time. With these assumptions, $D \leqslant 1$ cm particles are created at a constant rate in the source. We assume they orbitally evolve into a dynamical sink or survive to the present time. Consequently, the SFD slope is approximately constant with a in Model I.

In Section 4.2 (Model II), we allowed the dust particles to collisionally disrupt. After each disruption event, we tracked the daughter fragments in orbits with $0.5 \lesssim a \lesssim 3$ AU. In ad-
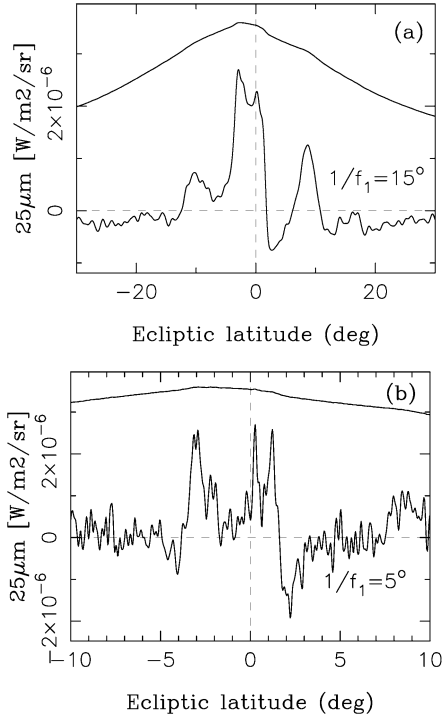
Fig. 14. Fourier filter applied to the original IRAS profile in the 25-μm wavelength ($F(b)$, scan 180_24, upper solid lines in both panels) allowed us to extract high-frequency brightness features that are produced by the asteroid dust bands ($R(b)$, bottom solid lines). (a) $f_1^{-1} = 15°$ and $f_2^{-1} = 1.0°$. With these parameter values the outer band pair appears in the residual profiles as broad peaks at latitudes $\approx -10°$ and $\approx 8°$. The two central band pairs are under-resolved and produce the central, double-peaked hump. (b) $f_1^{-1} = 5°$ and $f_2^{-1} = 0.2°$. The central band pairs are now better resolved. The sharp peaks at latitudes $\approx -3°$ and $\approx 1.2°$ are produced by the Karin dust band. $R(b)$ were scaled up by a factor to clearly appear in the range of this plot.

dition, we allowed $P(D)$ to decay with time over the source family's age. Because of the complexity of the collisional cascade as well as the difficulty in tracking the orbital evolution of numerous collisional fragments with the N-body code, we did not account for collisions in our numerical integration work (Section 2.2). Instead, we assumed that the SFD changes with a according to prescriptions based on empirical arguments and Monte Carlo simulations of the collisional cascade. Model I has the advantage of being defined by a small number of parameters. Model II, while likely to be more realistic, is more difficult to uniquely constrain from IRAS observations.

In the following text, we will discuss Models I and II in order of their increasing complexity. First, we will describe models with the constant-slope SFD for all D and a (Section 4.1.1) and models that use a broken-slope SFD (Section 4.1.2). In an attempt to improve fits to IRAS scans with small elongation, we will then move to models that use empirical weighting factors to produce SFDs that change with a (Section 4.2.1). Finally, we will describe models where the SFDs are defined by a Monte Carlo model of the collisional cascade (Section 4.2.2). These latter models realistically account for the effects of disruptive collisions in orbitally evolving particle populations.

To determine the quality of our fits we used the standard χ^2 method for $-15° < b < 15°$. To define χ^2, we assumed that

the RMS uncertainty of IRAS measurements of the spatially extended IR emission was 10^{-8} W m^{-2} sr^{-1}. We did not use data with $b < -15°$ and $b > 15°$ because the filtered signal is weak at these latitudes. In the following text, we do not list the numeric value of χ^2 for every studied model. Instead, we verbally describe the quality of the fit. By definition, our good fits correspond to $\chi^2 \lesssim 1$ (χ^2 was normalized by the number of measurements used to obtain the fit), our bad fits correspond to $\chi^2 > 1.5$. The best fits obtained in Section 4.2.2 have $\chi^2 \approx 0.8$. We favor these best-fit models over those with $\chi^2 > 1$ and carefully choose our wording to indicate in each specific case whether (or not) the difference in χ^2 is significant.

We used IRAS observations in 12-, 25-, and 60-μm wavelengths to constrain our fits. The signal in the 100-μm IRAS filter is noisy and contains emission from extrasolar sources. We also examined the model profiles in the 100-μm IRAS filter to see whether they could tell us something about the distribution of particles at large a. For completeness, we show these profiles in the figures.

4.1. Model I

To start with, we neglected the effect of collisions and assumed that the physical lifetime of particles was equal to their dynamical lifetime, $\tau_{dyn}(D)$. We determined $\tau_{dyn}(D)$ from our numerical integrations. As explained in Section 2.2, $\tau_{dyn} \propto D$ for $D \gtrsim 10$ μm and deviates from this functional dependence at $D \lesssim 10$ μm because τ_{dyn} can be significantly extended in this size range by resonant captures. Using this assumption, and if $P(D)$ of sources were constant in time over their entire lifetimes, $P(D) \propto N(D)/D$ for $D \gtrsim 10$ μm. Once $N(D) = N_0 D^{-\alpha}$ is determined from best fits to the observation data, the size spectrum of particles produced in the source is $P(D) \propto D^{-(\alpha+1)}$. In reality, however, $P(D)$ is likely to drop with time (Bottke et al., 2005; Farley et al., 2006). If so, the link between $N(D)$ determined from IRAS data and the time-dependent production efficiency of sources becomes more complicated. We will analyze models with time-dependent $P(D)$ functions in Section 4.2.2.

We have experimented with different temperature profiles $T(R)$ described in Section 2.3. Models with $T(R) \propto R^{-0.5}$ provide poor fits to the data. Most notably, the model signals are about 30% weaker for $b \approx 0°$ than the observed residual signals in the 12-μm IRAS filter. Apparently, these models lack important emission from a population of hot, near-ecliptic dust particles. The best fits occur for $T(R) = 275 R^{-\delta}$ K with $0.25 \leqslant \delta \leqslant 0.35$. The low values of δ in this range may be physically implausible. On the other hand, several authors suggested $\delta \approx 0.35$ (e.g., Dumont and Levasseur-Regourd, 1988; Renard et al., 1995; Leinert et al., 2002). For this reason, we used $\delta = 0.35$ for the near-ecliptic dust (modeled here as the Karin particles) in the rest of this paper. We will discuss the plausibility of this assumption in Section 5. Because the χ^2 values of our best fits are insensitive to $T(R)$ assumed for the outer dust band (contributed by Veritas particles), we adopted $T(R)$ as determined from Eq. (6) for the outer band. Except for

$D < 10$ μm Veritas particles, $T(R) \approx 275/\sqrt{R}$ K in this case (Section 2.3).

4.1.1. Model with constant SFD slope for 1 μm $\leqslant D \leqslant$ 1 cm

In our first modeling effort, we assumed that $f = 1$ and that $D_{min} = 1$ μm and $D_{max} = 1$ cm. We used optical properties of low-temperature cosmic pyroxene (see Section 4.1.3 for definition) and determined $N(D)$ of Karin and Veritas particles that produce fits with the smallest χ^2 values. For the reasons that will be described in Section 4.1.3, we attempted to match only the IRAS scans with $l_{SE} \geqslant 90°$. The results were in many ways unsatisfying ($\chi^2 > 2$). Most notably, these models show two sharp peaks at $|b| < 5°$ that poorly match the central hump in the observed signal. Conversely, the model provides a good match for the outer band pair: the location and shape of the two corresponding brightness peaks at $|b| \approx 10°$ are similar to IRAS data.

Before moving to more complex models, we experimented with f to determine how it effects our results. We found that the peaks corresponding to the central band pair become increasingly rounded and the central dip becomes shallower with increasing f. For Veritas particles, the peaks at $b \approx \pm 10°$, corresponding to the outer band pair, also become more rounded with the increasing f and shift slightly to smaller $|b|$ (cf. Grogan et al., 1997).

Karin particles with $f \approx 20$ offer an interesting possibility to improve our fits to the IRAS profiles near $b = 0°$. Our fits with $f = 1$ provide a poor match with the filtered IRAS profiles at small latitudes because they produce two sharp peaks and a deep dip at $b \approx 0°$. The conventional wisdom is that we are missing a third source at $b \approx 0°$ (e.g., the Themis or Massalia family). Using Themis family particles, Grogan et al. (2001) was able to match the IRAS scans at $b \approx 0°$ better. On the other hand, Mahoney-Hopping et al. (2003) was also able to fit the IRAS scans at $b \approx 0°$ without using a strong third source with $i \approx 0°$. This suggests there may be a problem with the uniqueness of these fits. In the following, indexes 'K' and 'V' denote parameters of Karin and Veritas particles, respectively.

By using $f_K > 20$, we shift the location of the two central peaks toward smaller $|b|$ while shrinking the central dip. The observed IRAS profile, however, has its two central peaks at larger latitudes and its central dip at $b \approx 0°$ is not as pronounced. This difference is reflected in the larger χ^2 of the fit. Because these differences are systematic and appear in comparisons with all IRAS scans having $l_{SE} \gtrsim 90°$, we find that $f_K \lesssim 20$. A more detailed analysis has shown that $f_K \approx 20$ provide best fits. See Section 5 for a discussion and interpretation of this relatively large value of f_K.

Similar constraints may be placed on f_V. With $f_V \gtrsim 4$, the latitudinal locations of the peaks corresponding to outer band pair are shifted by $\approx 1°$ from their observed latitudes toward smaller $|b|$. With $f_V = 8$, the peaks occur at $b \approx \pm 10°$ and become more rounded than the observed ones. Similar discrepancies between $f_V \gtrsim 4$ models and IRAS data occur for all of the scans in Tables 2 and 3 with $l_{SE} \gtrsim 90°$. Thus, we find that $f_V < 4$. Models with $f_V = 2$ produce fits that are similar to those obtained with $f_V = 1$.

Taken together, these experiments suggest that $f_K \approx 20$ (corresponding to $\Delta i \approx 1.8°$) and $f_V \approx 1$–2 (corresponding to $\Delta i \lesssim 1°$). These values set an upper limit on the ejection speeds of particle precursors from the Karin and Veritas families. Conceivably, the smallest precursor bodies included $D \sim 1$–10 cm meteoroids. While these upper limits on ejections speeds are firmly set by this argument, the exact interpretation of f_K depends on the contribution to f_K of the third, innermost band pair. If its contribution is substantial, the values of f_K determined here cannot be used to further narrow down the range of ejection speeds for the Karin meteoroids. We discuss this issue in Section 5.

Our fits suggest values of α_K and α_V between ≈ 2.0 and 3.2. These values of α are comparable to those determined by Grogan et al. (2001), who found $\alpha \approx 2.3$ for $4 \leqslant D \leqslant 100$ μm. Like Grogan et al., we found that the upper bound on α at 3.2 is well defined. Conversely, our lower bound of $\alpha \approx 2.0$ is fuzzy because our χ^2 values yield comparable α values over a range of $\alpha \sim 2.0$ (see Fig. 15 in Grogan et al., 2001).

Steep SFDs with $\alpha \gtrsim 3.2$ produce weak model signals in the 60-μm IRAS filter. For example, a steep model SFD with $\alpha = 3.3$ is $\approx 50\%$ deficient in flux at 60 μm relative to the flux at 12 and 25 μm. Note that most of the surface area in steep SFDs is produced by small particles that inefficiently radiate at long wavelengths. Shallow SFDs with $\alpha \lesssim 2.0$ include too many large particles at $a > 2$ AU. Because these particles tend to stay tightly clustered in inclination, they produce sharp, double-peak latitudinal profiles that are not observed. Large particles with $a < 2$ AU tend to spread to large i (Figs. 1 and 2) and hence do not contribute to the small-scale features seen in the filtered model profiles. Apparently, at least some contribution from small particles is needed to get a reasonable match between model and data.

With $f_K = 20$, $f_V = 1$ and $\alpha_K = \alpha_V = 2.8$ (Fig. 15), we found $S_K = 1.9 \times 10^{10}$ km^2 and $S_V = 3.3 \times 10^{10}$ km^2 in particles with 1 μm $\leqslant D \leqslant$ 1 cm (Model I in Table 5). These values vary between 1.3 to 1.9×10^{10} km^2 for Karin particles and 1.8 to 4.8×10^{10} km^2 for particles for $2.0 \leqslant \alpha \leqslant 3.2$, with lower values corresponding to $\alpha \approx 2.0$. The increased contribution of Karin particles relative to the case with $f_K = 1$ reflects the fact that Karin particles with $f_K = 20$ account for a larger part of the IR emission in the central peak. With $f_K = 20$ and $f_V = 1$, $S_K/S_V \approx 0.58$. This ratio varies between 0.4 and 0.72 for $2.0 \leqslant \alpha \leqslant 3.2$.

These values are much larger than the cross-sectional surface areas determined by Grogan et al. (2001). They found $\approx 0.7 \times 10^9$ km^2 for the central dust bands and $\approx 4.0 \times 10^9$ km^2 for the outer dust band for particles with $4 \leqslant D \leqslant 100$ μm. Our models described in Section 4.2.2 suggest S_K and S_V are a factor of ≈ 2 smaller than the values determined here, although these values are still about a factor of ≈ 5 larger than the ones found by Grogan et al. (2001).

The difference between Grogan et al.'s estimates and ours is that Grogan et al. determined the cross-sectional area of particles with $a > 2$ AU only. These particles preferentially contribute to high-frequency spatial features in the IRAS scans. Conversely, because our model allowed us to solve for this pa-
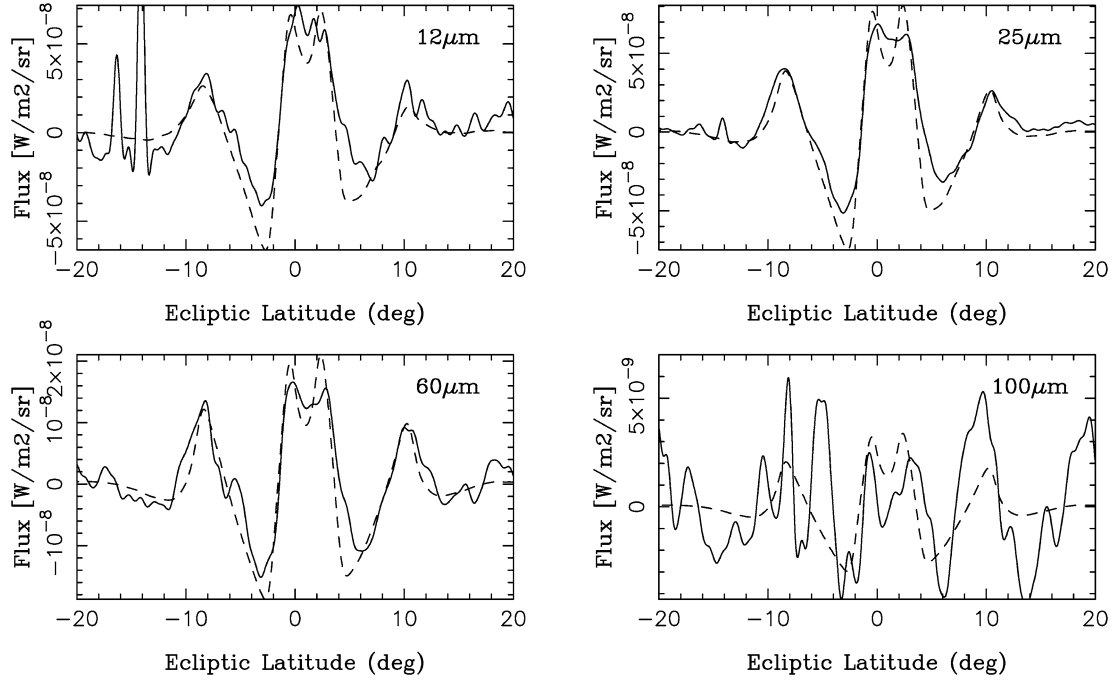
Fig. 15. Illustration of Model I that uses single power-law SFD for 1 μm $\leqslant D \leqslant$ 1 cm. The panels show a representative IRAS scan (180_24; Table 3) in 12-, 25-, 60-, and 100-μm wavelengths. We assumed $f_K = 20$ and $f_V = 1$ and a power-law SFD with $\alpha = 2.8$ for 1 μm $\leqslant D \leqslant$ 1 cm for both Karin and Veritas particle populations. The plot shows the residual IRAS (solid lines) and model (dashed lines) profiles after background has been removed from both signals by Fourier filter with $f_1^{-1} = 15°$ and $f_2^{-1} = 1°$. The hump in the IRAS profile at $b \approx -5°$ is a cometary trail (Sykes, 1990). This hump becomes stronger with increasing wavelength which suggests thermal emission from large R.

Table 5
Physical properties of the dust bands

	Model I							Model II		
	Constant slope			Broken slope						
	(1)	(2)	(3)	(4)	(5)	(6)	(7)	(8)	(Gl)	(Gi)
D_{break} (μm)	–	–	–	50	100	200	400	100		
α_K	2.8	2.0	3.2	2.1	2.2	2.3	2.4	2.2	≈ 2.5[a]	≈ 2.2[a]
α_V	2.8	2.0	3.2	2.1	2.2	2.3	2.4	2.2	≈ 2.5[a]	≈ 2.2[a]
χ^2	1.0	1.5	1.3	0.94	0.81	0.85	0.96	1.1	1.2	**0.80**
N_K (10^{22} μm^{-1})	6.8	0.18	11	25	20	15	14	25	–	–
N_V (10^{22} μm^{-1})	12	0.25	28	56	29	20	17	35	–	–
N_K (>30 μm) [10^{23}]	11	0.54	15	38	39	32	30	50	57	**54**
N_V (>30 μm) [10^{23}]	19	0.74	38	85	57	42	35	68	140	**110**
S_K (10^9 km^2)	19	13	19	17	17	19	25	22	4.4	**6.7**
S_V (10^9 km^2)	33	18	48	37	26	25	29	30	12	**14**
S_K/S_V	0.58	0.72	0.40	0.45	0.68	0.78	0.84	0.73	0.37	**0.48**
D_K (km)	37	43	23	19	18	18	20	20	9.7	**11**
D_V (km)	44	48	31	25	21	19	21	22	14	**14**
M_K (10^{18} g)	51	84	12	7.6	6.3	6.0	8.3	8.1	0.96	**1.4**
M_V (10^{18} g)	88	115	30	17	9.2	7.7	9.9	11	3.1	**2.9**
M_K/M_V	0.58	0.72	0.40	0.45	0.68	0.78	0.84	0.73	0.31	**0.49**

The rows are: diameter of the SFD slope break (D_{break}); power indexes for $D \leqslant D_{\text{break}}$ (α_K and α_V); normalized χ^2 indicating the quality of a fit; SFD calibration factors for $D = 30$ μm (N_K and N_V); number of particles with $D > 30$ μm (N_K (>30 μm) and N_V (>30 μm)); cross-sectional surface areas (S_K and S_V); their ratio (S_K/S_V); diameter of a sphere with required volume (D_K and D_V); required masses (M_K and M_V); and their ratio (M_K/M_V). Indexes 'K' and 'V' denote the parameters of Karin and Veritas particles. We used density 2.0 g cm^{-3} for Karin and Veritas particles to calculate M_K and M_V. Different models are denoted by labels: (1)–(3) are models with a constant value of α for 1 μm $\leqslant D \leqslant$ 1 cm; (4)–(7) are models with a broken slope at D_{break}, (8), (Gl), and (Gi) are models that allow the SFD change with a. All models listed here use $f_K = 20$ and $f_V = 1$. The individual models are: (1) $\alpha = 2.8$; (2) $\alpha = 2.0$; (3) $\alpha = 3.2$; (4) $D_{\text{break}} = 50$ μm and $\alpha_K = \alpha_V = 3.5$ for $D > D_{\text{break}}$; (5) the same as (4) but $D_{\text{break}} = 100$ μm; (6) the same as (4) but $D_{\text{break}} = 200$ μm; (7) the same as (4) but $D_{\text{break}} = 400$ μm; (8) the same as (5) but with $\beta = 0$ (Section 4.2.1); (Gl) model with $\tau_{\text{col}}^{\text{Gl}}(D, R)$, $\gamma = 3.0$ and $\tau_P = \infty$; and (Gi) the same as (Gl) but with $\tau_{\text{col}}^{\text{Gi}}(D, R)$. Values corresponding to our preferred model, (Gi), are denoted in bold. We used optical properties of low-temperature cosmic pyroxene (Henning and Mutschke, 1997) for all these models.
[a] Approximate values of α for $10 < D < 50$ μm and $a \approx 2$ AU.

rameter, we determined the *total* cross-sectional surface areas of all particles from the Karin and Veritas families, including those with $a < 2$ AU. As such, our S_K and S_V values represent the total contributions of the Karin and Veritas families to the dust environment in the Solar System.

One parameter that we can compare with Grogan et al. (2001) is the ratio of cross-sectional areas of particles in the central and outer IRAS bands. Using our simple model with $f_K = 20$, $f_V = 1$, $D_{min} = 1$ μm, and $D_{max} = 1$ cm, we found that $S_K/S_V \approx 0.6$. This value is relatively insensitive to our choice of α, provided it is within the range described above ($S_K/S_V \approx 0.4$–0.7 for $2.0 \leqslant \alpha \leqslant 3.2$). In contrast, Grogan et al. computed that the outer band represents 5–10 times more cross-sectional area than the inner band pair. We do not yet understand this difference. We hypothesize that the improved dynamical runs and/or some of the features used by our model allow us to determine a more complete picture of the central and outer bands than has been previously put together.

Our constant-α models with $D_{min} = 1$ μm and $D_{max} = 1$ cm are flawed because they predict excessively large volumes (and masses) of material. With $\alpha_K = \alpha_V = 2.8$, we found that the required volumes in $D \lesssim 1$ cm particles are equivalent to spheres of $D \approx 37$ km and $D \approx 44$ km for the inner and outer dust bands, respectively. These estimates account for all particles originating in the bands, including those with $a < 2$ AU that become dispersed into the background. This volume is clearly impossible for the Karin band because (i) the parent body of the Karin family was $D \approx 30$ km and (ii) a significant portion of the ejected material was proportioned into the observed family members (Nesvorný et al., 2005b). Based on these results, we believe that the constant-α models cannot characterize the SFD distribution of particles over the size range considered here (1 μm $\leqslant D \leqslant 1$ cm).

4.1.2. Model with broken SFD slope at D_{break}

With α constant for 1 μm $\leqslant D \leqslant 1$ cm, we needed an excessive volume of material to explain the observed IR brightness of the inner band pair. This makes us believe that the SFD of particles from the dust bands cannot be characterized by a single value of α for 1 μm $\leqslant D \leqslant 1$ cm. By experimenting with D_{max}, we found that our fits improved when $D_{max} \sim 50$–400 μm, i.e., when we suppressed the contribution of $D > 400$ μm particles. These test models predict shallow SFD slopes for $D < D_{max}$. Motivated by this result, we tested two values of α: one for $D \lesssim D_{break}$ and one for $D \gtrsim D_{break}$. We treated D_{break} as a free parameter.

We found that the best match between model and data occurred for $50 \lesssim D_{break} \lesssim 400$ μm. To obtain these matches, we used the power-law index $\alpha \gtrsim 3.5$ for $D > D_{break}$ for both bands. With $\alpha < 3.5$ for $D > D_{break}$, the model profiles become similar to those obtained with the constant slope for all D (Section 4.1.1). The upper limit on α for $D > D_{break}$ is not well defined but values ≈ 3.5 produce better fits than $\alpha \gg 3.5$. The values of D_{break} described above are comparable to those determined using more realistic models (see Section 4.2.2).

For the models described in this section, we found that $\alpha_K = \alpha_V = 2.2 \pm 0.5$ for $D \leqslant D_{break}$ produce our best fits to the data.

The power-law index for $D \leqslant D_{break}$ cannot be larger than ≈ 2.8 because the model signal in the 60-μm wavelength becomes weak with $\alpha > 2.8$. The lower bound on α for $D \leqslant D_{break}$ is not sharply defined because different models yield comparable values of χ^2 over a wide range of α values ranging down to $\alpha = 1.5$.

Fig. 16 ($f_K = 20$ and $f_V = 1$) shows representative fits with $\alpha_K = \alpha_V = 2.2$ for $D \leqslant D_{break} = 100$ μm and $\alpha_K = \alpha_V = 3.5$ for $D > D_{break}$. These fits have comparably small χ^2 values to our previous best fits using a constant α over our D range. We note that the observed shallow dip for $b \approx 5°$ is better matched by the model than in Fig. 15. The difference between our model and the observed profiles at $b \approx -5°$ in Figs. 15 and 16 can be blamed, at least in part, on the presence of a cometary trail that produces a hump in IRAS scan 180_24 at $b \approx -5°$ (Sykes, 1988).

The broken-slope model with $f_K = 20$ and $f_V = 1$ (Fig. 16) is one of the best model fits we have found to date with Model I assumptions. It produces the correct latitudinal locations and widths of the brightness peaks at $b \approx 0°$ and $b \approx \pm 10°$. Figs. 17 and 18 show comparisons between this model and IRAS scans for various ecliptic longitudes and $l_{SE} \gtrsim 90°$. The model fits the data reasonably well for all longitudes, though in some cases it tends to produce a slightly weaker signal than observed.

With $f_K = 20$ and $f_V = 1$, $\alpha_K = \alpha_V = 2.2$ for $D \leqslant 100$ μm and $\alpha_K = \alpha_V = 3.5$ for 100 μm $< D \leqslant 1$ cm, our best-fit model yields $N_K = 2.0 \times 10^{23}$ μm^{-1} and $N_V = 2.9 \times 10^{23}$ μm^{-1}, $S_K = 1.7 \times 10^{10}$ km^2, $S_V = 2.6 \times 10^{10}$ km^2, and $S_K/S_V \approx 0.7$ (Model 5 in Table 5). The ratio S_K/S_V varies between 0.4 and 1.0 when α for $D \leqslant 100$ μm is set to values between 1.5 and 2.8. The total volume of particles with 1 μm $\leqslant D \leqslant 1$ cm were found to be equivalent to spheres with diameters $D \approx 18$ km and $D \approx 21$ km for the inner and outer bands, respectively. These volumes are much smaller than volumes predicted by our models using a single value of α and are clearly more plausible when compared to the size of the parent body of the inner band pair.

Using our best-fit model parameters, we can estimate the contribution of Karin and Veritas particles to the total brightness of the zodiacal cloud emission. As described in Section 3, we calculate these contributions as $\int F_{model} / \int F_{obs}$, where F_{model} and F_{obs} are the model and observed (non-filtered) fluxes. The flux integrals are evaluated over $-50° \leqslant b \leqslant 50°$. We use this large range of b to account for most of the zodiacal cloud emission (see, e.g., Grogan et al., 2001, their Fig. 1).

We found that Karin and Veritas particles contribute 3.7%, 4.3%, and 5.4% to the total zodiacal cloud brightness at 12, 25, and 60 μm, respectively. The relative contribution of Karin and Veritas particles to these fractions is sensitive to the values of α_K and α_V for $D \leqslant D_{break}$, and to the value of D_{break} itself; we find it scales roughly with S_K/S_V. The combined contribution of Karin and Veritas particles to the zodiacal cloud brightness is 3.1–4.3%, 3.8–4.7%, and 4.7–6.2% at 12, 25, and 60 μm for all variations of our two slope model. Models with constant slope described in Section 4.1.1 predict similar values. Taken together, these results suggest that Karin and Veritas particles contribute only ≈ 5% to the zodiacal cloud brightness.
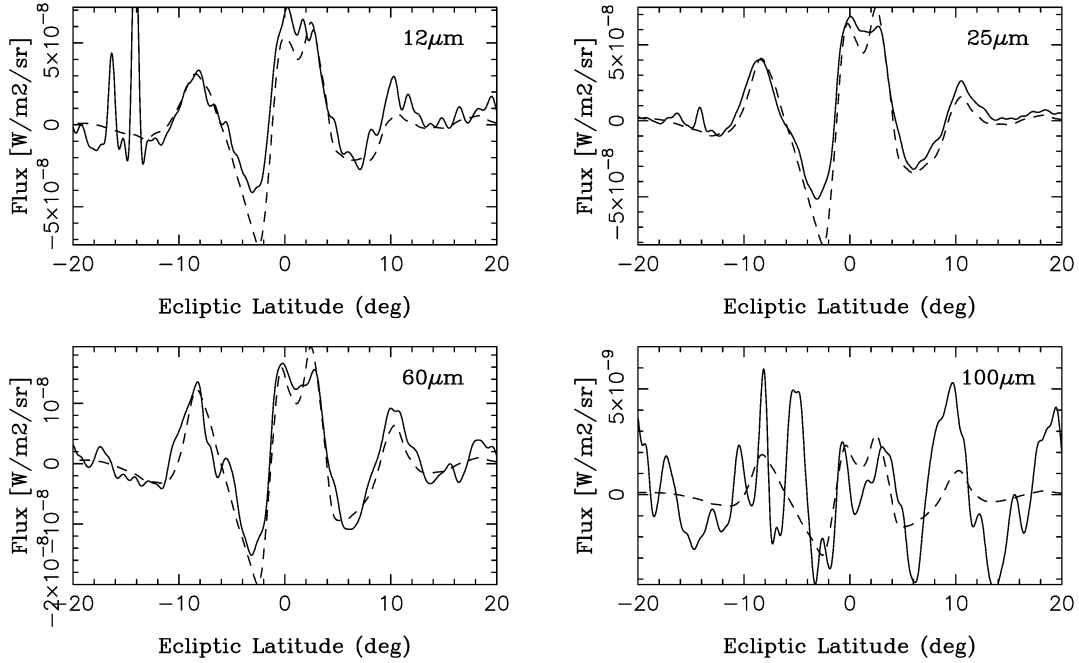
Fig. 16. Illustration of Model I that uses a power-law with $\alpha = 2.2$ for $D \leqslant 100$ μm and $\alpha = 3.5$ for $D > 100$ μm. We used $f_K = 20$ and $f_V = 1$ here. The panels show a representative IRAS scan (180_24; Table 3) in 12-, 25-, 60-, and 100-μm wavelengths. The residual IRAS (solid lines) and model (dashed lines) profiles were extracted from the total signals by the Fourier filter with $f_1^{-1} = 15°$ and $f_2^{-1} = 1°$.
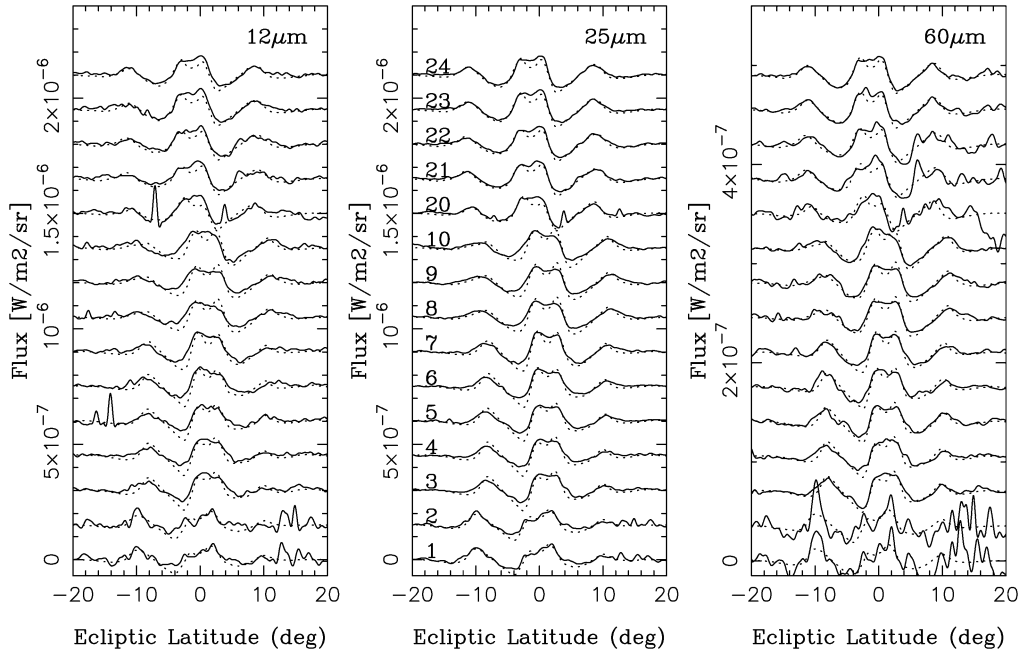

Fig. 17. A comparison between the model (dotted lines) and observed data (solid lines) for trailing IRAS scans (i.e., scans corresponding to longitudes near the anti-apex of Earth motion; Table 2). We used $f_K = 20$, $f_V = 1$, optical properties of low-temperature cosmic pyroxene, $\alpha_K = \alpha_V = 2.2$ for $D \leqslant 100$ μm and $\alpha_K = \alpha_V = 3.5$ for $D > 100$ μm, $N_K = 2.0 \times 10^{23}$ μm^{-1} and $N_V = 2.9 \times 10^{23}$ μm^{-1}. All scans shown here have $l_{SE} > 85°$. The scans are labeled by their identification labels listed in the middle panel. These labels are listed in Table 2.

This value is significantly smaller than predicted by Dermott et al. (2001), who suggested the major asteroid dust bands contribute as much as ≈30% to the total thermal emission of the zodiacal cloud.

The difference between our estimates and those by Dermott et al. may stem from different definitions of the latitudinal range where fluxes are compared. Dermott et al. (2001) expressed their estimate in terms of the peak intensity at $b \approx 0°$, essentially arguing that the dust bands contribute ≈30% of the zodiacal cloud emission between $-10° \lesssim b \lesssim 10°$. Conversely, we calculated the contribution by integrating the flux for $-50° \leqslant b \leqslant 50°$. Because the inner and outer dust bands do
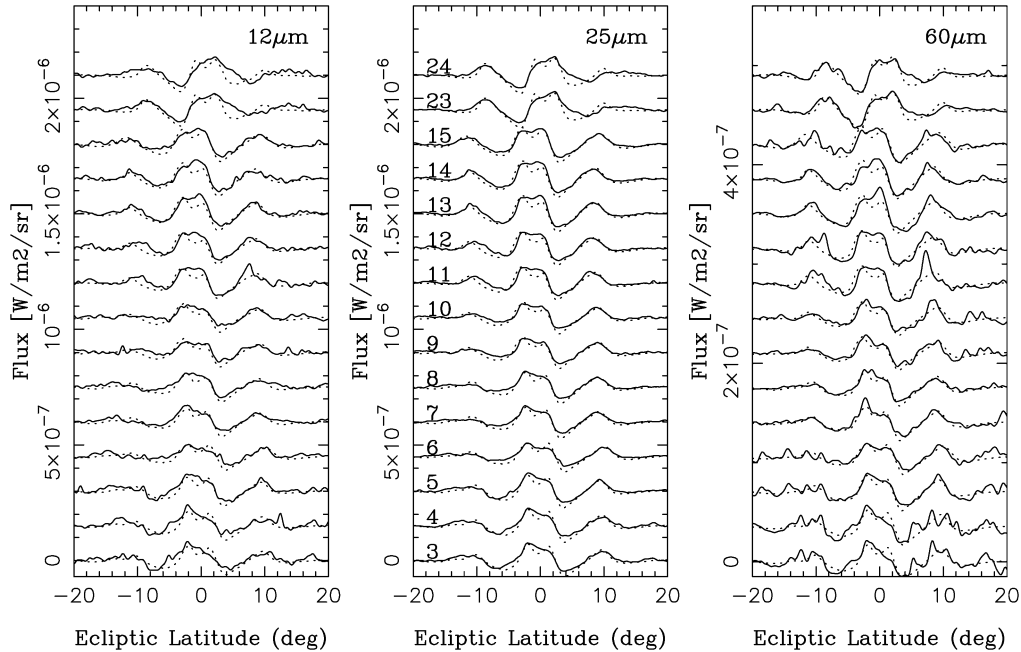
Fig. 18. The same as Fig. 17 but for the leading scans (i.e., scans corresponding to longitudes near the apex of Earth motion; Table 3). We have excluded scans with $l_{SE} < 85°$, and also those scans in Table 3 that were contaminated by the Galactic plane IR emission. These scans are noisy and do not appear clearly in the plots.

not significantly contribute to the zodiacal cloud for $|b| \gtrsim 20°$, their contribution at $-50° \leqslant b \leqslant 50°$ is smaller than their contribution at $-10° \lesssim b \lesssim 10°$.

To test this possibility, we calculated $\int F_{model} / \int F_{obs}$ for $|b| \leqslant 10°$. We found that Karin and Veritas particles contribute by $\approx 10\%$ to the total zodiacal cloud brightness in this latitudinal range, a factor of ≈ 3 less than the estimate of Dermott et al. (2001). This difference may be explained by the different assumptions made by Dermott et al. in their model. For example, to estimate the contribution described above, Dermott et al. (2001) had to extrapolate to $a < 2$ AU where they had a paucity of dynamical information on particle orbital motion from direct numerical integration (Grogan et al., 2001, their Section 5). They assumed that the thermal radiation of most $a < 2$ AU material contributed to the background.

Our results showed that small particles can evolve over 2 AU without large inclination changes (Figs. 1 and 2; see also Grogan et al., 2001). These particles are important to our best-fit models because they contribute to high-frequency spatial features in the IRAS scans. When these particle populations with $a < 2$ AU are properly accounted for, the contribution of Karin and Veritas particles to the total zodiacal cloud brightness is smaller than estimated by Dermott et al. (2001). We will show in Sections 4.1.3 and 4.2 that small particles produced by disruptive collisions are particularly important to explain the IR fluxes in the IRAS scans with $l_{SE} < 90°$.

All of the results discussed above were obtained using the optical properties of low-temperature cosmic pyroxene. The results for iron-free olivine and pyroxene were similar because the emission efficiency of these two materials at 12, 25, and 60 μm are similar in ϵ at these wavelengths to low-temperature cosmic pyroxene (Fig. 4). Overall, the low-temperature cosmic

pyroxene showed a bit better balance between the strength of signals at 12, 25, and 60 μm than iron-free olivine and pyroxene. The difference is not significant enough, however, to decisively favor low-temperature cosmic pyroxene over the other two other silicate materials.

Carbon grains with low carbonization degrees failed to match the observed profiles for all parameter choices described in this section except when we used $D_{break} > 400$ μm for both Karin and Veritas particles. With $D_{break} \lesssim 400$ μm, these models produced signals that were too weak at 60 μm because small 'carbon400' particles radiate extremely inefficiently at long wavelengths (Fig. 4). Models with $D_{break} > 400$ μm for Karin particles do not provide particularly satisfying fits because of the problems discussed above. Given these results, we find that 'carbon400' cannot be used to mimic the emission properties of Karin or Veritas particles. Carbon grains with high carbonization levels (our 'carbon1000') match the IRAS profiles only slightly worse than silicate materials. We will discuss this difference in greater detail in Section 4.2.2.

4.1.3. IRAS scans with $l_{SE} < 90°$

A major problem with all our models described above is that while reasonable fits were obtained for solar elongations $l_{SE} \gtrsim 90°$ (Figs. 17 and 18), these models failed to match the IRAS profiles obtained for $l_{SE} < 90°$. Fig. 19 shows a comparison between the model and IRAS observations with $l_{SE} \approx 65°$ (IRAS scan 441_21; Table 2). We have selected this and similar scans with small l_{SE} to probe the thermal emission of particles at ≈ 1 AU. By scanning at solar elongations $\approx 65°$, the telescope can see particles as close as ≈ 0.9 AU to the Sun.

The IRAS profiles with small l_{SE} do not show the double-peaked band-pair signature that is characteristic for emission of particles from $a > 2$ AU. Instead, they show a single broad
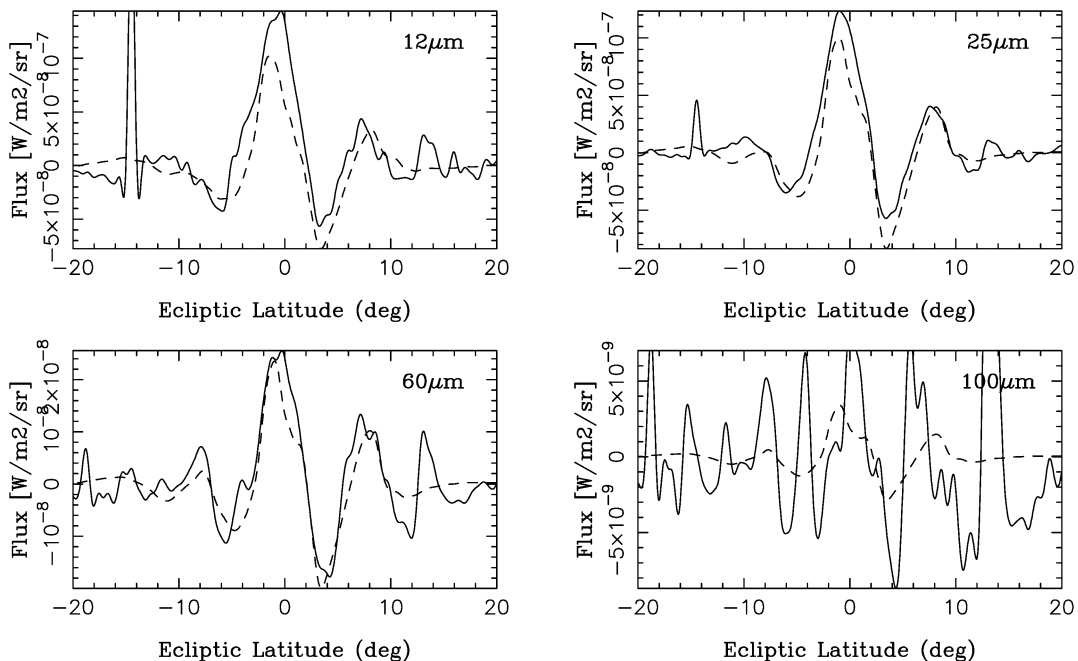
Fig. 19. An example of a case where our Model I fails to match IRAS observations for small l_{SE}. The IRAS scan 441_21 has one of the smallest solar elongation ($l_{SE} = 64.8°$) among all of our selected scans. We used $f_K = 20$, $f_V = 1$, and the broken-slope power-law SFD with $\alpha_K = \alpha_V = 2.2$ for $D \leqslant 100$ μm and $\alpha_K = \alpha_V = 3.5$ for $D > 100$ μm. The plot shows the residual model (dashed lines) and observed (solid lines) profiles after the background has been removed from both signals by the Fourier filter (Appendix C). Instead of attempting for the best fit we used N_K and N_V determined for our best fits to IRAS scans with $l_{SE} \gtrsim 90°$. The plot shows the residual model (dashed lines) and observed (solid lines) profiles after the background has been removed from both signals by the Fourier filter (Appendix C). There exists an important mismatch between the model and observed fluxes especially for short wavelengths.

peak at $b \approx 0°$ (Fig. 19). This signal must be coming from small particles at $a < 2$ AU because big particles are too dispersed in this region to contribute significantly to the small-scale features (compare top and bottom panels in Figs. 1 or 2). Conversely, small particles tend to keep their low i and e even for small a. Apparently, we need a larger contribution of small particles with $a < 2$ AU than suggested by all our previous models. These particles may be second- and higher-generation products of the collisional cascade started back in the main belt (Section 4.2).

Direct evidence for large populations of small particles with $a < 2$ AU comes from Fig. 19. To show this evidence clearly, we did not adjust N_K and N_V in these figures to obtain a best fit. Instead we used $N_K = 2.0 \times 10^{23}$ μm^{-1} and $N_V = 2.9 \times 10^{23}$ μm^{-1} in Fig. 19. These values were determined by our previous modeling as the best-fit N_K and N_V values to IRAS scans with $l_{SE} \gtrsim 90°$. If these models are correctly describing the orbital and size-frequency distributions of particles in the dust bands, they should also produce satisfactory fits to the IRAS scan 441_21 ($l_{SE} = 64.8°$; Fig. 19) and similar scans with small l_{SE}.

All our models that we have discussed to this point show fluxes that are deficient for small l_{SE}. In Fig. 19, the model signal for $b \approx 0°$ is about 30 and 20% weaker than the observed one in 12- and 25-μm wavelengths, respectively. Thus, to fit the profiles with small l_{SE}, one needs to increase the cross-sectional surface area by either increasing the number of particles and/or by decreasing the typical size of particles that contribute to the thermal emission. None of these options produce good fits to

IRAS scans with both the small l_{SE} and $l_{SE} \gtrsim 90°$ unless we assume that the SFD of radiating particles is a function of heliocentric distance. We will further analyze this scenario below.

4.2. Model II

Previously, we did not explicitly account for collisions in our N-body integrations (Section 2.2) because it was computationally expensive to deal with numerous second- and higher-generation products of the collisional cascade. For this reason, we are currently unable to construct a model where the thermal emission of particles produced by the collisional cascade is treated rigorously. Instead, we used approximate means to include the effect of collisions in our models.

These models use particle populations whose SFDs vary with semimajor axis. To start, we divided the semimajor axis interval $0.5 \leqslant a \leqslant 3.5$ AU into 12 zones, each having a width of 0.25 AU. We then used SIRT to calculate thermal radiation of particles in each zone and determined their corresponding fluxes in the IRAS filters (see Mahoney-Hopping et al., 2003, 2004, for a similar approach). Figs. 20 and 21 show these fluxes for two representative IRAS scans.

These figures show that Karin particles with $a > 2$ AU produce a characteristic band-pair signature with two peaks. The dip between the peaks becomes shallower as a approaches 2 AU because the particles are gradually spread in i during their orbital decay. At $a \lesssim 2$ AU, where particles' orbits are affected by secular resonances, the profiles become more complicated and shift to northern (Fig. 20) or southern (Fig. 21) latitudes due to the projection effects produced by the decreasing distance to
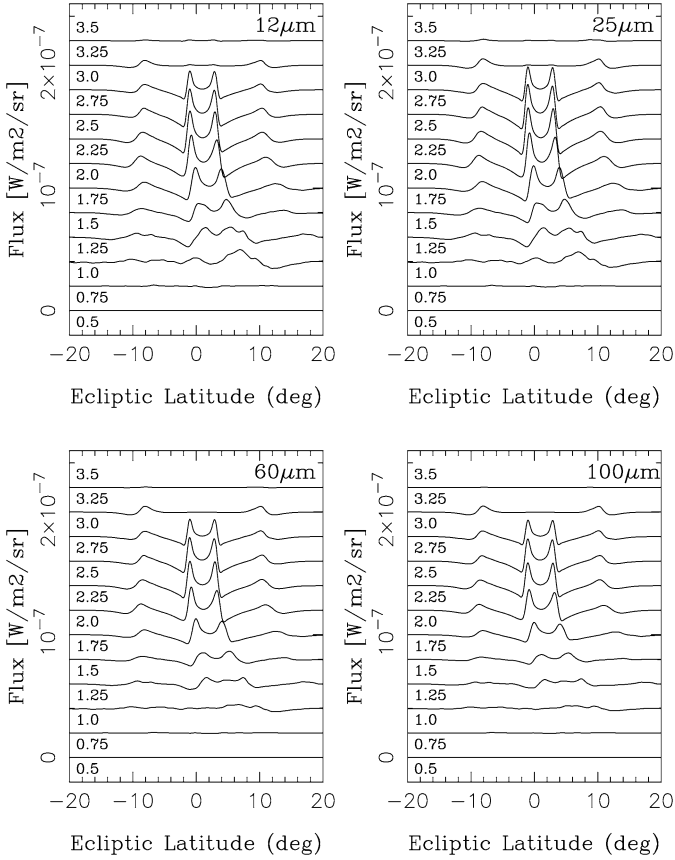
Fig. 20. Illustration of the IRAS fluxes produced by Karin and Veritas particles in orbits with different a. We used $f_K = 20$, $f_V = 1$, $\alpha_K = \alpha_V = 2.2$ for $D \leqslant 100$ μm and $\alpha_K = \alpha_V = 3.5$ for $D > 100$ μm. These values correspond to our best-fit Model I. The profiles show the thermal flux in IRAS filters received from particles in twelve different zones in a. When the profiles are added together they produce the result shown in Fig. 16. The pointing geometry is defined by that of the IRAS scan 180_24. The profiles were shifted for clarity and the fluxes in 60 and 100 μm were multiplied by factors of 3 and 20, respectively, to clearly appear in the scale of the plot.

Fig. 21. The same as Fig. 20 but for IRAS scan 441_21.

the observer. Thermal radiation of particles with $a \lesssim 2$ AU significantly contribute to the IRAS fluxes. Similar effects can be seen in Figs. 20 and 21 for Veritas particles.

In general, each zone in a is likely to have its own SFD, which may or may not be different from SFDs in other zones. We will denote these distributions by $N^{(j)}(D)$ where $j = 1, \ldots, 12$. Using the power-law parameterization of $N^{(j)}(D)$, there are four free parameters in each zone that we need to fix: $\alpha_<^{(j)}$, $\alpha_>^{(j)}$, $D_{\text{break}}^{(j)}$, and $D_{\text{max}}^{(j)}$, where $\alpha_<^{(j)}$ and $\alpha_>^{(j)}$ are the power-law indexes for particles smaller and larger than $D_{\text{break}}^{(j)}$, respectively (we assumed that $D_{\text{min}} = 1$ μm). Thus, there are 48 free parameters for each source. It is clearly difficult to uniquely determine all of the free parameters in this model.

To deal with this problem, we used two different schemes. In our first model we assumed that $N^{(j)}(D) = N(D)$ for all j and weighted the contribution of these populations at different a to the total cross-sectional surface area using empirical weighting factors (Section 4.2.1). Our second model used a Monte Carlo scheme to deal with disruptions among drifting particles and their fragments. We used this model to determine $N^{(j)}(D)$
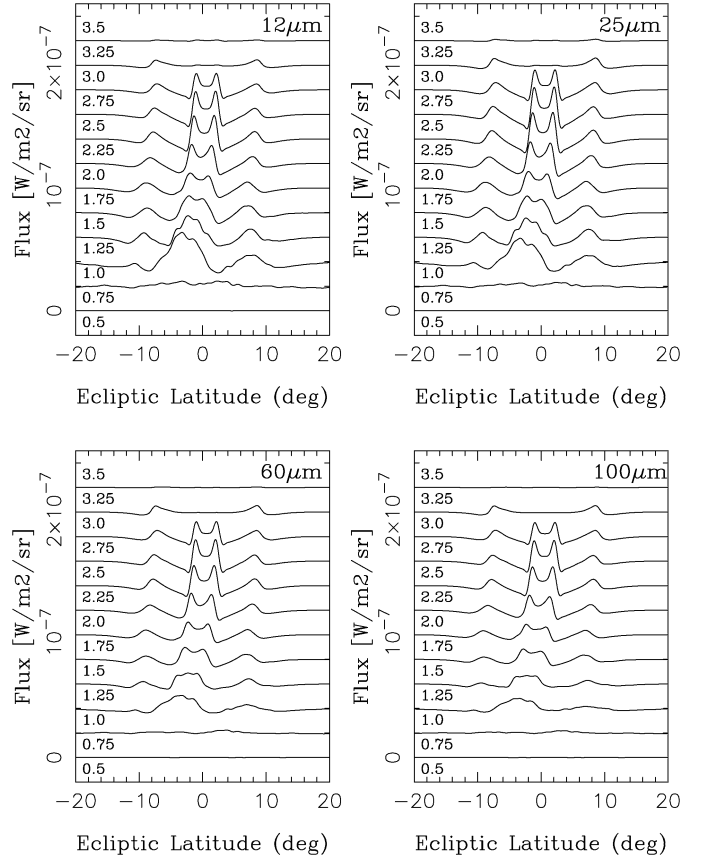
in each semimajor axis zone based on assumed $\tau_{\text{col}}(D)$ and $P(D, t)$. These $N^{(j)}(D)$ were then calibrated by fits to IRAS observations. We will describe our Monte Carlo model in Section 4.2.2.

4.2.1. Model with weighting factors

With $\tau_{\text{col}} > \tau_{\text{dyn}}$ and $P(D, t)$ constant with t, the cross-sectional surface area of particles between a and $a + \delta a$ is $\propto a$ because of the effects of P–R drag. This surface area distribution in a was a major assumption of our Section 4.1 models. Here we relax this assumption and construct models where the cross-section of Karin and Veritas particles varies with a as a^β, where β is a free parameter.

To produce distributions $\propto a^\beta$, we used weighting factors $w_j = a_j^{\beta-1}$, $j = 1, \ldots, 12$, where $a_j = 0.675 + 0.25(j-1)$ AU are centers of our semimajor axis zones. We first selected $\alpha_<^{(j)}$, $\alpha_>^{(j)}$, $D_{\text{break}}^{(j)}$, and $D_{\text{max}}^{(j)}$ and calculated the SIRT profiles for these model parameters for all D and j. These profiles were multiplied by weighting factors w_j and were added together. Finally, calibration factors N_K and N_V were adjusted to obtain good matches to the observed fluxes. Because of the difficulty in dealing with a large number of free parameters, we assumed that $\alpha_<^{(j)}$, $\alpha_>^{(j)}$, $D_{\text{break}}^{(j)}$, and $D_{\text{max}}^{(j)}$ are the same for all j.

We found that the best fits between model and data were produced when $\alpha_<^{(j)} \approx 1.5$–$2.5$, $\alpha_>^{(j)} \gtrsim 3.5$, $D_{\text{break}}^{(j)} \sim 50$–$400$ μm, and $D_{\text{max}}^{(j)} = 1$ cm. These values are similar to those determined in Section 4.1 but also allow for slightly larger $D_{\text{break}}^{(j)}$. We found
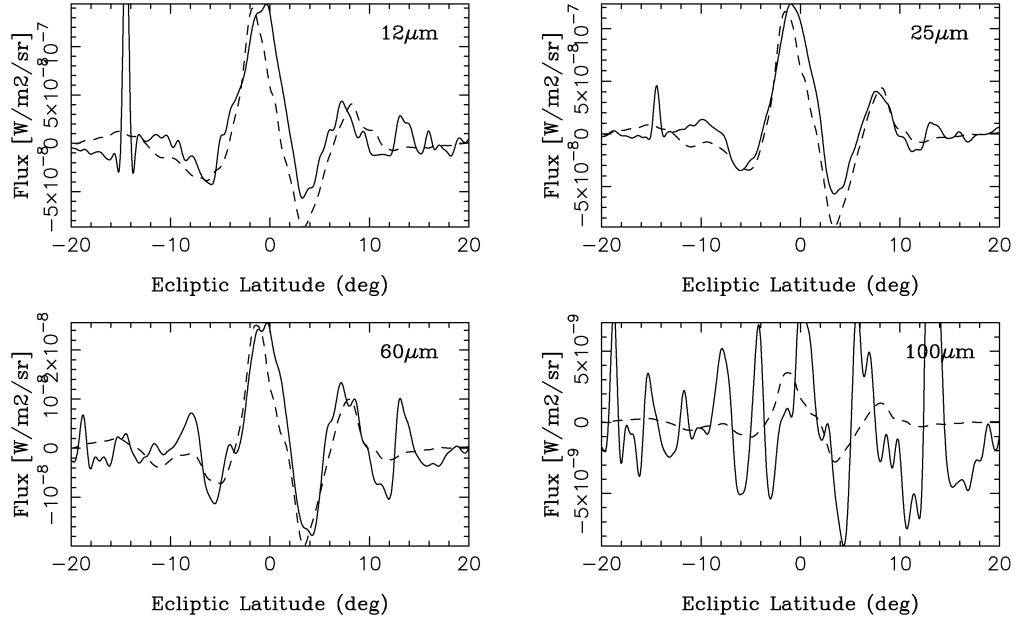
Fig. 22. Illustration of a model where we weighted the sliced profiles in Fig. 21 (IRAS scan 441_21) by a^{-1}. This weighting sets the cross-sectional surface areas in all semimajor axis zone to be roughly the same (i.e., $\beta = 0$). With this adjustment, the model matches the observed profile much better than in Fig. 19 where the cross-sectional surface area between a and $a + \delta a$ was roughly $\propto a$ due to effects of P–R drag. We used $f_K = 20$, $f_V = 1$, $\alpha_K = \alpha_V = 2.2$ for $D \leqslant 100$ μm and $\alpha_K = \alpha_V = 3.5$ for $D > 100$ μm.

that $\beta \approx 0$ yielded acceptable fits for all IRAS scans, including those with small solar elongations. Values of β in excess of ≈ 0.5 produced discrepancies similar to (or larger than) the ones shown in Fig. 19. With $\beta \lesssim -0.5$, the model fluxes were too strong for small l_{SE} relative those obtained with $l_{SE} \gtrsim 90°$.

Fig. 22 (441_21; $l_{SE} = 64.8°$) shows fits with $\beta = 0$ that can be compared to Fig. 19, where $\beta = 1$. We used $f_K = 20$, $f_V = 1$, $\alpha_K = \alpha_V = 2.2$ for $D \leqslant 100$ μm and $\alpha_K = \alpha_V = 3.5$ for $D > 100$ μm. With these parameters, $N_K = 2.5 \times 10^{23}$ μm^{-1} and $N_V = 3.5 \times 10^{23}$ μm^{-1}. The total cross-sectional surface areas, their ratio and other parameters characterizing the particle populations are listed in Table 5 (Model 8). They are similar to the values of these parameters determined previously. The χ^2 value is a bit larger in this case because we include scans with small l_{SE} that are more difficult to fit.

With $\beta = 0$, the number of particles between a and $a + \delta a$ is roughly constant with a. To achieve this distribution, new particles must be created in the source with time-dependent $P(D, t)$ and/or new particles must be produced at $1 \lesssim a \lesssim 3$ AU by collisional disruptions. It is clear that these disruptions will eliminate large particles and produce numerous small particle fragments. As a consequence, the SFD of particles will change with semimajor axis. Unfortunately, we were unable to determine this changing SFD with a directly by fits to IRAS data because the number of free parameters was too large. We deal with this problem in the following section.

4.2.2. Monte Carlo model for collisions

Our Monte Carlo model follows individual particles that are produced in the source and drift toward smaller a by P–R drag. The production rate of these source (first-generation) particles is defined by $P(D, t)$, where D is diameter and t is the time

elapsed since the formation of the source family. We assumed that $P(D, t) = P_0 D^{-\gamma} \exp(-t/\tau_P)$, where P_0, γ, and τ_P are free parameters. We used values of P_0 that were large enough to obtain good statistics and varied γ over $2 \leqslant \gamma \leqslant 3.5$, where values in the upper end of this interval correspond to a Dohnanyi-type distribution (Dohnanyi, 1969). τ_P defines the decay in the source production rate over time. We used $\tau_P = 0.5$, 1, 2, 5 Myr and ∞.

The model allows particles to collisionally disrupt and produce second- and higher-generation debris particles. The rate of particle disruptions is defined by the collisional lifetime, $\tau_{col}(D, R)$, that we set to be a function of diameter D and heliocentric distance R. We used several approximations of $\tau_{col}(D, R)$ such as the interplanetary τ_{col} determined by Grün et al. (1985, their Fig. 6) and simple forms where $\tau_{col} \propto \sqrt{D}$ (e.g., Farley et al., 1998; Dermott et al., 2001). When a particle disrupts the code replaces it with a swarm of fragments that have a power-law distribution. We assumed that the mass of the largest fragment is one half of that of the parent particle. Mass conservation then fixes the power-law index of the fragments (e.g., Greenberg and Nolan, 1989). To keep things simple we assumed that the ejection speeds of fragments produced by these secondary breakups were small compared to those of the first-generation fragments that were violently launched into space by the family-forming collision.

We have run a number of experiments with our Monte Carlo model with different values of model parameters τ_{col}, τ_P, and γ. In each run, we determined: (i) the SFD at the present epoch as a function of the semimajor axis; (ii) the terrestrial accretion rate at the present epoch. Results from (ii) can be compared with measurements of the terrestrial accretion rate (Love and Brownlee, 1993; Taylor et al., 1996). We discuss them in Section 5.
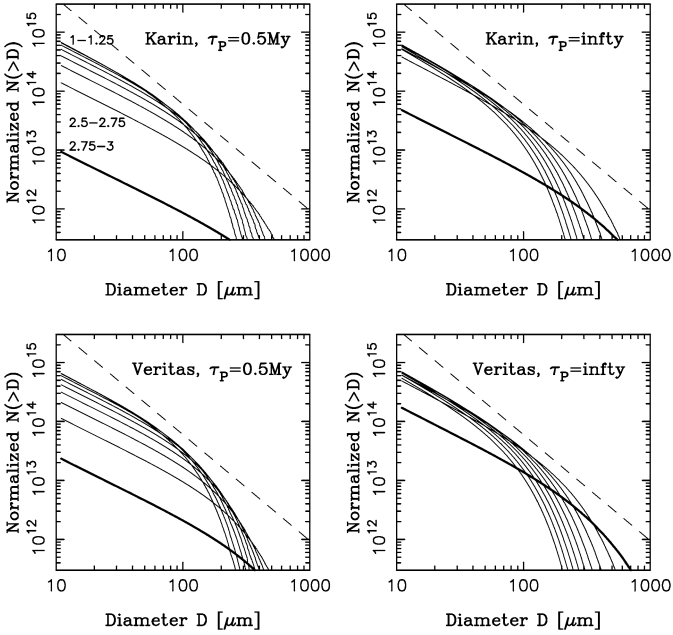
Fig. 23. The cumulative size-frequency distribution of Karin (top) and Veritas (bottom) particles in different semimajor axis zones. The distributions in the source zone are denoted in bold. Labels in top-left panel denote the semimajor axis range (in AU) corresponding to different lines. The distributions were normalized so that the cross-sectional surface area of particles in the zone between 2 and 2.25 AU is equal to 1 km^2. We used $\tau_P = 0.5$ Myr in the left panels and $\tau_P = \infty$ in the right panels. The dashed line shows the reference slope with $\alpha = 2.8$, which corresponds to our best-fit models with constant α in the whole size range (Fig. 15). The SFD of particles steepens at small a because large particles break before they can drift to small a by P–R drag and generate small particles which drift faster and reach small a before being disrupted.

Fig. 24. (a, c) Differential SFD exponent for Karin and Veritas particles with $D = 10$–50 μm in various semimajor axis zones. (b, d) The distribution of normalized cross-sectional surface area as function of a. Panels (a) and (b) show results with $\tau_P = 0.5$ Myr. Panels (c) and (d) show results with $\tau_P = \infty$. We used τ_{col}^{Gi} and $\gamma = 3.0$ here. The cross-sectional surface area was normalized to 1 in the semimajor axis zone between 2 and 2.25 AU. The cross-sectional surface areas in the source zones (2.75–3 AU for Karin particles and 3–3.25 AU for Veritas particles) are smaller than those in the neighbor zones because particles do not populate orbits with $a > a_{source}$ where $a_{source} \approx 2.866$ AU for the Karin cluster and $a_{source} \approx 3.17$ AU for the Veritas family. The SFD exponent in the source zones is ≈ 2 (i.e., $\approx \gamma - 1$) because small particles are removed by the P–R drag.

We used (i) in SIRT to test whether the SFDs generated by the Monte Carlo code with a particular choice of parameters can be used to obtain a good match to the IRAS data. In the first step, we binned the distributions of particles in 12 semimajor axis zones with 0.5 AU widths and centers at $a_j = 0.675 + 0.25(j - 1)$ AU, $j = 1, \ldots, 12$. These are the same bins used in Section 4.2.1. Fig. 23 shows the SFDs for Karin and Veritas particles in the individual zones obtained with Grün et al.'s (1985) interplanetary τ_{col} and $\gamma = 3$. To illustrate the dependence of these SFDs on τ_P, we used $\tau_P = 0.5$ Myr in the left panels and $\tau_P = \infty$ in the right panels.

Two effects of collisions are apparent in Fig. 23: (1) Large particles are disrupted before they can drift to small a; this produces SFDs that bend at $D \approx 100$–200 μm because they are deficient in large particles. (2) The SFDs of particles become steeper with decreasing a because numerous small particles are produced by the collisional cascade and because few large particles survive long enough to reach those a values. The SFDs produced with $\tau_P = 0.5$ Myr and $\tau_P = \infty$ do not differ very much. With $\tau_P = \infty$, the slopes of SFDs in small semimajor axis bins tend to be slightly steeper than those for $\tau_P = 0.5$ Myr.

Figs. 24a and 24c show effect (2) for Karin and Veritas particles with 10 μm $\leqslant D \leqslant 50$ μm. The size exponents in this size range are comparable for both particle populations. The SFDs are shallow at large a and become steeper at small a. For
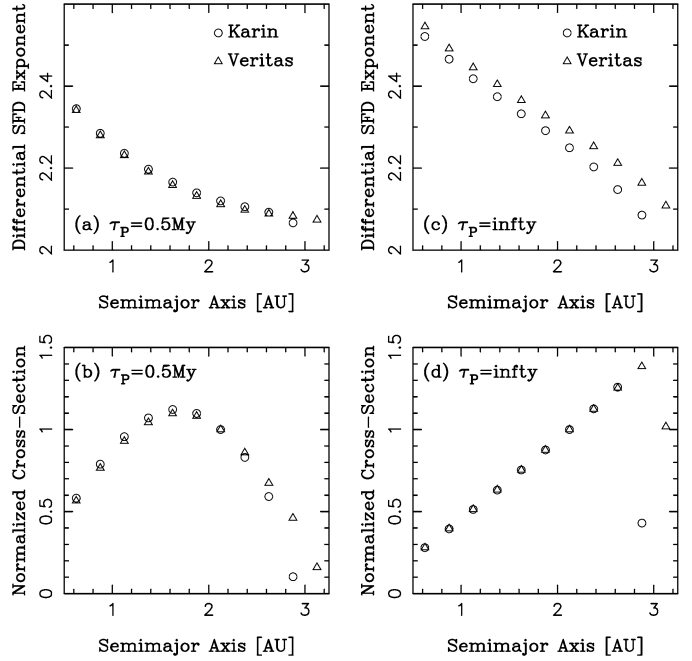
$a \approx 1$ AU, $\alpha_K = \alpha_V \approx 2.2$–$2.5$. The values of α found here for $1 \lesssim a \lesssim 3$ AU and $D = 10$–50 μm are intermediate between the values we determined previously from our fits to the IRAS data. These fits used $\alpha_K = \alpha_V \approx 2.8$ in models where both power indices were assumed fixed for 1 μm $\leqslant D \leqslant 1$ cm (Section 4.1.1), and $\alpha_K = \alpha_V \approx 2.1$–$2.4$ for $D \lesssim D_{break}$ in models where α_K and α_V changed at D_{break} (Section 4.1.2). The values of D_{break} found here (Fig. 23) are also comparable to those determined in Section 4.1.2.

With $\tau_P = 0.5$ Myr, the cross-sectional area of particles in individual semimajor axis zones show an interesting behavior (Fig. 24b) that is more complicated than the simple power-law dependence assumed in Section 4.2.1. It increases as we go from $a = 3$ AU to $a = 2$ AU and peaks at $a \approx 1.6$ AU. We believe this happens because large particles disrupt between 2 and 3 AU and produce smaller fragments which effectively represent a larger total cross-section. This behavior contrasts with the situation where the total cross-section of particles in a semimajor axis zone is $\propto a$ (e.g., our previous models that ignore effects of collisions and propagate particles from sources to sinks by P–R drag only). Interestingly, Fig. 24d shows that the cross-section is $\propto a$ if the decay constant τ_P is large. The transition from cases like Fig. 24b to cases like Fig. 24d happens for $\tau_P \approx 1$ Myr.
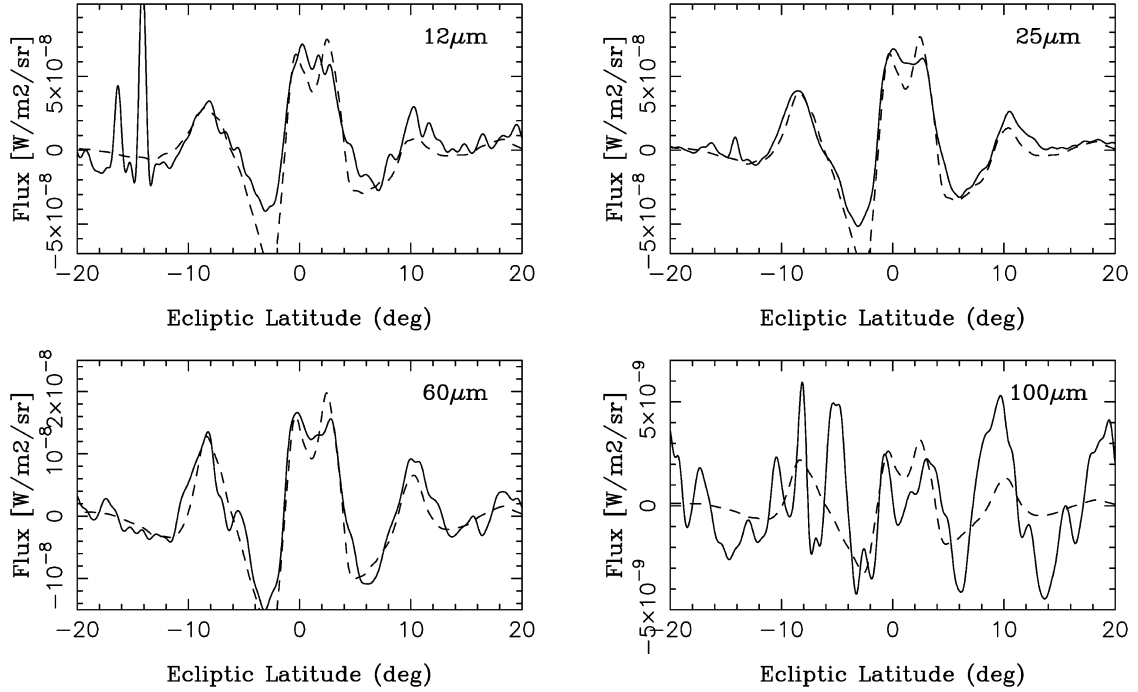
Fig. 25. Illustration of a model that uses $f_K = 20$, $f_V = 1$, $\tau_P = \infty$, τ_{col}^{Gi}, $\gamma = 3.0$, and the optical properties of low-temperature cosmic pyroxene. The panels show a representative IRAS scan (180_24; Table 3) in 12-, 25-, 60-, and 100-μm wavelengths. The plot shows the residual IRAS (solid lines) and model (dashed lines) profiles after background has been removed from both signals by Fourier filter with $f_1^{-1} = 15°$ and $f_2^{-1} = 1°$. The model fits are satisfactory.
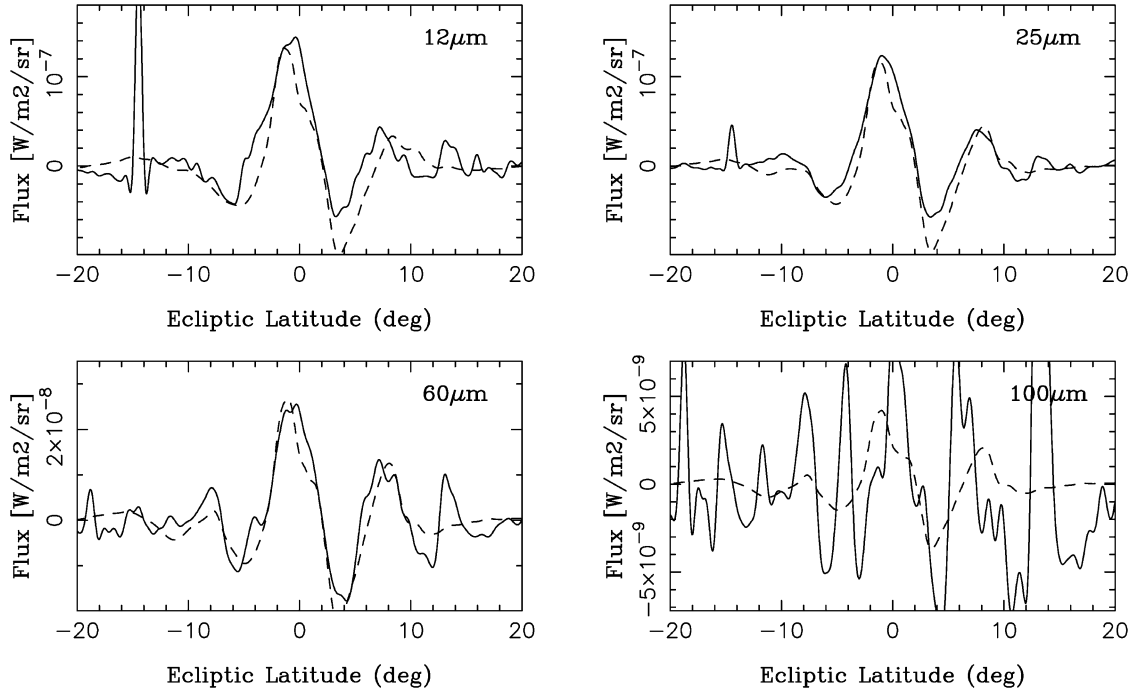

Fig. 26. The same as Fig. 25 but for IRAS scan 441_21. This is the scan with largest χ^2 among all selected scans except of 032_02 and 032_11 that have 60-μm wavelengths polluted by the Galactic emission.

We used distributions like those shown in Fig. 23 in SIRT to test whether the thermal flux from the model particle population matches IRAS observations. Figs. 25 and 26 show our best-fit results for our two representative IRAS scans. Figs. 27 and 28 show these results for IRAS scans in Tables 2 and 3, respectively. To obtain these fits, we used $f_K = 20$, $f_V = 1$,

$\gamma = 3$, and $\tau_P = \infty$. For the collisional lifetime of particles we used $\tau_{col}^{Gi}(D, R)$ determined by Grün et al. (1985) from the analysis of spaceborne micrometeoroid detectors (Grün et al.'s interplanetary collisional lifetime). This collisional lifetime has the following dependance on R and D: $\tau_{col}^{Gi}(D, R) \propto R^{1.8}$. For $R = 2.5$ AU, $\tau_{col}^{Gi}(D)$ has a minimum for $D \approx 2$ mm, where
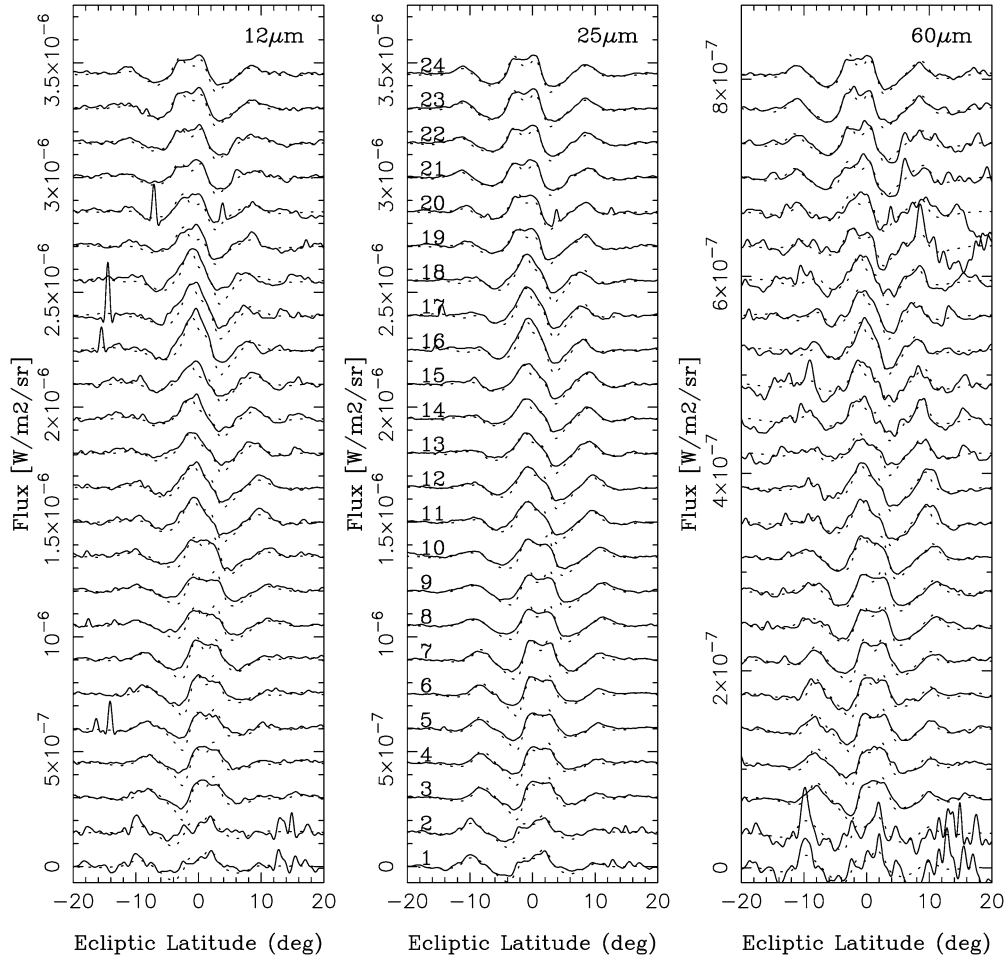
Fig. 27. A comparison between the model (dotted lines) and observed data (solid lines) for trailing IRAS scans. We used the same model parameters as the ones in Fig. 25. The scans are labeled by their identification labels listed in Table 2.

$\tau_{\rm col}^{\rm Gi} \approx 50,000$ yr, and increases for both smaller and larger D. For $D = 100$ μm, $\tau_{\rm col}^{\rm Gi} \approx 1$ Myr. For $R = 1$ AU, the minimum of $\tau_{\rm col}^{\rm Gi}(D)$ for $D \approx 2$ mm is $\approx 10,000$ yr.

The fits in Figs. 25 and 26 yield comparable χ^2 values to those obtained previously (Sections 4.1 and 4.2.1). Obtaining reasonable fits in Figs. 25 and 26, however, is more satisfying because these fits use a realistic collisional model. The distribution of particles in a and D obtained with this model (Figs. 23 and 24) is more likely to be realistic than those obtained with empirical fits (Sections 4.1 and 4.2.1). For example, it turns out that the cross-sectional surface does not need to be roughly constant with a as implied by the models with empirical weighting factors. Instead, good fits to IRAS data can be obtained with models where the cross-sectional area is $\propto a$ (as if in the absence of collisions) and where the SFD slope becomes steeper with decreasing a (due to generation of collisional debris at small a; Figs. 24c and 24d). With $\tau_{\rm col}^{\rm Gi}$, we found that these latter models occur for $\tau_{\rm P} \gtrsim 1$ Myr.

Most model profiles in Figs. 27 and 28 show good matches to observations. A few show significant discrepancies. For example, the model profiles corresponding to scans 3–7 in Fig. 27 show deficient signal for $b \approx -4°$. Similarly, model profiles

corresponding to nos. 16–18 show a deficient signal for $b \approx 4°$. These discrepancies indicate we may be missing sources at latitudes intermediate between the inner and outer dust bands such as, for example, the E/F and G/H band pairs (Sykes, 1988). Cometary trails may also be contributing to the observed flux at latitudes where these discrepancies occur. For example, trail B identified by Sykes (1988) produces important emission for $b \approx -5°$ in trailing scans 3–7 (see Fig. 27). By using the third source, taken to be the Themis family, Grogan et al. (2001) were able to produce fits to some of the IRAS scans that look slightly better than the ones obtained here. This suggests that the third source may be needed to obtain better fits. The third, near-ecliptic source may be especially important in cases like leading scans 10–14, where the model fluxes are slightly deficient for $b \approx 0°$ (Fig. 28). We emphasize that our fits were obtained with the *minimal* model where we used two (asteroidal) sources only. It is likely that using more sources and/or additional empirical parameters would improve them.

Most models with $\tau_{\rm col} \neq \tau_{\rm col}^{\rm Gi}$ do not produce good fits to the IRAS data. For example, we used models with $\tau_{\rm col} = T_{\rm col}\sqrt{D/1\,{\rm m}}$, where $T_{\rm col} = 5$–20 Myr. These $\tau_{\rm col}$ were obtained by extrapolation from larger D (Farinella et al., 1998;
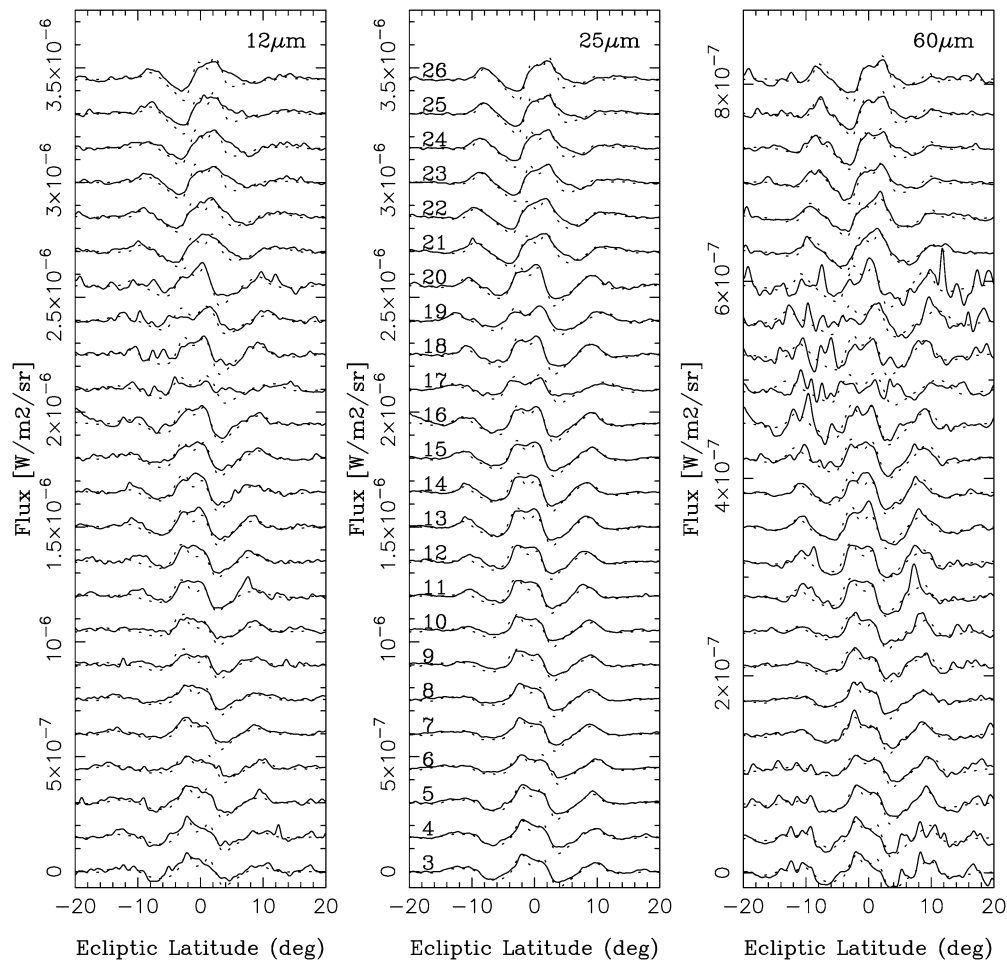
Fig. 28. The same as Fig. 17 but for the leading scans. We do not show scans B_032_02 and B_032_11 (nos. 1 and 2 in Table 3) because they are contaminated by the Galactic plane IR emission. These scans are noisy and do not appear clearly in the plots. Scan labels are listed in Table 3.

Bottke et al., 2005). With $T_{col} = 10$ Myr, the model profiles in the 60-μm IRAS filter were systematically about 30% weaker than the observed fluxes. Other values of T_{col} and test models with $\tau_{col} = $ const did not produce good fits to IRAS data as well. The likely problem with these disruption laws is that they are incompatible with the real SFD of particles. The wavy shape of the Grün et al. (1985) disruption law provides a better match.

We also used the collisional lifetime, τ_{col}^{Gl}, determined by Grün et al. (1985) from the analysis of lunar microcrater data (Grün et al.'s lunar collisional lifetime). This τ_{col}^{Gl} has the same dependance on R as τ_{col}^{Gi} and differs from τ_{col}^{Gi} for $D \lesssim 1$ mm, where $\tau_{col}^{Gl} \approx 100{,}000$ yr for particle sizes in the range of interest. The model fits with τ_{col}^{Gl} are slightly worse than those with τ_{col}^{Gi} (by about 0.3 in χ^2). Because Grün et al.'s lunar flux may be polluted by the craters formed by secondary ejecta particles, we will only discuss the results obtained with τ_{col}^{Gi} in the following.

We experimented with f_K and f_V. These experiments showed dependences of profile fluxes on these parameters that were similar to those determined previously using empirical parameterizations of the SFD. The dependences were discussed in Section 4.1. We found that $f_K \approx 20$ and $f_V \approx 1$–2 produce the best-fits (see Section 5 for a discussion of $f_K \approx 20$).

The dependence of our model fluxes on the optical properties of the radiating grains is similar to that discussed in Section 4.1.2. All silicate materials produce comparatively good fits. Carbon materials with low carbonization degrees do not match IRAS signals for longer wavelengths. Carbon materials with high carbonization degrees (i.e., 'carbon1000,' Jäger et al., 1998) work better but are not quite as good as silicate grains. From silicate grains, the low-temperature cosmic pyroxene works best, followed by iron-free olivine and pyroxene. The differences in χ^2 between silicate materials are very small.

We find that better fits are consistently obtained for large τ_P values. For example, χ^2 is about 0.7 smaller for our best-fit $\tau_P = \infty$ than that for $\tau_P = 0.5$ Myr. This result clearly favors slow decay of $P(D, t)$ over time with characteristic time scale of several Myr or longer.[9] The differences in χ^2 between mod-

---

[9] The value of τ_P may be constrained by the results of Farley et al. (2006). By measuring ^{3}He abundances in $\approx$8-Myr old deep-ocean sediments, Farley et al. detected Veritas particles that were accreted by the Earth. According to their results, Veritas particles with $D \approx 10$ μm produced a peak in the terrestrial impactor flux that lasted $\approx$1 Myr. Our model will need further development to determine a $P(D, t)$ function compatible with this constraint. Our preliminary results suggest that $\tau_P > 1$ Myr.

els with different values of γ are small. $\gamma \approx 3.0$ and Dohnanyi-like values of $\gamma \approx 3.5$ appear to work better than $\gamma < 3.0$ and $\gamma > 3.5$.

With $f_K = 20$, $f_V = 1$, τ_{col}^{Gi}, $\tau_P = \infty$, and $\gamma = 3.0$, and optical properties of low-temperature cosmic pyroxene, the best-fit model implies cross-sectional surface areas $S_K = 6.7 \times 10^9$ km^2 and $S_V = 1.4 \times 10^{10}$ km^2. These values are a factor of ≈ 2–4 lower than the cross-sectional areas determined in our empirical models (Models 1–8 in Table 5) due to the economic distribution of particles produced by τ_{col}^{Gi}. Most of S_K and S_V for $a \lesssim 2.5$ AU (Fig. 24) is in particles with $D < 500$ µm (Fig. 23). For the same reason, models with τ_{col}^{Gi} require significantly less material volume than models with one fixed SFD for all a that extends with a constant SFD slope to large D. We found that $D_K = 11$ km and $D_V = 14$ km in the best-fit model described above.

We found the ratio $S_K/S_V \approx 0.5$ for this model and also for most other models with plausible assumptions of τ_P and γ. Most of our good fits with τ_{col}^{Gi} correspond to S_K/S_V that vary between 0.45 and 0.57. These values are similar to the ratio of the cross-sectional areas listed for our empirical models in Table 5. The mass ratio, M_K/M_V, varies between 0.46 and 0.59 for all good fits with τ_{col}^{Gi}. These values are also comparable to values of M_K/M_V determined previously (Table 5).

Having determined our best-fit model parameters, we can estimate the contribution of Karin and Veritas particles to the total brightness of the zodiacal cloud emission. As we did in the previous section, we calculate these contributions as $\int F_{model}/\int F_{obs}$, where the integrals are evaluated over $-50° \leqslant b \leqslant 50°$. We also use a more limited range of latitudes, $-10° \leqslant b \leqslant 10°$, to determine the contribution of dust bands to the zodiacal cloud emission near the ecliptic.

Using $f_K = 20$, $f_V = 1$, τ_{col}^{Gi}, $\tau_P = \infty$, $\gamma = 3.0$, and optical properties of low-temperature cosmic pyroxene, we found that Karin and Veritas particles contribute on average by 6.2, 6.8, and 9.0% to the total zodiacal cloud brightness at 12, 25, and 60 µm, respectively, for $-50° \leqslant b \leqslant 50°$. The contribution of Karin and Veritas particles to these fractions are similar. The combined contribution of Karin and Veritas particles to the total zodiacal cloud brightness is 5.5–7.2, 5.7–7.4, and 8.6–9.3% at 12, 25, and 60 µm, with exact values depending on the chosen range of ecliptic longitude. Taken together, our models suggest that Karin and Veritas particles only contribute to the zodiacal cloud brightness by 5–9%. Fig. 29 illustrates this conclusion.

These estimates are comparable to those indicated by our models that neglected comminution (Section 4.1). We also found that the contribution Karin and Veritas particles to the total zodiacal cloud brightness at $-10° \leqslant b \leqslant 10°$ is 9–15%, i.e., about 2–3 times lower than the $\approx 30\%$ value suggested by Dermott et al. (2001). These estimates validate our previous result (see Section 4.1) that their contribution to the zodiacal cloud is smaller than thought before.

The above estimates should be used with caution because of an important limitation of our model. The small and large particles follow different orbital paths when they drift over the secular resonances at ≈ 2 AU (Figs. 1 and 2). Large particles disrupting at $a < 2$ AU produce small fragments that are or-
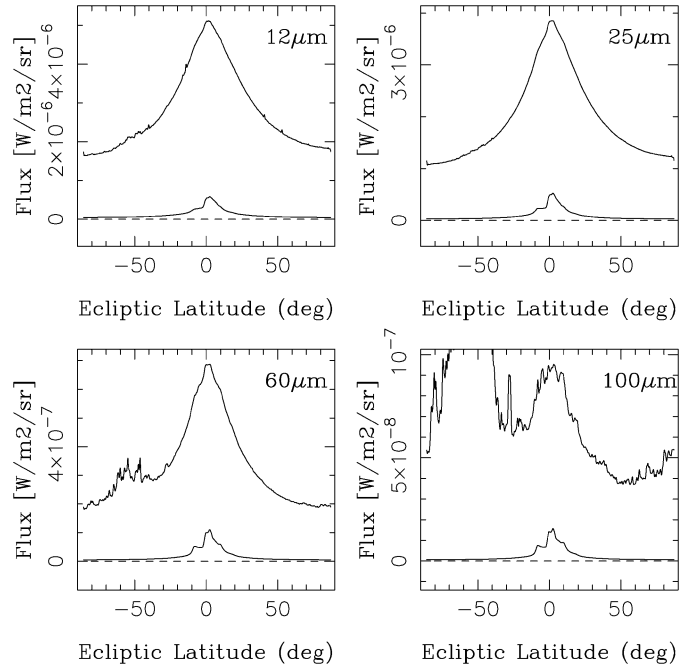

Fig. 29. Contribution of Karin and Veritas particles to the zodiacal cloud brightness. The panels show fluxes in 12-, 25-, 60-, and 100-µm IRAS wavelengths. The upper solid lines show IRAS scan 180_24 (Table 3) that has been smoothed by a low pass-filter to remove point sources and instrumental noise. The bottom solid lines show the contribution of Karin and Veritas particles to the observed fluxes. Karin and Veritas particles contribute to the observed fluxes by ≈ 9–15% within 10°, and by ≈ 5–9% within 50° to the ecliptic. The strong signal in 100-µm wavelengths between latitudes $b \approx -80°$ and $b \approx -30°$ is the Galactic plane emission.

bitally dispersed and produce signals in the IRAS latitudinal profiles that differ from those of similarly sized particles that we have tracked all the way from the source. Thus, by merging our N-body and Monte Carlo results, we do not rigorously account for the collisional production of small particles at $a < 2$ AU. A more advanced approach, capable of modeling the collisional cascade for all orbits, is beyond the scope of this paper. It will require computationally expensive N-body integrations of second- and higher-generation debris particles started on intermediate orbits between sources and sinks.

5. Discussion

In this paper, we described a new model for the zodiacal dust bands. This model includes several important improvements over the past work on the subject (e.g., Grogan et al., 2001). For example, our model accounts for thermal emission of diameter $D > 100$ µm particles, it includes dynamical effects on particles with $a < 2$ AU, and follows the collisional disruption of particles as well as the generation of new debris particles.

We used our model to obtain satisfactory fits for a larger range of IRAS scan geometries than Grogan et al. (2001), including those with small solar elongations which are generally more difficult to fit. We believe that Grogan et al.'s model would not produce satisfactory matches to IRAS scans with small solar elongations because these scans include important emission

from dust particles with $a < 2$ AU, which is not modeled in Grogan et al. Moreover, Grogan et al. (2001) assumed that the Eos family is the source of the outer dust band and used a large inclination dispersion of Eos particles in the source to obtain a satisfactory fit. If the inclination dispersion of Eos particles in the source were set to be comparable to the inclination dispersion of multi-kilometer Eos family members, the fits were unsatisfactory (e.g., Grogan et al., 1997, their Fig. 2). Conversely, our model was able to produce good fits to the IRAS scans by using Veritas particles whose inclination distribution in the source was set to be equal to that of large Veritas family members. For this and other reasons discussed in Section 1 (see also Nesvorný et al., 2003), we believe that the Veritas family is the real source of the outer dust band.

We found that particle populations with $a \lesssim 2.5$ AU are important contributors to the brightness of the zodiacal dust bands. These results appear to be supported by measurements of the parallactic distance. For example, Spiesman et al. (1995) used COBE data to determine the observed parallax of the inner and outer dust bands. They found the heliocentric distances of 1.37 ± 0.17 AU for the inner and 2.05 ± 0.13 AU for the outer band pairs. Using the same dataset, Reach et al. (1997) found distances of 1.7 ± 0.2 AU for the inner and 2.4 ± 0.3 AU for the outer band pair. Finally, using IRAS data, Reach (1992) found 1.35 ± 0.05 and 1.9 ± 0.2 AU for the inner and outer band pairs, respectively. These distance estimates are lower than those obtained previously (Gautier et al., 1984; Hauser et al., 1984).

To test this, we calculated the relative contribution to the total IR flux from particles at various a. We found that most of the thermal flux in the high-spatial-frequency signal reaching IRAS is produced by particles with $a < 2.5$ AU, with roughly equal parts being emitted by particles in 1–1.5-, 1.5–2-, and 2–2.5-AU zones. Moreover, Karin particles show a slightly larger flux from smaller a than the high-inclination Veritas particles; we believe this is probably due to projection effects. Taken together, we found our results can explain modern measurements of the parallactic distance described above. The exact contribution of particles in different semimajor axis zones depends on wavelength. For example, the contribution of particles with $a > 2$ AU is stronger in the 60-μm IRAS filter than at shorter wavelengths.

We can use our results to estimate the terrestrial accretion flux from Karin and Veritas particles. First of all, we used numerical simulations to determine the impact probability, $P_\oplus$, of Karin and Veritas particles on the Earth. As shown by Kortenkamp and Dermott (1998), $P_\oplus$ varies in time due to the long-term variations of the Earth's orbit. Because our goal is to compare the terrestrial accretion rate of Karin and Veritas particles with the LDEF measurements, we need to calculate $P_\oplus$ at the current epoch. We have experimented with several techniques. Estimation of $P_\oplus$ via Öpik probabilistic formalism (Öpik, 1951) is not accurate because of the difficulty with dealing with particles trapped in mean motion resonances with the Earth which are phase-protected against impacts. Therefore, we resorted to a numerical technique which we describe below.

To determine $P_\oplus$ of Karin and Veritas particles at the current epoch we used the results obtained in Section 2.2, where we have obtained an accurate orbital distribution of particles at the current epoch in different semimajor axis zones. To estimate $P_\oplus$, we cloned these particles, tracked their orbits into future (using `swift_rmvs3`; Levison and Duncan, 1994) and counted impacts on the Earth. We have set the integration time, T_integ, to be much shorter than the time scale on which Earth's inclination and eccentricity changes. Specifically, we cloned each particle $\sim$100 times (by applying small perturbations on mean anomaly) and used $T_\mathrm{integ} = 5000$ yr. We estimate that this set up assures about 20% accuracy of $P_\oplus$.

In the second step, we computed the terrestrial mass accretion rate of particles with diameter D, $A(D)$, via the following formula:

$$A(D) = \frac{\pi}{6} D^3 \rho \sum_j P_\oplus^{(j)}(D) N^{(j)}(D), \qquad (14)$$

where $N^{(j)}(D)$ is the differential size distribution of particles in semimajor axis zone j, $P_\oplus^{(j)}(D)$ is the impact probability per one particle with diameter D in zone j per year (determined from our numerical integrations described above). $N^{(j)}(D)$ was obtained by calibrating the SFD in each zone by our model fits to IRAS data (Section 4.2.2). We used the same density, $\rho = 2 \ \mathrm{g\,cm^{-3}}$, for Karin and Veritas particles.

Finally, we calculated $A_\oplus = \int \mathrm{d}D \, A(D)$, with limits between $D_\mathrm{min} = 20$ and $D_\mathrm{max} = 400$ μm. This model $A_\oplus$ can be directly compared to the terrestrial mass accretion rate measured by the LDEF. By analyzing the impact record on LDEF, it was estimated that 20,000–60,000 tons of particles with sizes in a diameter range of $\approx$20–400 μm are annually accreted by the Earth (Love and Brownlee, 1993; Taylor et al., 1996). This estimate assumes that particles impact at typical speeds $\approx$17 km s^{-1}. While this assumption may be reasonable for asteroid particles, it may not hold for cometary particles which could impact at much larger speeds. If the contribution of cometary particles to the LDEF record is important, the mass annually accreted by the Earth is likely to be smaller than the above estimates.

With $\tau_\mathrm{col}^\mathrm{Gi}$, $\tau_\mathrm{P} = \infty$ Myr and $\gamma = 3.0$ (corresponding to our best-fit Model II) we found that Karin and Veritas particles contribute to the terrestrial accretion rate by 15,000 t yr^{-1}. This estimate is insensitive to γ ($<$10% variations in $A_\oplus$ with different values of γ) but sensitively depends on τ_P. With $\tau_\mathrm{P} = 1.0$ Myr we found $A_\oplus = 20,000$ t yr^{-1}. Given these results, we estimate that Karin and Veritas particles contribute $\approx$15,000–20,000 t yr^{-1} to the Earth's accretion rate (assuming 2 g cm^{-3} particle density). Karin and Veritas particles contribute to these rates in roughly equal proportions. The larger contribution of Karin particles relative to $S_\mathrm{K}/S_\mathrm{V}$ reflects their smaller i values, which produce smaller encounter velocities and a larger gravitational focusing factor by the Earth.

Our values of $A_\oplus$ are comparable to those determined by Dermott et al. (2002), who suggested that Karin and Veritas particles contribute by $\approx$30% to the terrestrial accretion rate (see also Dermott et al., 2001). We also found that Veritas particles contribute to $A_\oplus$ in about the same proportion as Karin

particles, while Dermott et al. (2002) estimates that Veritas particles contribute about 5 times more to $A_\oplus$ than Karin particles. This difference between our results and Dermott et al. likely comes from our different models. Independent of these differences, however, both our team and Dermott et al. suggest that $\gtrsim 50\%$ of the terrestrial accretion rate must be provided by additional sources of particles (e.g., other asteroids, comets). Alternatively, the LDEF-inferred terrestrial accretion rate can be smaller than that suggested by Love and Brownlee (1993) if there was an important contribution of high-speed particles to LDEF measurements.

We speculate that our IDPs and micrometeorite collections may contain particle species from the two identified parent asteroids. According to our accretion estimates, Karin and Veritas particles should be represented in these samples in roughly equal proportions. Karin particles derive from a parent body classified as an S-type based on the reflectance spectra of the observed asteroid fragments (Jedicke et al., 2004; Nesvorný et al., 2005a). The S-type asteroids have olivine-rich silicate mineralogy (Gaffey et al., 1993) that may be linked with the olivine class of IDPs described in Jessberger et al. (2001). Veritas particles derived from a Ch-type parent body (Mothé-Diniz et al., 2005), whose mineralogy corresponds to hydrated silicates. We speculate that Veritas particles may be linked with the layer-lattice hydrated IDPs and phyllosilicate micrometeorites. See Jessberger et al. (2001) for a review of mineralogical and elementary properties of IDPs and micrometeorites from the collected samples.

When extrapolated to $D \gg 1$ cm with $\alpha = 3.5$, the SFDs of Karin and Veritas particles with $10\ \mu m < D < 1$ cm (calibrated here from IRAS) link up nicely with the observed SFDs of $D > 1$ km asteroid members in the Karin and Veritas families. Thus, despite possible wiggles in the SFD slope for small D (Fig. 23), the steep SFDs of asteroid families for $D \gtrsim 10$ km (Tanga et al., 1999) and the likely changes in α for intermediate D, the overall slope of the fragment SFDs produced in catastrophic collisions is close to the Dohnanyi's slope expected for collisionally relaxed SFDs ($\alpha = 2.5$). If so, most of the total mass of a family is in large fragments and most of the cross-sectional area is in small particles. The integrated masses in fragments with $D > 10\ \mu m$ for our estimated SFDs are comparable to masses of parent bodies of the Karin cluster and the Veritas family determined by other means (Nesvorný et al., 2005b; Durda et al., 2005). These results represent an important constraint for hydrocode simulations of asteroids/planetesimals disruption events (e.g., Michel et al., 2001).[10]

Finally, we discuss the interpretation of $f_K \approx 20$ that we derived from the IRAS data. This large value of f corresponds to $\Delta i \approx 1.8°$ and the ejection velocities of ≈ 300–400 m s^{-1}. These values set an upper limit on speeds by which $D \sim 1$–10 cm meteoroids (precursor bodies of small Karin particles observed in the dust bands) were collisionally ejected when the

Karin family formed. Large values of f may have been also contributed by the increased dispersion of particles produced by secondary fragmentations. While perfectly reasonable, another interpretation is possible or perhaps even likely. The large values of f_K determined here for the Karin family may be an artifact of our two source model. Large values of f_K may incorporate a third, near-ecliptic source such as the Themis family (Grogan et al., 2001). If so, our results on SFDs of particles and their contribution to the zodiacal cloud and LDEF still hold, except some part of our Karin particles stands for a contribution from the third source.

Independent evidence for a contribution of the third near-ecliptic source may come from the temperature profile $T(R)$ that was required to produce our successful fits to the near-ecliptic emission. To obtain satisfactory fits, we used $T(R) \propto R^{-0.35}$ for Karin particles. With $T(R) \propto R^{-0.5}$, our two-source model did not produce satisfactory fits to the data. In particular, the model signal in the 12 μm was ≈ 30–40% weaker and more irregular/wider than the observed signal. With $T(R) \propto R^{-0.5}$, particles at 2–3 AU are relatively cold, ≈ 200 K at 2 AU and ≈ 160 K at 3 AU. The flux spectral density of the thermal emission from these particles peaks at 14.5 and 18.0 μm, respectively. This means that Karin particles, while in the main belt, contribute to the 12-μm IRAS filter in the steeply dropping Wien part of their thermal radiation, and explains why our model signal in 12 μm is weak with $T(R) \propto R^{-0.5}$.

This problem could be alleviated if there is a significant contribution from a near-ecliptic asteroid source in the inner main belt such as the Massalia family (Nesvorný et al., 2003). This asteroid family has $a \approx 2.4$ AU, $e \approx 0.16$, and $i \approx 1.43°$, and is 110–240-Myr old (Vokrouhlický et al., 2006). Dust particles produced in the Massalia family would be distributed at $a < 2.4$ AU where they would not excessively contribute to 24- and 60-μm IRAS wavelengths. Because the Massalia family has a relatively large eccentricity ($e \approx 0.16$), the particles produced in the family could reach 1.7 AU before being spread by the effects of secular resonances at $a = 2$ AU. Thermal emission from these relatively hot particles would significantly contribute to 12-μm IRAS wavelengths, thus resolving our problem with $T(R)$. Conversely, Themis particles would contribute to different IRAS wavelengths in similar ways as Karin particles. Further work will be needed to resolve this issue.

6. Conclusions

Here we briefly summarize the results of our work, which has important implications for: (i) the transport of dust particles from their source regions to the inner Solar System; (ii) the origin of a large fraction of the IDPs accreted by Earth; (iii) the interpretation of long term variations in the accretion rate of IDPs on Earth; and (iv) the physical makeup and structure of the zodiacal cloud:

(1) We found that the Karin and Veritas families are viable sources for the inner and outer IRAS band pairs. We base this on their recent formation, their location in the main belt, and our fits we get between our model and IRAS ob-

---

[10] Results of Farley et al. (2006) show that the SFD of original Veritas particles with $D \approx 10\ \mu m$ produced by the Veritas breakup was steep ($\alpha \approx 4.0$). This steep SFD evolved by collisions over ≈ 8.3 Myr to the present SFD of small Veritas particles which is more shallow ($\alpha \approx 2.0$–2.5).

servations. Plausible sources for the residual, inclination 1.4° IRAS dust band include: the Themis family, Massalia family, some other yet-to-be identified asteroid breakup, etc. Previous studies have found that particles originating in the Themis family match the properties of the innermost dust band inferred from IRAS observations. The Themis family corresponds to one of the largest disruption events to occur in the main belt over the last several Gyr. It is plausible that the comminution among the family members is enough to keep the dust band supplied with material ≈2 Gyr after its formation (Nesvorný et al., 2003). On the other hand, the Massalia family is only 110–240 Myr old (Vokrouhlický et al., 2006) which may also be an important factor when it comes to a question of current contribution of Themis and Massalia families to the 1.4° IRAS dust band. The observed brightnesses of near-ecliptic band pairs in different IRAS wavelengths may be used to distinguish between these two potential sources because the contribution of warmer Massalia particles (produced at $a \approx 2.4$ AU) to shorter wavelengths should be stronger than that of colder Themis particles (produced at $a \approx 3.1$ AU).

(2) Collisions and P–R drift of Karin and Veritas particles produce SFDs that become steeper at smaller a. At 1 AU, the SFD is shallow for small D (differential slope exponent of particles with $D \lesssim 100$ μm is ≈2.2–2.5) and then steepens for $D \gtrsim 100$ μm. Most of the mass at 1 AU, as well as most of the cross-sectional area, is contributed by particles with $D \approx 100$–200 μm. There are $\approx 5 \times 10^{24}$ Karin and $\approx 10^{25}$ Veritas family particles with $D > 30$ μm in the Solar System. The IRAS observation of the dust bands may be satisfactorily modeled using 'averaged' SFDs that are constant with a. These SFDs are best described by a broken power-law function with differential power index $\alpha \approx 2.1$–2.4 for $D \lesssim 100$ μm and by $\alpha \gtrsim 3.5$ for 100 μm $\lesssim D \leqslant 1$ cm. The total cross-sectional surface area of Veritas particles is a factor of ≈2 larger than the surface area of the particles producing the inner dust bands. The total volumes in Karin and Veritas family particles with 1 μm $< D < 1$ cm correspond to $D \approx 11$ km and $D \approx 14$ km asteroids with equivalent masses 1.5×10^{18} g and 3.0×10^{18} g, respectively (assuming 2 g cm^{-3} bulk density).

(3) The Karin and Veritas family particles contribute by 6–9% in 10–60-μm wavelengths to the total zodiacal cloud brightness within 50° and by 9–15% within 10° latitudes from the ecliptic. Because these two sources are clearly the strongest individual asteroid-source contributors to the zodiacal cloud emission, the asteroid dust and micrometeoroids may represent a smaller part of the zodiacal cloud than suggested by Dermott et al. (2001). We hypothesize that cometary sources with flat inclination distributions may be the best candidates to explain the strength and latitudinal extent of the zodiacal cloud emission because asteroidal sources (and Jupiter family comets) have inclinations that are too small to produce the observed IR flux from large ecliptic latitudes. Hahn et al. (2002) used a similar argument based on Clementine observations of the zodiacal cloud in optical wavelengths to argue that more than

90% of the zodiacal dust cross-section enclosed by a 1-AU-radius sphere around the Sun is of a cometary origin. One problem with Hahn et al.'s argument is that the scattering function and the radial dust density distribution were not well separated. Therefore, the latitudinal extent of the zodiacal cloud was not reliably translated in an inclination distribution. Conversely, our work unambiguously links the inclination distribution of the asteroidal dust with the latitudinal distribution of the observed thermal emission. We find that the contribution of cometary dust to the zodiacal cloud is likely to be substantial.

(4) The terrestrial accretion rate of Karin and Veritas particles with $D = 20$–400 μm is about 15,000–20,000 t yr^{-1} (assuming 2 g cm^{-3} particle density). This value represents ≈30–50% of the terrestrial accretion rate of cosmic material measured by LDEF (Love and Brownlee, 1993), or a larger fraction if the remaining impacts measured by LDEF were produced by high-speed cometary impactors. The range of model values given here reflects the variation of the terrestrial accretion rate produced by our two-source model, with collisional and dynamical evolution affecting the source populations on a time scale of several Myr. Other sources are needed to explain the remaining fraction of cosmic dust striking Earth today. Our collections of IDPs and micrometeorites should contain particle species from both the Karin and Veritas families. The Karin family IDPs should be about as abundant in our collections as Veritas family IDPs though this ratio may change if the contribution of third, near-ecliptic source is significant.

(5) The disproportional contribution of Karin/Veritas particles to the zodiacal cloud (only 5–9%) and to the terrestrial accretion rate (30–50%) suggests that the effects of gravitational focusing by the Earth enhance the accretion rate of Karin/Veritas particles relative to those in the background zodiacal cloud. From this result and from the latitudinal brightness of the zodiacal cloud (discussed above), we infer that the zodiacal cloud emission may be dominated by high-speed cometary particles, while the terrestrial impactor flux contains major contribution from asteroidal sources.

(6) The ejection speeds of $D \sim 1$–100 cm fragments launched from the Karin and Veritas parent bodies during their family formation event did not exceed ≈400 and ≈200 m s^{-1}, respectively. Sources of dust particles launched above this speed limit tend to be too spread in inclination space, such that their particles produce poor a match to IRAS observations. Ejection velocities $\ll 400$ m s^{-1} may apply for Karin particles if f_K values derived were artificially pushed to larger values in our two-source model because we neglected the third, near-ecliptic source.

(7) The optical properties of olivine and pyroxene materials work best to match the IRAS observations of the dust bands. Carbon grains with low carbonization levels described by Jäger et al. (1998) produce signals that are too weak in 60-μm wavelengths and are thus poor analogs for particles in the dust bands.

(8) When the slope of our SFD for centimeter-sized particles in both the Karin and Veritas families are extrapolated to large D with $\alpha \approx 3.5$, it connects with the SFDs of Karin and Veritas family asteroids at $D \sim 0.1$–1 km. This result indicates the steep SFD of observed asteroid members in the Karin cluster ($\alpha \approx 5$; Nesvorný et al., 2005b) cannot continue much beyond $D < 1$ km. The same result is likely to hold for Veritas and other main-belt families whose observed members have a comparably steep SFD (e.g., Tanga et al., 1999; see also Morbidelli et al., 2003; Bottke et al., 2005).

Acknowledgments

Appendix A. Invariant frame definition

In the first step, we transformed the pointing direction of IRAS from B1950.0 to J2000.0 using the following algorithm that has been suggested to us by W. Owen.

1. Rotate from geocentric ecliptic to equatorial coordinates using the rotation matrix:

$$R(-\epsilon_1) = \begin{pmatrix} 1 & 0 & 0 \\ 0 & \cos\epsilon_1 & -\sin\epsilon_1 \\ 0 & \sin\epsilon_1 & \cos\epsilon_1 \end{pmatrix},$$

where $\epsilon_1 = 23°.445787875004344$ is the 1950.0 value for the obliquity.

2. Rotate from 1950.0 equatorial to 2000.0 equatorial coordinates using the matrix:

$$\begin{pmatrix} 0.9999256778471213 & -0.0111816373488345 & -0.0048589883900042 \\ 0.0111816373273023 & 0.9999374831700273 & -0.0000271711639427 \\ 0.0048589884395548 & -0.0000271623014313 & 0.9999881946770940 \end{pmatrix}.$$

1950.0 Cartesian position vector multiplied by this matrix comes out in 2000.0 coordinates.

3. Rotate from 2000.0 equatorial to 2000.0 ecliptic using the rotation matrix

$$R(\epsilon_2) = \begin{pmatrix} 1 & 0 & 0 \\ 0 & \cos\epsilon_2 & \sin\epsilon_2 \\ 0 & -\sin\epsilon_2 & \cos\epsilon_2 \end{pmatrix},$$

where $\epsilon_2 = 23°.439291111111111$ is the 2000.0 value for the obliquity.

To zeroth-order, the ecliptic latitude is unchanged by the transformation and the longitude increases by $\approx 0.64°$. The latitude is slightly higher for longitudes between $0°$ and $180°$ and slightly lower for longitudes between $180°$ and $360°$.

In the second step, we transformed 2000.0 heliocentric ecliptic coordinates to the invariant frame using the rotation matrix:

$$\begin{pmatrix} 0.999655192471335 & -0.000218559985336729 & -0.0262573493831792 \\ 0.0 & 0.999965359274649 & -0.0083234758798735 \\ 0.026258258988317 & 0.00832060588272546 & 0.999620563690367 \end{pmatrix}.$$

We fixed the x-axis of the invariant frame so that ecliptic and invariant frame longitudes are similar for low latitudes. The normal vector to the invariant plane is inclined to the ecliptic by about $1.58°$. The ascending node of the invariant plane is at ecliptic longitude $\approx 198°$.

Appendix B. Evaluation of brightness integral

To evaluate integral (11) over singularities at $r = r_{\text{MIN}}(a, e, i)$ and $r = r_{\text{MAX}}(a, e, i)$, where the spatial density becomes infinite (but integrable), we renormalized the relevant parts of Eq. (9) by introducing new integration variables. In particular, we divided the integral over $S(R, \beta)$ into three parts:

$$I_q = \int_{r_1}^{r_2} \frac{dr\, f(r)}{\sqrt{R(r) - q}},$$

$$I_Q = \int_{r_1}^{r_2} \frac{dr\, f(r)}{\sqrt{Q - R(r)}},$$

$$I_i = \int_{r_1}^{r_2} \frac{dr\, f(r)}{\sqrt{\sin^2 i - \sin^2 \beta(r)}}, \tag{B.1}$$

where r_1 and r_2 are the appropriate integration limits, $f(r)$ stands for all parts in Eq. (11) that depend on r, $q = a(1 - e)$ and $Q = a(1 + e)$. To renormalize these parts at r_1 or r_2, we introduced new variables:

$$t_q = \sqrt{R(r) - q},$$
$$t_Q = \sqrt{Q - R(r)},$$
$$t_i = \sqrt{\sin^2 i - \sin^2 \beta(r)}, \tag{B.2}$$

which transformed (B.1) into

$$I_q = \pm \int_0^{\sqrt{R(r_3) - q}} \frac{f(r)}{\partial R / \partial r} 2t_q\, dt_q,$$

$$I_Q = \mp \int_0^{\sqrt{Q - R(r_3)}} \frac{f(r)}{\partial R / \partial r} 2t_Q\, dt_Q,$$

$$I_i = \mp \int_0^{\sqrt{\sin^2 i - \sin^2 \beta(r_3)}} \frac{f(r)}{\sin 2\beta \partial \beta / \partial r} 2t_i\, dt_i, \tag{B.3}$$

where $r = r(t)$ and $\beta = \beta(t)$ were obtained by inversion of Eqs. (B.2), $r_3 = r_2$ if we renormalized at r_1 and $r_3 = r_1$ if we renormalize at r_2. The upper signs in Eqs. (B.3) correspond to a renormalization at r_1 while the lower signs correspond to a renormalization at r_2. The derivatives $\partial R / \partial r$ and $\partial \beta / \partial r$ in Eqs. (B.3) were calculated analytically by taking derivatives of

the transformation from the telescope- to Sun-centered coordinates.

We calculated integrals (B.3) numerically. To test the accuracy, we varied the number of grid points at which the integrands in (B.3) are evaluated. We found that a simple trapezoidal rule with twenty points for a single annulus crossing produces flux values with the relative accuracy of $\sim 10^{-3}$. This precision is satisfactory in the context of this work. Depending on the location of this annulus, its shape, and the location of the telescope, there may be up to six singularities along the line of sight where integral (11) must be regularized. The difficulty in dealing with the geometry of these various intersections was the main challenge for the development of the SIRT algorithm.

Appendix C. Fourier filter

To compare our model data with IRAS flux measurements we used a Fourier filter that separates high- and low-frequency spatial features. The filtered, high-frequency model signal can be directly compared to the filtered IRAS profiles.

Latitudinal profile $F(b)$ of the IR flux was Fourier transformed into $\mathcal{F}(F)$ (Reach et al., 1997). A version of this signal corresponding to the low-spatial-frequency, broad-background IR flux was created by taking the inverse Fourier transform:

$$F_{\text{back}} = \mathcal{F}^{-1}\big(\mathcal{F}(F)e^{-f^2/2f_1^2}\big), \tag{C.1}$$

where f is the spatial frequency and f_1 is a parameter. A noise-suppressed, smooth latitudinal profile of the original signal was created by another inverse Fourier transform:

$$F_{\text{smooth}} = \mathcal{F}^{-1}\big(\mathcal{F}(F)e^{-f^4/2f_2^4}\big), \tag{C.2}$$

which suppressed very high spatial frequencies ($> f_2$) produced by point sources and instrumental noise. The filtered residual profile was created by taking $R(b) = F_{\text{smooth}}(b) - F_{\text{back}}(b)$.

This method enhances structures with latitudinal scales in the range $f_1^{-1} < b < f_2^{-1}$. We found that $f_1^{-1} = 15°$ and $f_2^{-1} = 1.0°$ work well to suppress noise in the signal and enhance spatial structures that correspond to the dust bands. We also used $f_1^{-1} = 5°$ and $f_2^{-1} = 0.2°$ to better resolve the central bands. Fig. 14 illustrates these choices.

We have also experimented with a filter where the low-spatial-frequency signal is extracted from the original signal by the inverse Fourier transform:

$$F_{\text{back}} = \mathcal{F}^{-1}\big(\mathcal{F}(F)p(f)\big). \tag{C.3}$$

The filter profile in the frequency space, $p(f)$, was defined as

$$p(f) = \frac{1}{2}\big[1 - \tanh C_{\text{f}}(|f| - f_3)\big]. \tag{C.4}$$

This filter profile analytically approximates a step-like function (Guzzo and Benettin, 2001). Terms with frequencies higher than f_3 are suppressed and terms with frequencies lower than f_3 are retained in the signal.

Parameter C_{f} controls the width of the transition region. We used $C_{\text{f}} = 50$. Larger values of C_{f} produce a narrower transition region but generate artificial waves in the extracted signal in the

time domain. Smaller values of C_{f} produce a wider transition region. Factor f_3 controls the location of the transition region. We used $f_3^{-1} = 15°$. With larger values of f_3, the filter retains only a weak residual high-frequency signal. With smaller values of f_3, the filter leaves medium-frequency signal in the residual profile.

We used the filter defined by (C.3) and (C.4) to produce a residual high-frequency signal, $R(b) = F_{\text{smooth}}(b) - F_{\text{back}}(b)$, that does not include any traces of the low-frequency signal. This operation is linear. Moreover, a second application of the filter on the residual signal recovers the same, original residual high-frequency signal. Therefore, Grogan et al.'s (2001) iterative method applied to the model/observed data with this filter produces the same result as a single application of filter on the model/observed data. We have verified that the best-fit parameters obtained with filter (C.4) are nearly identical to those obtained with (C.1). Our results obtained with in Section 4 are thus insensitive to details of the filtering method.

References

Berg, O.E., Grün, E., 1973. Evidence for Hyperbolic Cosmic Dust Particles. COSPAR Space Research, vol. XIII. Akademie Verlag, Berlin, pp. 1046–1055.

Bohren, C.F., Huffman, D.R., 1983. Absorption and Scattering of Light by Small Particles. Wiley, New York.

Bottke, W.F., Durda, D.D., Nesvorný, D., Jedicke, R., Morbidelli, A., Vokrouhlický, D., Levison, H.F., 2005. The origin and evolution of stony meteorites. In: Knežević, Z., Milani, A. (Eds.), Dynamics of Populations of Planetary Systems. Cambridge Univ. Press, Cambridge, pp. 357–374.

Boulanger, F., Beichman, C., Desert, F.X., Helou, G., Perault, M., Ryter, C., 1988. Small grains and IRAS colors. Astrophys. J. 332, 328–334.

Bowell, E., Muinonen, K., Wasserman, L.H., 1994. A public-domain asteroid orbit database. In: Milani, A., Di Martino, M., Cellino, A. (Eds.), Asteroids, Comets and Meteors. Kluwer, Dordrecht, pp. 477–481.

Bowey, J.E., Barlow, M.J., Molster, F.J., Hofmeister, A.M., Lee, C., Tucker, C., Lim, T., Ade, P.A.R., Waters, L.B.F.M., 2002. The 69-μm forsterite band as a dust temperature indicator. Mon. Not. R. Astron. Soc. 331, L1–L6.

Bradley, J.P., Humecki, H.J., Germani, M.S., 1992. Combined infrared and analytical electron microscope studies of interplanetary dust particles. Astrophys. J. 394, 643–651.

Bradley, J.P., Klller, L.P., Brownlee, D.E., Thomas, K.L., 1996. Reflectance spectroscopy of interplanetary dust particles. Meteorit. Planet. Sci. 31, 394–402.

Brown, P.G., Campbell-Brown, M.D., 2003. The Canadian Meteor Orbit Radar (CMOR): Early results. In: AAS/DPS Meeting Abstracts 35.

Brown, P.G., Jones, J., 1999. Meteoroid streams of asteroidal origin. In: Baggaley, W.J., Porubčan, V. (Eds.), Meteoroids. Proceedings of the International Conference held at Tatranska Lomnica, Slovakia, p. 159.

Burns, J.A., Lamy, P.L., Soter, S., 1979. Radiation forces on small particles in the Solar System. Icarus 40, 1–48.

Bus, S.J., Binzel, R.P., 2002. Phase II of the small main-belt asteroid spectroscopic survey. A feature-based taxonomy. Icarus 158, 146–177.

Cellino, A., Bus, S.J., Doressoundiram, A., Lazzaro, D., 2002. Spectroscopic properties of asteroid families. In: Bottke, W.F., Cellino, A., Paolicchi, P.R., Binzel, P. (Eds.), Asteroids III. Univ. of Arizona Press, Tucson, pp. 633–643.

Ceplecha, Z., Borovička, J., Elford, W.G., Revelle, D.O., Hawkes, R.L., Porubčan, V., Šimek, M., 1998. Meteor phenomena and bodies. Space Sci. Rev. 84, 327–471.

Crovisier, J., Leech, K., Bockelee-Morvan, D., Brooke, T.Y., Hanner, M.S., Altieri, B., Keller, H.U., Lellouch, E., 1997. The spectrum of Comet Hale–Bopp (C/1995 01) observed with the Infrared Space Observatory at 2.9 AU from the Sun. Science 275, 1904–1907.

Dermott, S.F., Nicholson, P.D., Burns, J.A., Houck, J.R., 1984. Origin of the Solar System dust bands discovered by IRAS. Nature 312, 505–509.

Dermott, S.F., Nicholson, P.D., Kim, Y., Wolven, B., Tedesco, E.F., 1988. The impact of IRAS on asteroidal science. In: Lawrence, A. (Ed.), Comets to Cosmology. Springer-Verlag, Berlin, pp. 3–18.

Dermott, S.F., Jayaraman, S., Xu, Y.L., Gustafson, B.A.S., Liou, J.C., 1994. A circumsolar ring of asteroidal dust in resonant lock with the Earth. Nature 369, 719–723.

Dermott, S.F., Grogan, K., Durda, D.D., Jayaraman, S., Kehoe, T.J.J., Kortenkamp, S.J., Wyatt, M.C., 2001. Orbital evolution of interplanetary dust. In: Grün, E., Gustafson, B.S., Dermott, S., Fechtig, H. (Eds.), Interplanetary Dust. Springer-Verlag, Berlin, pp. 569–640.

Dermott, S.F., Kehoe, T.J.J., Durda, D.D., Grogan, K., Nesvorný, D., 2002. Recent rubble-pile origin of asteroidal Solar System dust bands and asteroidal interplanetary dust particles. In: Warmbein, B. (Ed.), Asteroids, Comets, and Meteors 2002. ESA Publications, Noordwijk, The Netherlands, pp. 319–322.

Di Martino, M., Migliorini, F., Zappalà, V., Manara, A., Barbieri, C., 1997. Veritas asteroid family: Remarkable spectral differences inside a primitive parent body. Icarus 127, 112–120.

Dohnanyi, J.W., 1969. Collisional models of asteroids and their debris. J. Geophys. Res. 74, 2531–2554.

Dorschner, J., Begemann, B., Henning, T., Jaeger, C., Mutschke, H., 1995. Steps toward interstellar silicate mineralogy. II. Study of Mg–Fe-silicate glasses of variable composition. Astron. Astrophys. 300, 503–520.

Draine, B.T., Lee, H.M., 1984. Optical properties of interstellar graphite and silicate grains. Astrophys. J. 285, 89–108.

Dumont, R., Levasseur-Regourd, A.-C., 1988. Properties of interplanetary dust from infrared and optical observations. Astron. Astrophys. 191, 154–160.

Durda, D.D., Dermott, S.F., 1997. The collisional evolution of the asteroid belt and its contribution to the zodiacal cloud. Icarus 130, 140–164.

Durda, D.D., Bottke, W.F., Nesvorný, D., Enke, B.L., Asphaug, E., Richardson, D.C., 2005. Size-frequency distributions of fragments from SPH/N-body simulations of asteroid impacts. Comparison with observed asteroid families. Icarus. Submitted for publication.

Edoh, O., 1983. Optical Properties of Carbon from Far Infrared to the Far Ultraviolet. Ph.D. Thesis. University of Arizona.

Fajardo-Acosta, S.B., Knacke, R.F., 1995. IRAS low-resolution spectra with β Pictoris-type silicate emission. Astron. Astrophys. 295, 767–774.

Farinella, P., Vokrouhlický, D., Hartmann, W.K., 1998. Meteorite delivery via Yarkovsky orbital drift. Icarus 132, 378–387.

Farley, K.A., Montanari, A., Shoemaker, E.M., Shoemaker, C.S., 1998. Geochemical evidence for a comet shower in the Late Eocene. Science 280, 1250–1253.

Farley, K.A., Vokrouhlický, D., Bottke, W.F., Nesvorný, D., 2006. A Late Miocene dust shower produced by a breakup in the main asteroid belt. Nature. In press.

Gaffey, M.J., Burbine, T.H., Piatek, J.L., Reed, K.L., Chaky, D.A., Bell, J.F., Brown, R.H., 1993. Mineralogical variations within the S-type asteroid class. Icarus 106, 573–602.

Gautier, T.N., Hauser, M.G., Low, F.J., 1984. Parallel measurements of the zodiacal dust bands with the IRAS survey. Bull. Am. Astron. Soc. 16, 442.

Greenberg, R., Nolan, M.C., 1989. Delivery of asteroids and meteorites to the inner Solar System. In: Gehrels, T. (Ed.), Asteroids II. Univ. of Arizona Press, Tucson, pp. 778–801.

Grogan, K., Dermott, S.F., Jayaraman, S., Xu, Y.L., 1997. Origin of the ten degree Solar System dust bands. Planet. Space Sci. 45, 1657–1665.

Grogan, K., Dermott, S.F., Durda, D.D., 2001. The size-frequency distribution of the zodiacal cloud: Evidence from the Solar System dust bands. Icarus 152, 251–267.

Gronchi, G.F., Milani, A., 2001. Proper elements for Earth-crossing asteroids. Icarus 152, 58–69.

Grün, E., Zook, H.A., Fechtig, H., Giese, R.H., 1985. Collisional balance of the meteoritic complex. Icarus 62, 244–272.

Grün, E., Baguhl, M., Svedhem, H., Zook, H.A., 2001. In situ measurements of cosmic dust. In: Grün, E., Gustafson, B.S., Dermott, S., Fechtig, H. (Eds.), Interplanetary Dust. Springer-Verlag, Berlin, pp. 295–346.

Gustafson, B.A.S., 1994. Physics of zodiacal dust. Annu. Rev. Earth Planet. Sci. 22, 553–595.

Gustafson, B.A.S., Greenberg, J.M., Kolokolova, L., Xu, Y., Stognienko, R., 2001. Interactions with electromagnetic radiation: Theory and laboratory simulations. In: Grün, E., Gustafson, B.S., Dermott, S., Fechtig, H. (Eds.), Interplanetary Dust. Springer-Verlag, Berlin, pp. 509–567.

Guzzo, M., Benettin, G., 2001. A spectral formulation of the Nekhoroshev theorem and its relevance for numerical and experimental data analysis. Discrete Cont. Dynam. Syst. Ser. B 1 (1), 1–28.

Hahn, J.M., Zook, H.A., Cooper, B., Sunkara, B., 2002. Clementine observations of the zodiacal light and the dust content of the inner Solar System. Icarus 158, 360–378.

Hanner, M.S., 1996. Composition and optical properties of cometary dust. Astron. Soc. Pacific Conf. Ser. 104, 367–376.

Hanner, M.S., 1999. The silicate material in comets. Space Sci. Rev. 90, 99–108.

Hanner, M.S., Hackwell, J.A., Russell, R.W., Lynch, D.K., 1994. Silicate emission feature in the spectrum of Comet Mueller 1993a. Icarus 112, 490–495.

Hauser, M.G., Gillett, F.C., Low, F.J., Gautier, T.N., Beichman, C.A., Aumann, H.H., Neugebauer, G., Baud, B., Boggess, N., Emerson, J.P., 1984. IRAS observations of the diffuse infrared background. Astrophys. J. 278, L15–L18.

Henning, T., Mutschke, H., 1997. Low-temperature infrared properties of cosmic dust analogues. Astron. Astrophys. 327, 743–754.

Hirayama, K., 1918. Groups of asteroids probably of common origin. Astron. J. 31, 185–188.

Hunt, S.M., Oppenheim, M., Close, S., Brown, P.G., McKeen, F., Minardi, M., 2004. Determination of the meteoroid velocity distribution at the Earth using high-gain radar. Icarus 168, 34–42.

Ishiguro, M., Nakamura, R., Fujii, Y., Morishige, K., Yano, H., Yasuda, H., Yokogawa, S., Mukai, T., 1999. First detection of visible zodiacal dust bands from ground-based observations. Astrophys. J. 511, 432–435.

Jackson, A.A., Zook, H.A., 1992. Orbital evolution of dust particles from comets and asteroids. Icarus 97, 70–84.

Jager, C., Mutschke, H., Henning, T., 1998. Optical properties of carbonaceous dust analogues. Astron. Astrophys. 332, 291–299.

Jäger, C., Dorschner, J., Mutschke, H., Posch, T., Henning, T., 2003. Steps toward interstellar silicate mineralogy. VII. Spectral properties and crystallization behavior of magnesium silicates produced by the sol–gel method. Astron. Astrophys. 408, 193–204.

Janches, D., Meisel, D.D., Mathews, J.D., 2001. Orbital properties of the Arecibo micrometeoroids at Earth interception. Icarus 150, 206–218.

Jedicke, R., Nesvorný, D., Whiteley, R., Ivezić, Ž., Jurić, M., 2004. An age–color relationship for main-belt S-complex asteroids. Nature 429, 275–277.

Jessberger, E.K., Stephan, T., Rost, D., Arndt, P., Maetz, M., Stadermann, F.J., Brownlee, D.E., Bradley, J.P., Kurat, G., 2001. Properties of interplanetary dust: Information from collected samples. In: Grün, E., Gustafson, B.S., Dermott, S., Fechtig, H. (Eds.), Interplanetary Dust. Springer-Verlag, Berlin, pp. 253–294.

Kelsall, T., and 11 colleagues, 1998. The COBE diffuse infrared background experiment search for the cosmic infrared background. II. Model of the interplanetary dust cloud. Astrophys. J. 508, 44–73.

Kessler, D.J., 1981. Derivation of the collision probability between orbiting objects. The lifetimes of Jupiter's outer moons. Icarus 48, 39–48.

Knacke, R.F., Fajardo-Acosta, S.B., Telesco, C.M., Hackwell, J.A., Lynch, D.K., Russell, R.W., 1993. The silicates in the disk of beta Pictoris. Astrophys. J. 418, 440–450.

Kortenkamp, S.J., Dermott, S.F., 1998. Accretion of interplanetary dust particles by the Earth. Icarus 135, 469–495.

Leinert, C., Grün, E., 1990. Interplanetary dust. In: Schwenn, R., Marsch, E. (Eds.), Physics of the Inner Heliosphere. Springer-Verlag, Berlin, pp. 207–275.

Leinert, Ch., Ábrahám, P., Acosta-Pulido, J., Lemke, D., Siebenmorgen, R., 2002. Mid-infrared spectrum of the zodiacal light observed with ISOPHOT. Astron. Astrophys. 393, 1073–1079.

Levison, H.F., Duncan, M.J., 1994. The long-term dynamical behavior of short-period comets. Icarus 108, 18–36.

Li, A., Greenberg, J.M., 1997. A unified model of interstellar dust. Astron. Astrophys. 323, 566–584.

Love, S.G., Brownlee, D.E., 1993. A direct measurement of the terrestrial mass accretion rate of cosmic dust. Science 262, 550–554.

Love, S.G., Joswiak, D.J., Brownlee, D.E., 1994. Densities of stratospheric micrometeorites. Icarus 111, 227–236.

Low, F.J., Young, E., Beintema, D.A., Gautier, T.N., Beichman, C.A., Aumann, H.H., Gillett, F.C., Neugebauer, G., Boggess, N., Emerson, J.P., 1984. Infrared cirrus—New components of the extended infrared emission. Astrophys. J. 278, L19–L22.

MacKinnon, I.D.R., Rietmeijer, F.J.M., 1987. Mineralogy of chondritic interplanetary dust particles. Rev. Geophys. 25, 1527–1553.

Mahoney-Hopping, L., Dermott, S.F., Kehoe, T., Kolokolova, L., Grogan, K., 2003. Sources of the Solar System dust bands and interplanetary dust particles. In: AAS/DPS Meeting Abstracts 35.

Mahoney-Hopping, L., Dermott, S.F., Kehoe, T., 2004. Recent catastrophic disruptions of main-belt asteroids as a source of the Solar System dust bands and interplanetary dust particles. In: AAS/DPS Meeting Abstracts 36.

Marzari, F., Weidenschilling, S., 2002. Mean motion resonances, gas drag, and supersonic planetesimals in the solar nebula. Celest. Mech. Dynam. Astron. 82, 225–242.

Mathews, J.D., Janches, D., Meisel, D.D., Zhou, Q.-H., 2001. The micrometeoroid mass flux into the upper atmosphere: Arecibo results and a comparison with prior estimates. Geophys. Res. Lett. 28, 1929–1932.

McDonnell, J.A.M., Gardner, D.J., 1998. Meteoroid morphology and densities: Decoding satellite impact data. Icarus 133, 25–35.

McDonnell, T., McBride, N., Green, S.F., Ratcliff, P.R., Gardner, D.J., Griffiths, A.D., 2001. Near-Earth environment. In: Grün, E., Gustafson, B.S., Dermott, S., Fechtig, H. (Eds.), Interplanetary Dust. Springer-Verlag, Berlin, pp. 163–231.

Michel, P., Froeschlé, C., 1997. The location of linear secular resonances for semimajor axes smaller than 2 AU. Icarus 128, 230–240.

Michel, P., Benz, W., Tanga, P., Richardson, D.C., 2001. Collisions and gravitational reaccumulation: Forming asteroid families and satellites. Science 294, 1696–1700.

Milani, A., Knežević, Z., 1994. Asteroid proper elements and the dynamical structure of the asteroid main belt. Icarus 107, 219–254.

Molster, F.J., Waters, L.B.F.M., Tielens, A.G.G.M., Koike, C., Chihara, H., 2002. Crystalline silicate dust around evolved stars. III. A correlations study of crystalline silicate features. Astron. Astrophys. 382, 241–255.

Morbidelli, A., Henrard, J., 1991. The main secular resonances ν_6, ν_5 and ν_{16} in the asteroid belt. Celest. Mech. 51, 169–197.

Morbidelli, A., Moons, M., 1993. Secular resonances in mean motion commensurabilities—The 2/1 and 3/2 cases. Icarus 102, 316–332.

Morbidelli, A., Nesvorný, D., Bottke, W.F., Michel, P., Vokrouhlický, D., Tanga, P., 2003. The shallow magnitude distribution of asteroid families. Icarus 162, 328–336.

Moro-Martín, A., Malhotra, R., 2003. Dynamical models of Kuiper belt dust in the inner and outer Solar System. Astron. J. 125, 2255–2265.

Moshir, M. (Ed.), 1989. IRAS Faint Source Survey, Explanatory Supplement Version 1 and Tape. Infrared Processing and Analysis Center, California Institute of Technology, Pasadena, CA.

Mothé-Diniz, T., Roig, F., Carvano, J.M., 2005. Reanalysis of asteroid families structure through visible spectroscopy. Icarus 174, 54–80.

Murray, C.D., Dermott, S.F., 1999. Solar System Dynamics. Cambridge Univ. Press, Cambridge.

Mutschke, H., Begemann, B., Dorschner, J., Guertler, J., Gustafson, B., Henning, T., Stognienko, R., 1998. Steps toward interstellar silicate mineralogy. III. The role of aluminium in circumstellar amorphous silicates. Astron. Astrophys. 333, 188–198.

Nakamura, A., Suguiyama, K., Fujiwara, A., 1992. Velocity and spin fragments from impact disruptions. I. An experimental approach to a general law between mass and velocity. Icarus 100, 127–135.

Nesvorný, D., Bottke, W.F., 2004. Detection of the Yarkovsky effect for main-belt asteroids. Icarus 170, 324–342.

Nesvorný, D., Bottke, W.F., Levison, H.F., Dones, L., 2002. A recent asteroid breakup in the main belt. Nature 417, 720–722.

Nesvorný, D., Bottke, W.F., Levison, H.F., Dones, L., 2003. Recent origin of the Solar System dust bands. Astrophys. J. 591, 486–497.

Nesvorný, D., Jedicke, R., Whiteley, R.J., Ivezić, Z., 2005a. Evidence for asteroid space weathering from the Sloan Digital Sky Survey. Icarus 173, 132–152.

Nesvorný, D., Enke, B.L., Bottke, W.F., Durda, D.D., Asphaug, E., Richardson, D.C., 2005b. Karin cluster formation via asteroid impact. Icarus. Submitted for publication.

Neugebauer, G., and 27 colleagues, 1984. The Infrared Astronomical Satellite (IRAS) mission. Astrophys. J. 278, L1–L6.

Öpik, E.J., 1951. Collision probabilities with the planets and the distribution of interplanetary matter. Proc. R. Irish Acad. 54, 165–199.

Reach, W.T., 1992. Zodiacal emission. III. Dust near the asteroid belt. Astrophys. J. 392, 289–299.

Reach, W.T., Franz, B.A., Weiland, J.L., Hauser, M.G., Kelsall, T.N., Wright, E.L., Rawley, G., Stemwedel, S.W., Spiesman, W.J., 1995. Observational confirmation of a circumsolar dust ring by the COBE satellite. Nature 374, 521–523.

Reach, W.T., Franz, B.A., Weiland, J.L., 1997. The three-dimensional structure of the zodiacal dust bands. Icarus 127, 461–484.

Reach, W.T., Morris, P., Boulanger, F., Okumura, K., 2003. The mid-infrared spectrum of the zodiacal and exozodiacal light. Icarus 164, 384–403.

Renard, J.B., Levasseur-Regourd, A.C., Dumont, R., 1995. Properties of interplanetary dust from infrared and optical observations. Astron. Astrophys. 304, 602–608.

Sandford, S.A., Walker, R.M., 1985. Laboratory infrared transmission spectra of individual interplanetary dust particles from 2.5 to 25 microns. Astrophys. J. 291, 838–851.

Sekanina, Z., Hanner, M.S., Jessberger, E.K., Fomenkova, M.N., 2001. Cometary dust. In: Grün, E., Gustafson, B.S., Dermott, S., Fechtig, H. (Eds.), Interplanetary Dust. Springer-Verlag, Berlin, pp. 95–161.

Šidlichovský, M., Nesvorný, D., 1994. Temporary capture of grains in exterior resonances with the Earth: Planar circular restricted three-body problem with Poynting–Robertson drag. Astron. Astrophys. 289, 972–982.

Šidlichovský, M., Nesvorný, D., 1997. Frequency modified Fourier transform and its applications to asteroids. Celest. Mech. Dynam. Astron. 65, 137–148.

Spiesman, W.J., Hauser, M.G., Kelsall, T., Lisse, C.M., Moseley, S.H.J., Reach, W.T., Silverberg, R.F., Stemwedel, S.W., Weiland, J.L., 1995. Near- and far-infrared observations of interplanetary dust bands from the COBE diffuse infrared background experiment. Astrophys. J. 442, 662–667.

Sykes, M.V., 1986. IRAS Observations of Asteroid Dust Bands and Cometary Dust Trails. Ph.D. Thesis. Arizona University, Tucson.

Sykes, M.V., 1988. IRAS observations of extended zodiacal structures. Astrophys. J. 334, L55–L58.

Sykes, M.V., 1990. Zodiacal dust bands—Their relation to asteroid families. Icarus 85, 267–289.

Sykes, M.V., Greenberg, R., 1986. The formation and origin of the IRAS zodiacal dust bands as a consequence of single collisions between asteroids. Icarus 65, 51–69.

Sykes, M.V., Grün, E., Reach, W.T., Jenniskens, P., 2005. The interplanetary dust complex and comets. In: Festou, M., Keller, U., Weaver, H. (Eds.), Comets II. Univ. of Arizona Press, Tucson. In press.

Tanga, P., Cellino, A., Michel, P., Zappalà, V., Paolicchi, P., Dell'Oro, A., 1999. On the size distribution of asteroid families: The role of geometry. Icarus 141, 65–78.

Taylor, S., Lever, J.H., Harvey, R.P., 1996. Terrestrial flux rates of micrometeorites determined from the south pole water well. Meteorit. Planet. Sci. 31, A140.

Tedesco, E.F., Noah, P.V., Noah, M., Price, S.D., 2002. The supplemental IRAS minor planet survey. Astron. J. 123, 1056–1085.

Vokrouhlický, D., Brož, M., Bottke, W.F., Nesvorný, D., Morbidelli, A., 2006. Yarkovsky/YORP chronology of asteroid families. Icarus. In press.

Waelkens, C., and 20 colleagues, 1996. SWS observations of young main-sequence stars with dusty circumstellar disks. Astron. Astrophys. 315, L245–L248.

Weidenschilling, S.J., Jackson, A.A., 1993. Orbital resonances and Poynting–Robertson drag. Icarus 104, 244–254.

Williams, J.G., 1979. Proper elements and family memberships of the asteroids. In: Gehrels, T. (Ed.), Asteroids. Univ. of Arizona Press, Tucson, pp. 1040–1063.

Wisdom, J., Holman, M., 1991. Symplectic maps for the N-body problem. Astron. J. 102, 1528–1538.

Wyatt, S.P., Whipple, F.L., 1950. The Poynting–Robertson effect on meteor orbits. Astrophys. J. 111, 134–141.

Zubko, V.G., Mennella, V., Colangeli, L., Bussoletti, E., 1996. Optical constants of amorphous carbon extracted from recent laboratory extinction measurements. In: Käufl, H.U., Siebenmorgen, R. (Eds.), Proceedings of the ESO Workshop. Springer-Verlag, Berlin, p. 333.